A study of snow optical properties with a multiple scattering radiative transfer model for the atmosphere-snow system and spectral albedo observations

Teruo Aoki

DOCTOR OF PHILOSOPHY

Department of Polar Science
School of Mathematical and Physical Science
The Graduate University for Advanced Studies

1999

A study of snow optical properties with a multiple scattering radiative transfer model for the atmosphere-snow system and spectral albedo observations

by
Teruo Aoki

Meteorological Research Institute
1-1 Nagamine, Tsukuba, Ibaraki 305-0052, Japan

Ph. D. Thesis

Department of Polar Science
School of Mathematical and Physical Science
The Graduate University for Advanced Studies

1999

Table of Contents

Acknowledgments

I express my heartfelt thanks to Drs. Tadao Aoki and Masashi Fukabori of Meteorological Research Institute (MRI) for their valuable comments and discussions throughout this work. I extend my thanks to Dr. Akihiro Uchiyama of MRI for providing the atmospheric absorption parameters and for his helpful comments. I also thank Dr. Yoshihiro Tachibana of Research Institute of Civilization, Tokai University, Dr. Akihiro Hachikubo of Kitami Institute of Technology, Mr. Yuji Zaizen of MRI and Dr. Tomohiko Oishi of Tokai University for their help in the field experiment and their discussions.

I am much obliged to Professor Takashi Yamanouchi, National Institute of Polar Research for his tenderest guidance throughout this dissertation. I am also grateful to Professor Fumihiko Nishio of Hokkaido University of Education, Dr. Toyoaki Tanaka of MRI and Professor Takenori Noumi of Meteorological College, for their kindhearted suggestions.

Some of field experiments and numerical computations in this work have been done as part of ADEOS II/GLI project supported by National Space Development Agency.

Abstract

A multiple scattering radiative transfer model in the shortwave wavelength region has been developed for the atmosphere-snow system in which the absorption and scattering by the realistic gases, aerosols and clouds were included and a radiative interaction between the atmosphere and the snow was simulated. Using this model the atmospheric effects on spectral albedo and radiation budget at the snow surface and the top of the atmosphere were investigated. Furthermore, observations of spectral albedo and bidirectional reflection distribution function (BRDF) with the spectrometer have been made together with the snow pit works on some snowfields. The results of spectral observations were compared to the theoretically calculated ones with a multiple scattering model for the atmosphere-snow system and the effects of snow physical parameters on spectral albedo and BRDF were investigated.

In Chapter 1, the approximation methods for Mie phase function were discussed in calculating the spectral albedo of snow surface by taking account of the multiple scattering by snow particles. The particles such as snow grains which are large compared to the wavelength have a strong forward peak in the phase function of single scattering. It has been known that a large error is led by the calculation of multiple scattering directly using such phase function. Therefore, four types of approximations of Mie phase function were investigated in calculating the multiple scattering by snow particles using the "doubling" method. These involve Hansen's renormalization, Grant's renormalization, the delta-M method and the truncation method. Using these approximations, the spectral albedos of snow surface were calculated under the conditions of effective grain radii of 50, 200 and 1000μm in a wavelength region from 0.3 to 3.0μm, and were compared to that calculated using the delta-Eddington approximation. The reason to compare with the delta-Eddington approximation is that this method does not need a phase function and a behavior of the systematic error is understood. In the Hansen's renormalization, the maximum albedo error exceeded 0.1 for the snow with an effective radius of 1000μm at small solar zenith angles. The delta-M method overestimated the snow albedos at all solar zenith angles at the wavelengths less than 1.4μm for the snow with an effective radius of 1000μm. Reasonable results were obtained by the Grant's renormalization and the truncation method for all three cases of effective grain radii studied. It was also found that these

methods save computation time and memory because sufficient accuracy was obtained even with an angle resolution of 0.1° in the forward peak region of phase function. In case of truncation method, the result was not sensitive to the choice of a truncation angle between 5° and 20°.

In Chapter 2, the atmospheric effects on spectral and spectrally integrated snow albedos at the snow surface and the top of the atmosphere were investigated. A multiple scattering radiative transfer model based on the "doubling and adding" method combined with the Mie theory was applied to estimate the effects of absorption and scattering by the atmospheric molecules, absorptive gases, aerosols and clouds. Based on the result of Chapter 1, the truncation method with a truncation angle of 10° was employed to correct the anisotropic Mie phase function. It was shown that the spectral surface albedo was reduced by the atmospheric absorptive gases at large solar zenith angles. The solar zenith angle dependence was weakened at the wavelengths less than $0.5\mu m$ by the Rayleigh scattering and at almost all wavelengths by the atmospheric aerosols and cloud cover. H_2O rich atmosphere decreased the spectral surface albedo at large solar zenith angle in the H_2O bands, while the additional reduction of downward solar flux in the near infrared region by H_2O absorption caused the spectrally integrated surface albedo to increase by several percent. Aerosols increased the spectrally integrated surface albedo at small solar zenith angles and reduced it at large solar zenith angles, however they reduced the spectrally integrated planetary albedo except at large solar zenith angles. Optically-thick cloud cover increased both the spectrally integrated surface and planetary albedos at any solar zenith angle. In the visible region at small solar zenith angles the downward solar flux on the snow surface under cloudy sky could exceed that for clear case, and both further could exceed the extraterrestrial solar flux, resulting from the multiple reflection between snow surface and the atmosphere (cloud cover).

It is concluded, from what has been said above, that the snow surface albedo is affected by the appearances of cloud or aerosols of high concentration. It is also found that the snow surface albedo is affected by the Rayleigh scattering at shorter wavelengths and by the atmospheric absorption at large solar zenith angles. Thus, it is necessary to take the atmospheric effects into account for comparison of the theoretical albedo of snow surface with the measured one, according to the conditions of clouds, aerosols, water vapor and solar zenith angle.

In Chapter 3, the spectral albedo in the wavelength region of 0.35-2.5 μm observed on the snowfield under the cloudy sky at Barrow, Alaska in April, 1997 was discussed. The observed spectral albedo was compared with the theoretical ones calculated by a multiple scattering model for the atmosphere-snow system using the snow physical parameters obtained from the snow pit work. It was found that for new snow consisting of dendrites the optically effective snow grain size was not a crystal size, but of the order of a branch width. The observed spectral albedo was lower than theoretically calculated one for "pure snow" in the visible region and a part of the near infrared region; such reduction was explained by the internal mixture of soot and the external mixture of dust for snow particles. The theoretical spectral albedo calculated for a two-layer snow model that contains impurities agreed well with the measured one at all wavelengths.

In Chapter 4, the effects of snow physical parameters on spectral albedo and bidirectional reflectance of snow surface were discussed by comparing the observed spectral data with the theoretical ones. The observations of spectral albedo and bidirectional reflectance in the wavelength region of $0.35 - 2.5\,\mu m$ were made together with snow pit work on a flat snowfield under the clear sky in eastern Hokkaido, Japan in February, 1998. The effects of snow impurities, density, layer structure, and grain size attained by in situ and laboratory measurements were taken into account in snow models for which spectral albedos were calculated using a multiple scattering model for the atmosphere-snow system. Comparisons of these theoretical albedos with measured ones suggest that the snow impurities were concentrated at the snow surface by dry fallout of atmospheric aerosols. The optically equivalent snow grain size was found to be of the order of a branch width of dendrites or of a dimension of narrower portion of broken crystals as was same in Chapter 3. This means that the optical equivalent snow grain size is smaller than the so-called snow grain size measured glaciologically. The observational results for the BRDF normalized by the radiance at the nadir showed that the anisotropic reflection was very significant in the near infrared region especially at the wavelengths longer than $1.4\,\mu m$, while the visible normalized BRDF (NBRDF) patterns were relatively flat. Comparison of this result with two kinds of theoretical NBRDFs, where one having been calculated using single scattering parameters by the Mie theory and the other using the same parameters except for Henyey-Greenstein (HG) phase function obtained from the same asymmetry factor as in the Mie theory, showed

that the observed NBRDF agreed with the theoretical one using HG phase function rather than with that using Mie phase function, while the albedos calculated with both phase functions agreed well with each other. This suggests that the optically effective snow grain shape is neither the sphere nor the ordinary hexagonal column, by which respectively the rainbow or halo appear in the theoretical BRDF pattern, but is the nonspherical particle having the smooth phase function.

General Introduction

The cryosphere plays an important role for the energy budget on the earth because of its high reflectance and the large variation of its areal extent. The snow-covered region of the earth's surface, in particular, has a large seasonal variation and its albedo also varies greatly from that of freshly fallen snow to that of melting snow. The melting of polar snow and ice by global warming and the resultant sea level rise are matters currently causing much public anxiety (Warrick *et al.*, 1995). Recently, it is reported that the variation of snow-covered region in the Eurasian Continent has an influence on annual variation of East Asian climate (Yasunari *et al.*, 1991), and many Himalayan glaciers are retreating (Higuchi *et al.*, 1980). An understanding of the radiative process in the cryosphere, especially of snow albedo properties, is important not only for an understanding of the interaction between the atmosphere and the snow surface, but also for the remote sensing of the cryosphere to monitor the climate change.

An attempt to calculate the spectral albedo of snow with a multiple scattering radiative transfer model in the visible and near infrared regions has begun from DUNKLE and BEVANS (1956). This model and the following model by GIDDINGS and LACHAPELLE (1961) did not consider the single scattering properties by each snow grain independent of a multiple scattering, and thus were valid only for the diffuse incidence and high albedo. In the 1970's, many multiple scattering models for snow albedo, which consider the single scattering by each snow grain, have appeared (BARKSTROM, 1972; BOHREN and BARKSTROM, 1974; BARKSTROM and QUERFELD, 1975; BERGER, 1979; CHOUDHURY and CHANG, 1979a, b). However, these models were not accurate enough for the wide ranges of wavelength, grain size and solar zenith angle. One reason is that since the particles larger than the wavelength such as snow grains have a very sharp forward peak of single scattering, a multiple scattering calculation using such the phase function often contains an error. As against this WISCOMBE and WARREN (1980) and WARREN and WISCOMBE (1980) simulated the spectral albedo of snow by the Mie theory for single scattering and by the delta-Eddington approximation for multiple scattering, which is advantageous to the handling of anisotropic phase function. They showed the dependence of the spectral albedo of snow on the observable parameters such as solar zenith angle, snow grain size, illuminating conditions and snow impurities. Viewing from the other standpoint this means that the snow physical

parameters such as grain size and impurities are possible to be remotely retrieved from the space. CHOUDHURY and CHANG (1981a, b) and CHOUDHURY (1981) introduced the effects of the atmospheric gaseous absorption and a surface reflection into their snow albedo model. WARREN (1982) discussed that almost all models until then belonged to the category of two-stream approximation. In the models by WISCOMBE and WARREN (1980) and CHOUDHURY and CHANG (1981a, b) there were following two insufficient points: One is that the realistic atmospheric effects on the radiative interaction between the atmosphere and the snow was not incorporated. The other is that the error increased at large solar zenith angles because of an employment of the two-stream approximation (the delta-Eddington approximation belongs to this category). As we have seen above, the accuracy of the past albedo models of snow surface was not necessarily sufficient with regard to the atmospheric effects and the dependence of solar zenith angle. However, if the multiple scattering model, in which the interaction between the atmosphere and the snow is considered, keeping the accuracy even at large solar zenith angles is developed, it would become the basic model applicable for the studies such as: (1) the satellite remote sensing of snow physical parameters; (2) the radiation budget at the snow surface and the top of the atmosphere; and (3) the prediction of the ultraviolet radiation on the snow surface.

On the remote sensing of snow physical parameters, WARREN (1982) showed that a cloud cover over snow surface is detectable by the reflectance at around the wavelength of 1.6 μm and a liquid water content in the snow could affect the reflectance. The multi-channel optical sensor GLI (Global Imager) mounted on the Japanese satellite ADEOS-II (Advanced Earth Observing Satellite-II) that will be launched in 2000 (NAKAJIMA *et al.*, 1998), equips 36 channels from the visible to the infrared regions. Using this sensor, it is proposed to retrieve the snow grain size and the snow impurities. Since the snow grain size varies depending on the history of meteorological condition such as the temperature and solar radiation under which the snow has exposed, the retrieved snow grain size is possible to be used for the monitoring of climate change on the ice sheet especially in Antarctica with a small amount of short term variation of snow grain size. On the other hand, since the snow impurities reduce the visible albedo (Warren and Wiscombe, 1980), it could enhance the global warming. It is necessary to monitor the global concentration distribution of snow impurities because the strongly absorptive materials especially such as soot, that is

commonly contained in the snow, are anthropogenic impurities produced from a burning of fossil fuels.

For the development of a multiple scattering model for the atmosphere-snow system, the spectral albedo observation of snow surface is very important to evaluate the appropriateness of the model itself. The spectral albedo observations of snow surface have started from the pioneer work made by LILJEQUIST (1956) for four visible bands in Antarctica, and have been followed by the works made by GRENFELL and MAYKUT (1977) and KUHN and SIOGAS (1978) with the spectrometer at the wavelengths longer than 1.6 μm in the polar regions. The visible albedos observed in these works were too low compared to the theoretically predicted ones for pure snow in the polar region. This reason is considered to be caused by the observation method. After that such spectral measurements have been made in the wide spectral range from the visible to the wavelengths beyond 2.0 μm (GRENFELL, 1981; GRENFELL and PEROVICH, 1984; GRENFELL *et al.*, 1994) and the relationships between the spectral albedo and snow physical parameters such as grain size or impurities have been clarified. GRENFELL *et al.* (1994) showed from three wintering observations in Antarctica that the observed spectral albedos agreed well with the theoretical ones calculated with the model by WISCOMBE and WARREN (1980) under cloudy conditions, while some discrepancies remained at the near infrared wavelengths under the clear conditions. WARREN *et al.* (1986) cited the following three reasons on the difficulties in measuring the spectral albedo under clear condition as: (1) setting error of the instrument; (2) the deviation from the so-called "cosine property" of the incident angular sensitivity of the instrument and (3) the problem of the slant snow surface. On the other hand, there are little measurements of the spectral albedo for the snow with complicated layer structure, which would also affect the spectral albedo.

Since the bidirectional reflection property of snow is very anisotropic, the study of bidirectional reflection distribution function (BRDF), that depends on the incident angle and the reflection angle, is very important for satellite remote sensing of snow surface. The early BRDF observations of snow surfaces were made in the broad spectral regions (SALOMONSON and MARLATT, 1968; KUHN, 1974; DIRMHIRN and EATON, 1975). The first measurement in narrow spectral band was made by KUHN and SIOGAS (1978) at the monochromatic wavelength of 0.45 μm at the South Pole and the effect of sastrugi was reported. After that, some BRDF observations were made in the

narrow spectral bands of the wavelength region less than 1.0 μm (KUHN, 1985; STEFFEN, 1987; WARREN *et al.*, 1998) and it was shown that the maximum value of BRDF appeared at the forward scattering direction of the solar zenith angle and the minimum at the backscattering direction. It was also shown from these observations that the relative relation between the Sun and sastrugi highly affected the BRDF pattern. On the other hand, Li (1982) calculated the snow BRDF using the Mie theory and the "doubling" method, but there were a few BRDF models of snow surface considering the interaction with the atmosphere. Recently LEROUX *et al.* (1999) calculated the snow BRDF using the "doubling and adding" method together with the Mie theory and ray optics, and LEROUX and FILY (1998) extended their model to the snow surface with sastrugi. Thus the snow BRDF properties were understood to some extent, but there is no BRDF model to compare with the measured ones in the wide spectral range from the visible to the wavelengths beyond 1.0 μm .

As we have seen above the past albedo models of snow surface were not accurate at the large solar zenith angles and were insufficient with regard to the atmospheric effects. The spectral albedos calculated with such models have been compared with the observed spectral albedos only under the limited conditions. The relationships between spectral albedo and snow physical parameters have not validated sufficiently. To develop the accurate multiple scattering model for the atmosphere-snow system, in Chapter 1 four types of approximations of Mie phase function were investigated in calculating the multiple scattering by snow particles larger then the wavelength using the "doubling" method. In the following Chapter 2, the multiple scattering model for the atmosphere-snow system, in which the interaction between the atmosphere and the snow is considered, was developed based on the result of Chapter 1. Using this model the atmospheric effects on the spectral and spectrally integrated snow albedos at the snow surface and the top of the atmosphere were investigated. In Chapter 3, the spectral albedo in the wavelength region of 0.35-2.5 μm observed with the spectrometer on the snowfield under the cloudy condition at Barrow, Alaska was discussed. The effects of snow grain size and impurities on the spectral albedo were investigated by comparing the observed spectral albedo with the theoretical ones calculated by the model developed in Chapter 2, in which the snow physical parameters obtained from the snow pit work were used. In the last Chapter 4, the observational results of spectral albedo and bidirectional reflectance in the wavelength region of

$0.35 - 2.5\,\mu m$ made with snow pit work on a flat snowfield under the clear condition in eastern Hokkaido, Japan was discussed. From this results, the effects of snow grain size and snow layer structure of impurities on spectral albedo and bidirectional reflectance were investigated by comparing the observed spectral data with the theoretical ones calculated by a multiple scattering model for the atmosphere-snow system.

References

BARKSTROM, B. R. (1972): Some effects of multiple scattering on the distribution of solar radiation in snow and ice. *J. Glaciol.*, **11**, 357-368.

BARKSTROM, B. R. and QUERFELD, C. W. (1975): Concerning the effect of anisotropic scattering and finite depth on the distribution of solar radiation in snow. *J. Glaciol.*, **14**, 107-124.

BERGER, R. H. (1979): Snowpack optical properties in the infrared. *CRREL Rep.* **79-11**, U. S. Army Cold Reg. Res. and Eng. Lab., Hanover, N. H., 1-9.

BOHREN, C. F. and BARKSTROM, B. R. (1974): Theory of the optical properties of snow. *J. Geophys. Res.*, **79**, 4527-4535.

CHOUDHURY, B. J. (1981): Radiative properties of snow for clear sky solar radiation. *Cold Reg. Sci. Technol.*, **4**, 103-120.

CHOUDHURY, B. J. and CHANG, A. T. C. (1979a): Two-stream theory of reflectance of snow. *IEEE Trans. Geosci. Electron.*, **GE-17**, 63-68.

CHOUDHURY, B. J. and CHANG, A. T. C. (1979b): The solar reflectance of a snow field. *Cold Reg. Sci. Technol.*, **1**, 121-128.

CHOUDHURY, B. J. and CHANG, A. T. C. (1981a): On the angular variation of solar reflectance of snow. *J. Geophys. Res.*, **86**, 465-472.

CHOUDHURY, B. J. and CHANG, A. T. C. (1981b): The albedo of snow for partially cloudy sky. *Boundary layer Meteorol.*, **20**, 371-389.

DIRMHIRN, I. and EATON, F. D. (1975): Some characteristics of the albedo of snow. *J. Appl. Meteorol.*, **14**, 375-379.

DUNKLE, R. V. and BEVANS, J. T. (1956): An approximate analysis of the solar reflectance and transmittance of a snow cover. *J. Meteorol.*, **13**, 212-216.

GIDDINGS, J. C. and LACHAPELLE, E. (1961): Diffusion theory applied to radiant energy distribution and albedo of snow. *J. Geophys. Res.*, **66**, 181-189.

GRENFELL, T. C. (1981): A visible and near-infrared scanning photometer for field measurements of spectral albedo and irradiance under polar conditions. *J. Glaciol.*, **27**,476-481.

GRENFELL, T. C. and MAYKUT, G. A. (1977): The optical properties of ice and snow in the Arctic Basin. *J. Glaciol.*, **18**, 445-463.

GRENFELL, T. C. and PEROVICH, D. K. (1984): Spectral albedos of sea ice and incident

solar irradiance in the southern Beaufort Sea. *J. Geophys. Res.*, **89,** 3573-3580.

GRENFELL, T. C., WARREN, S. G. and MULLEN, P. C. (1994): Reflection of solar radiation by the Antarctic snow surface at ultraviolet, visible and near-infrared wavelengths. *J. Geophys. Res.*, **99**, 18669-18684.

HIGUCHI, K., FUSHIMI, H., OHATA, T., TAKENAKA, S., IWATA, S., YOKOYAMA, K., HIGUCHI, H., NAGOSHI, A. and IOZAWA, T. (1980): Glacier inventory in the Dudh Kosi region, East Nepal. *IAHS Publ.*, **126**, 95-101.

KUHN, M. (1974): Anisotropic reflection from sastrugi fields. *Antarct. J. U.S.*, **9**, 123-125.

KUHN, M. (1985): Bidirectional reflectance of polar and alpine snow surfaces. *Ann. Glaciol.*, **6**, 164-167.

KUHN, M. and SIOGAS, L. (1978): Spectroscopic studies at McMurdo, South Pole, and Siple Stations during the austral summer 1977-78. *Antarct. J. U.S.*, **13**, 178-179.

LI, S. (1982): *A model for the anisotropic reflectance of pure snow*. M.S. thesis, 60pp, Univ. of Calif., Santa Barbara.

LILJEQUIST, G. H. (1956): Energy exchange of an Antarctic snow-field: Short-wave radiation. in *Norwegian-British-Swedish Antarctic Expedition, 1949-52, Scientific Results, vol. 2, Part 1A*, Norsk Polarinstitutt, Oslo.

LEROUX, C. and FILY, M. (1998): Modeling the effect of sastrugi on snow reflectance. *J. Geophys. Res.*, **103**, 25,779-25,788.

LEROUX, C., LENOBLE, J., BROGNIEZ, G., HOVENIER, J. W. and De HAAN, J. F. (1999): A model for the bidirectional polarized reflectance of snow. *J. Quant. Spectrosc. Radiat. Transfer*, **61**, 273-285.

NAKAJIMA, T. Y., NAKAJIMA T., NAKAJIMA M., FUKUSHIMA H., KUJI M., UCHIYAMA A. and KISHINO M. (1998): Optimization of the advanced earth observing satellite II global imager channels by use of radiative transfer calculations. *Appl. Opt.*, **37**, 3149-3163.

SALOMONSON, V. V. and MARLATT, W. E. (1968): Anisotropic solar reflectance over white sand, snow and stratus clouds. *J. Appl. Meteorol.*, **7**, 475-483.

STEFFEN, K. (1987): Bidirectional reflectance of snow at 500-600 nm. in *Large Scale Effects of Seasonal Snow Cover*, edited by B. Goodison *et. al.*, IAHS Publ. 166 pp. 415-425, Int. Assoc. of Hydrol. Sci., Wallingford, England.

WARREN, S. G. (1982): Optical properties of snow. *Rev. Geophys. Space Phys.*, **20**, 67-

89.

WARREN, S. G. and WISCOMBE, W. J. (1980): A model for the spectral albedo of snow, II: Snow containing atmospheric aerosols. *J. Atmos. Sci.*, **37**, 2734-2745.

WARREN, S. G., GRENFELL, T. C. and MULLEN, P. C. (1986): Optical properties of Antarctic snow. *Antarct. J. U.S.*, **21**, 247-248.

WARREN, S. G., BRANDT, R. E. and HINTON, P. O'RAWE (1998): Effect of surface roughness on bidirectional reflectance of Antarctic snow. *J. Geophys. Res.*, **103**, 25,789-25,807.

WARRICK, R. A., Le PROVOST, C., MEIER, M. F., OERLEMANS J. and WOODWORTH, P. L. (1995): Change in sea level. Chapter. 7 in *Climate Change 1995*, Cambridge University Press, 572pp.

WISCOMBE, W. J. and WARREN, S. G. (1980): A model for the spectral albedo of snow, I: Pure snow. *J. Atmos. Sci.*, **37**, 2712-2733.

YASUNARI, T., KITOH A. and TOKIOKA, T. (1991): Local and remote responses to excessive snow mass over Eurasia appearing in the Northern spring and summer climates. - A study with MRI.GCM -. *J. Meteorol Soc. Jpn*, **69**, 473-487.

Chapter 1

Approximations of phase function in calculating the spectral albedo of snow surface with multiple scattering

Approximations of Phase Function in Calculating the Spectral Albedo of Snow Surface with Multiple Scattering

by

Teruo Aoki

Tadao Aoki

Masashi Fukabori

Papers in Meteorology and Geophysics Vol. 47, No. 3/4, pp. 141-156, March 1997

Meteorological Research Institute, Tsukuba, Ibaraki, 305 Japan

気象研究所研究報告 第47巻第3/4号 141−156頁 平成9年3月
Papers in Meteorology and Geophysics Vol. 47, No. 3/4, pp. 141−156, March 1997

Approximations of Phase Function in Calculating the Spectral Albedo of Snow Surface with Multiple Scattering

by

Teruo Aoki, Tadao Aoki and Masashi Fukabori

Meteorological Research Institute, Tsukuba, Ibaraki 305, Japan

(Received October 8, 1996 ; Revised February 3, 1997)

Abstract

Four types of approximations of the Mie phase function were studied in calculating multiple scattering by snow particles with the doubling method. These involve the two renormalizations of Hansen and Grant, the delta-M method and direct truncation. These four approximations were compared for snow surface albedo with effective grain radii of 50, 200 and 1000 μm in a wavelength region from 0.3 to 3.0 μm with the delta-Eddington approximation as a reference. In the Hansen's renormalization, the maximum albedo error exceeds 0.1 for snow with an effective radius of 1000 μm at small solar zenith angles. The delta-M method overestimates snow albedos at all solar zenith angles in a wavelength region smaller than 1.4 μm for snow with effective radius of 1000 μm. This is due to insufficient angle resolution (0.1° in a scattering angle region less than 2°) in the forward peak region of the look-up table of the Mie phase function. It has been shown that even with ten times higher resolution in the scattering angle region less than 10° a sufficiet accuracy could not be obtained for an effective radius of 1000 μm in a wavelength region smaller than 0.6 μm. Reasonable results were obtained by the Grant's renormalization and direct truncation approximation for all cases of effective grain radii studied. It was also found that these methods save computation time and memory because sufficient accuracy is obtained even with a low angle resolution of 0.1° in the forward peak region of phase function. In direct truncation, the result was not sensitive to the choice of a truncation angle between 5° and 20°.

1. Introduction

The cryosphere is known to play an important role in the climate system of the earth (Manabe and Wetherald, 1975; Yasunari *et. al.*, 1991). The modeling of spectral snow albedo has been intensively and widely investigated (Warren. 1982). Most models belong to the category of two-stream approximation. This method's weakest point is that error increases at low solar elevations. The snow albedo model by Wiscombe and Warren (1980), which incorporates the delta-Eddington approximation(Joseph *et al.*, 1976) with the Mie theory, was the most accurate model for snow albedo (Warren, 1982) at that time. The maximum error in flux reflectance with this model could, however, amount to 0.1 at a solar zenith angle of 84.3° (Joseph *et al.*, 1976). Solar elevation is generally low in high-latitude regions involving a large area of the cryosphere. A more accurate model in such low solar elevation is required to advance studies in climate or remote sensing.

For snow particle size of the order of $10^1 - 10^3$ μm, the Mie phase function of light scattering is highly asymmetric, having a very sharp peak in the

forward direction (Fig. 1). In such cases, calculation of the radiative transfer by ordinary scattering theory fails due to the very sharp forward peak of the asymmetric phase function. Many procedures have been proposed to overcome this difficulty (Hansen, 1969a; Potter, 1970; Hansen, 1971b; Wiscombe, 1977; Nakajima and Tanaka, 1988). Practically these methods have been developed for the application to radiative transfer in the cloud layer. Snow particles size is, however, one to two orders larger than that of cloud particles, so the applicability of existing methods to snow particles requires careful examination. In the present paper, we study the adequacy of current methods in calculating the spectral albedo (flux reflectance) of the snow (snowpack) surface. Calculations were made for the albedo of snow surfaces illuminated only by direct solar radiation. Thus, "snow albedo" here means the ratio of emergent radiation flux from the snow surface to direct solar flux.

2. Radiative Transfer Model

In the present model, radiative transfer in snow is treated the same as in the multiple scattering model in the atmosphere containing aerosol or cloud particles. Snow grains are assumed to be mutually independent spherical ice particles, i.e., each particle is placed in the far field of others. In reality, natural snow grains are not isolated. According to Wiscombe and Warren (1980), a model that neglects near-field effects of close packing and the nonsphericity of snow particles can be used to predict the spectral albedo of snow operationally at visible and near infrared wavelengths.

For size distribution, we use the standard size distribution given by Hansen (1971b) as

$$n(r) = constant \cdot r^{\frac{1-3b}{b}} e^{\frac{-r}{ab}}, \qquad (1)$$

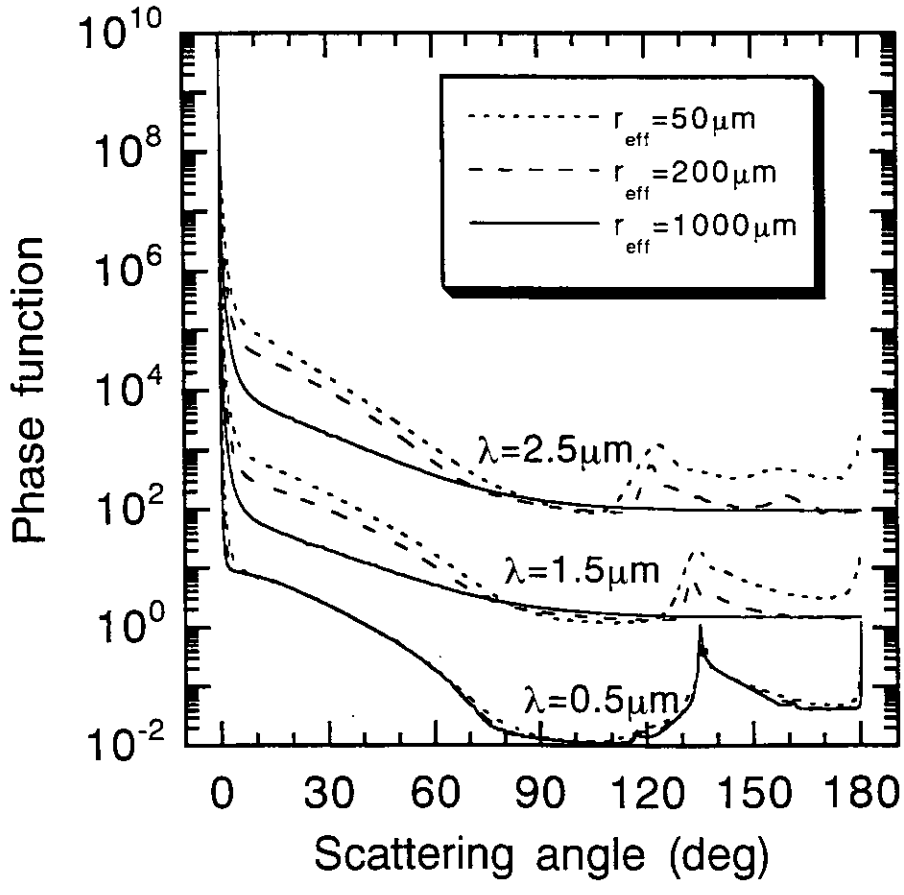

Fig. 1 Phase functions for snow particles with effective radii of r_{eff} = 50, 200 and 1000 μm with v_{eff} = 0.125 at wavelengths λ = 0.5, 1.5 and 2.5 μm. Curves are successively displaced upward by a factor of 10^2 except for λ = 0.5 μm.

where r is the radius of snow grain particle. It can easily be shown that, for the size distribution (1) the effective raius r_{eff} is given by a and the effective variance ν_{eff} by b. The complex refractive index of ice compiled by Warren(1984) is used to calculate parameters for single scattering in the Mie theory. To calculate multiple scattering, the doubling method (e.g., Hansen, 1969b; Hansen, 1971a; Hansen and Travis, 1974) is used omitting polarization. Numerical integration over the scattering angle to calculate the radiant flux density is conducted using a Gaussian quadrature of 16 points (32 streams) in the zenith angle and 513 points in the azimuth angle from zero to 180° for the expansion of Fourier series. We calculated spectral snow albedos without atmosphere for three values of effective radii of $r_{eff} = 50$, 200 and 1000 μm with effective variance $\nu_{eff} = 0.125$ at wavelengths every 0.025 μm from 0.3 to 3.0 μm. Accord-

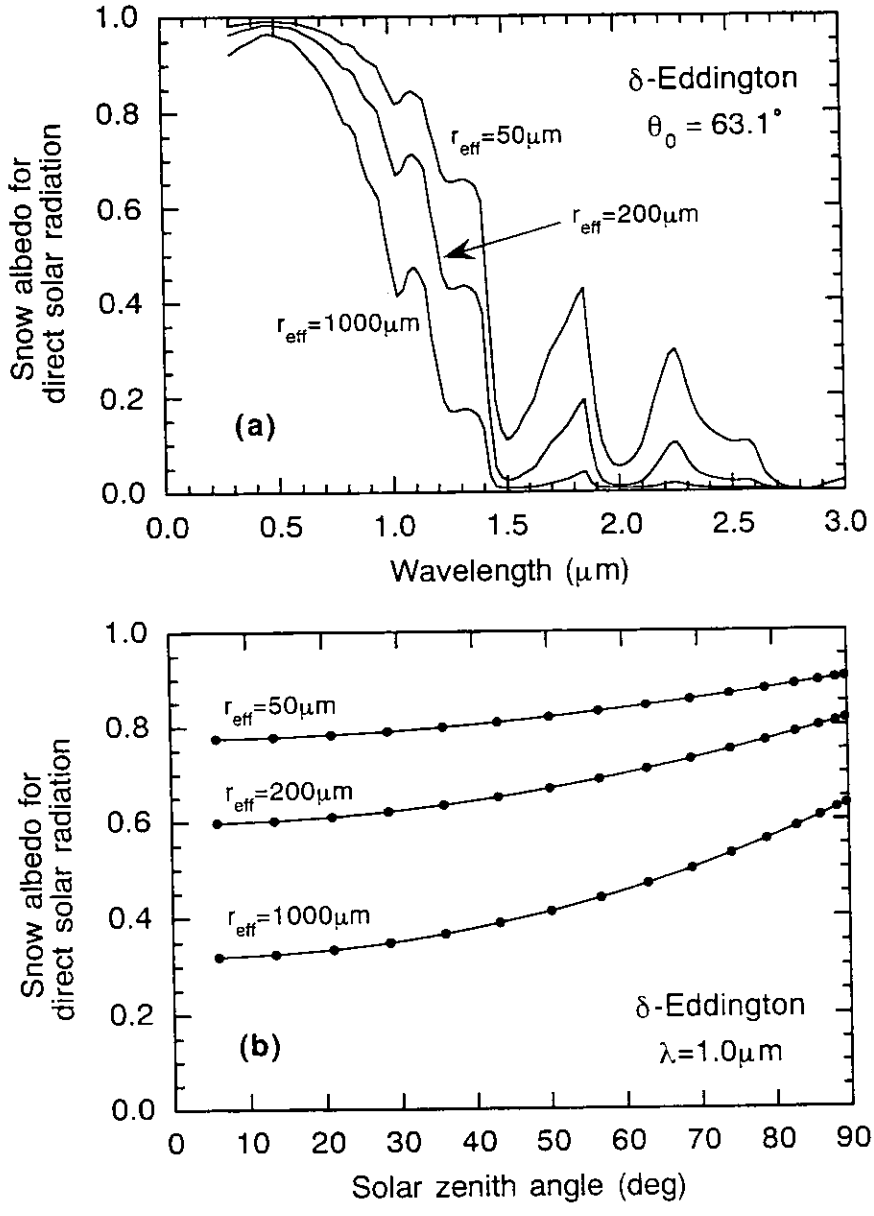

Fig. 2 Snow albedos for direct solar radiation calculated by the DE approximation as functions of (a) wavelength at solar zenith angle $\theta_0 = 63.1°$ and (b) the solar zenith angle at wavelength $\lambda = 1.0\mu$m.

ing to Wiscombe and Warren (1980), these three values correspond to new snow, fine grained older snow and old snow for the melting point. The snow layer is homogeneous and plane-parallel. Its optical depth is 3200 at wavelength $\lambda = 0.5\,\mu$m for all grain sizes and is large enough (semi-infinite) for the snow surface albedo to converge at a constant value. Radiative transfer is difficult to calculate directly for highly asymmetric phase functions such as cloud particles. To avoid this difficulty, Hansen (1969a) and Potter (1979), for example, used direct truncation (TR) approximation of a forward peak of phase function. Hansen (1971b) also adopted renormalization (H-RN) approximation that replaced the phase function with a modified form, keeping energy constant. Grant's renormalization (G-RN) approximation (Wiscombe, 1976), for another example, corrects only azimuthally integrated phase functions, including forward and backscattered directions. Wiscombe (1977) proposed automatic truncation approximation, the delta-M (DM) method, that does not require a precise truncation angle value. In our present study, we calculate spectral snow albedos by the doubling methods incorporating the H-RN, G-RN, DM and TR appoximations, and examine their effectiveness in computation accuracy and efficiency.

Since snow particle size is one to two order larger than that of cloud particles, its phase function has a much stronger forward peak than cloud particles (Fig. 1). This requires a very fine scattering angle mesh for calculating multiple scattering by ordinary method of radiative transfer, which consumes enormous computation time. Even with such high mesh points as used in our model, accuracy is not sufficient in radiative transfer calculation for snow albedo by the doubling method without approximation of phase function. In practice, then, snow albedo cannot be solved precisely. We thus use, as a reference, the delta-Eddington (DE) approximation (Joseph *et al.*, 1976), which is a kind of two-stream approximation with the lowest order of approximation in the DM method. This is advantageous in handling anisotropic single scattering parameters. Unfortunately, this method includes systematic error due to two-stream approximation model properties. Joseph *et al.* (1976) studied the albedo error of the DE approximation by comparing it with the doubling method using the Henyey-Greenstain phase function for some single scattering parameters. Albedo calculated by the DE approximation was found to be accurate for small solar zenith angles, but was underestimated, with a maximum error of 0.1, at the solar zenith angle of 84.3°. This error occurs for an optical depth of 10, a single scattering albedo of 0.8-0.99 and an asymmetry factor of 0.8-0.95. Values for single scattering albedo and asymmetry factor correspond to wave lengths where differences in snow albedo between the DE approximation and the doubling method with the Mie phase function are large, as will be shown in the following sections. The DE approximation uses the asymmetry factor and single scattering albedo, not the phase function itself. Provided that these two parameters are exact, the calculated result does not include error caused by the phase function shape. Naturally, due to the use of two-stream approximation, the accuracy of DE approximation deteriorates at large solar zenith angles. Thus, by calculating these two parameters using the Mie theory, we will be able to obtain accurate albedo values by the DE approximation, except for large solar zenith angles.

The DE approximation has been used by Wiscombe and Warren (1980) to calculate spectral snow albedo using the Mie parameters. The spectral snow albedo calculated with this model agreed well with that observed under cloudy conditions (Grenfell and Warren, 1994).

Snow albedos calculated in this study with the DE approximation (Figs. 2a-b), enable us to determine the characteristics of dependence of snow albedo on wavelength and solar zenith angle. We will therefore use the DE approximation not as the exact model but just as a reference to investigate the appropriateness of the H-RN, G-RN, DM and TR approximations.

3. The H-RN Approximation

Hansen (1971b) proposed renormalization approximation in calculationg radiative transfer through cloud particles with the doubling method to avoid error due to highly asymmetric phase function. The phase function is first integrated in each solid angle of the reflection and transmission hemispheres for incident light with the same grids in azimuth and zenith angles as those of multiple scattering calculation, and is iteratively corrected so as to become the sum of both integrals unity. Here, the reflection hemisphere is defined by the upward hemisphere and transmission hemisphere by the downward hemisphere. With large particles, the forward peak is so sharp that error occurs in the transmission hemisphere but is negligible in the reflection hemisphere. The phase function therefore needs to be corrected only for the transmission hemisphere. The fractions of scattered radiation in the reflection and transmission hemispheres are given by

$$r = \frac{1}{2\pi}\int_0^{2\pi} P_r(\Theta)\,d\Omega, \qquad (2)$$

$$t = \frac{1}{2\pi}\int_0^{2\pi} P_t(\Theta)d\Omega, \quad (3)$$

where $P_r(\Theta)$ and $P_t(\Theta)$ are the phase functions in the reflection and transmission hemispheres, Θ is the scattering angle, and Ω is the solid angle. The phase function $P(\Theta)=P_r(\Theta)+P_t(\Theta)$ is normalized to satisfy the following equation

$$\frac{1}{4\pi}\int_0^{4\pi} P(\Theta)d\Omega = 1. \quad (4)$$

The corrected phase function at the m-th step of the iteration is given by

$${}^mP_t(\Theta) = {}^{m-1}P_t(\Theta)f_c, \quad (5)$$

with correction factor $f_c = (1-r)/t$. Corrected phase function ${}^mP_t(\Theta)$ is successively substututed into Eq.(3) until $|1-r-t|$ becomes small enough (Appendix B, Hansen (1971b)).

The difference in snow albedo between the DE approximation and the doubling + H-RN approximation is shown in Fig. 3 as a function of wavelength. Comparison with Fig. 2a shows that the difference in snow albedo (Fig.3) is small in wavelength regions where snow albedo is close to 1.0 or zero, light absorption by single paricles is so weak or so strong that snow albedo converges at 1.0 or zero, being almost independent of the types of model. This makes the difference in snow albedo small. In other wavelength regions, the difference in snow albedo generally increases with the solar zenith angle. This may come from the fact that the DE approximation underestimates albedo, as noted in Section 2. Agreement becomes still worse, however, even at small solar zenith angles. The maximum difference in snow albedo exceeds 0.1 for $r_{eff} = 1000\,\mu$m at $\theta_0 = 5.9°$. This difference is considered to be the real error in the H-RN approximation since the DE approximation is accurate at small solar zenith angles. To obtain the reason for such a large discrepancy, we examined the initial values of r and t given by Eqs.(2) and (3). The values of t were of the order of $10^{-1}-10^{1}$ for $r_{eff} = 50\,\mu$m, $10^{0}-10^{2}$ for $r_{eff} = 200\,\mu$m and $10^{1}-10^{4}$ for $r_{eff} = 1000\,\mu$m. The values of r for these three grain sizes were all reasonable, less than 1.0. These mean that correction factor f_c ranges from 10^{0} to 10^{-4} and that the resulting total phase function will have a large discontinuity at the boundary between upward and downward hemispheres for most cases. This will cause error in calculating multiple scattering. In a few cases, f_c closes to 1.0 for $r_{eff} = 50\,\mu$m and $\lambda > 1.0\,\mu$m at $\theta_0 = 89.7°$. In these cases, absolute values of the difference in snow albedo exceed 0.2 at some wavelenghts, suggesting that snow albedo is far larger than that with the DE approximation in a case of sunlight grazing the snow surface.

4. The G-RN Approximation

In the Grant's renormalization approximation, described by Wiscombe (1976), correction is made only for azimuthally integrated phase functions, including forward and backscattered directions, so as to conserve the sum of fractions of scattered radiation in reflection and transmission hemispheres. Since the sharp forward peak of phase function causes error in calculating snow albedo, we corrected only the phase function element including the forwared peak. No discontinuity exists at the boundary between upward and downward hemispheres in the G-RN approximation. The problem caused by such a discontinuity in the H-RN approximation thus does not arise here. The G-RN approximation is the simplest of the four approximations studied. Details of numerical calculation of the G-RN approximation are given in Section 6 of Wiscombe (1976).

Large differences in snow albedo from the DE approximation at small solar zenith angles in the H-RN approximation (Fig. 3) are not found in the G-RN approximation (Fig. 4). In the DE approximation, the calculated albedo is known to be accurate at small solar zenith angles but underestimated at large solar zenith angles (Section 2). According to Joseph *et al.* (1976), the albedo error in the DE approximation at $\theta_0 = 84.3°$ was estimated as about 0.1 when compared with the doubling method using the Henyey-Greenstain phase function. The single scattering albedo and asymmetry factor for which the DE approximation makes such this error appear at wavelength where snow albedo differences (Fig. 4) are large. In our calculation, maximum differences at $\theta_0 = 86.2°$ in snow albedo between the DE approximation about and the doubling + G-RN approximation are about 0.1 for $r_{eff} = 50\,\mu$m and 0.08-0.09 for $r_{eff} = 200$ and $1000\,\mu$m (third curves from the bottom in each graph in Fig.4). These results show that the G-RN approximation is more suitable than the H-RN approximation for such large particles as snow.

5. The DM Approximation

In the delta-M method proposed by Wiscombe (1977), the phase function is approximated by a sum of the delta function for the forward peak and low order polynomials for the remainder. In general, phase function $P(\cos\Theta)$ is approximated by

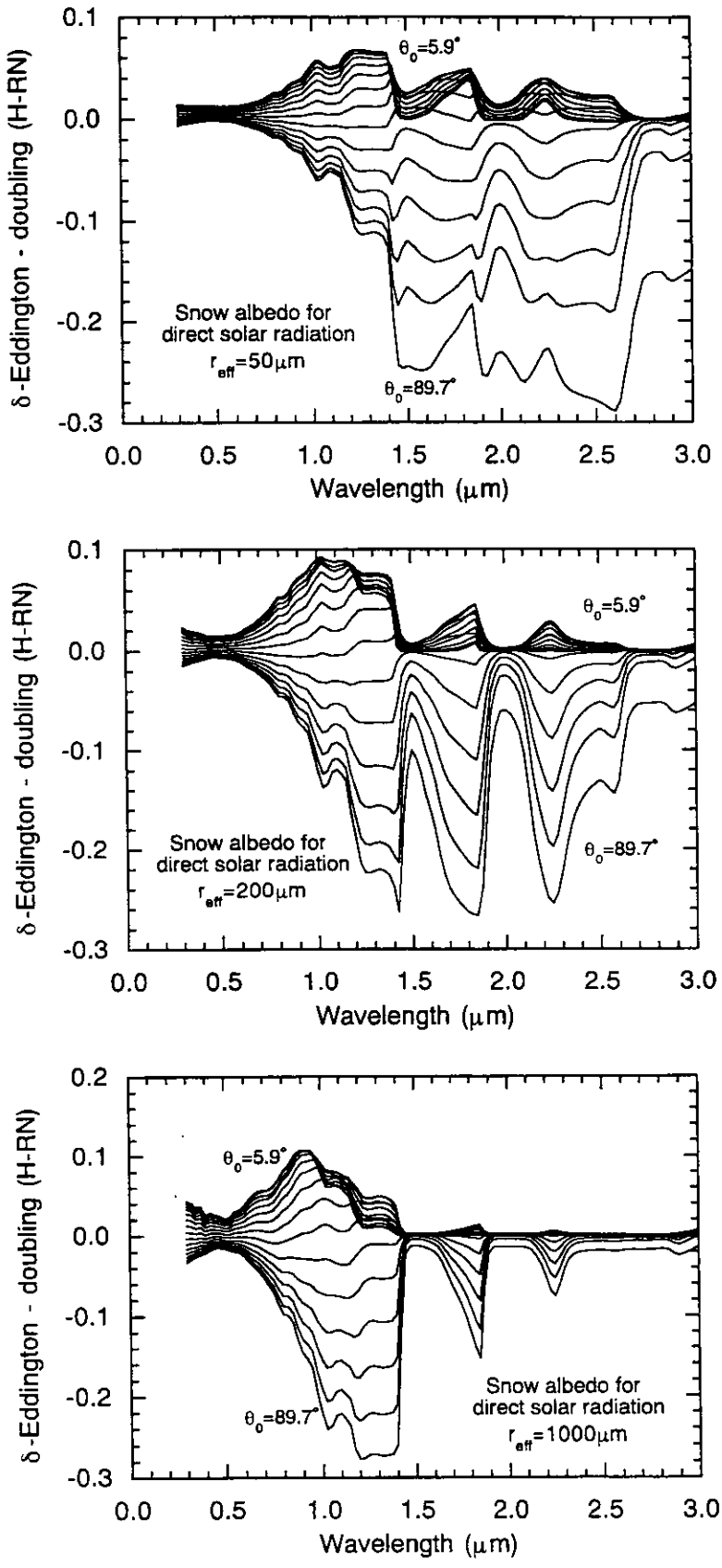

Fig. 3 Differences in snow albedos for direct solar radiation between the DE approximation and the doubling + H-RN approximation as a function of wavelength. Curves are plotted for 16 solar zenith angles (θ_0), where cosines correspond to Gaussian points for the zenith angle indicated by solid circles in Fig. 2(b).

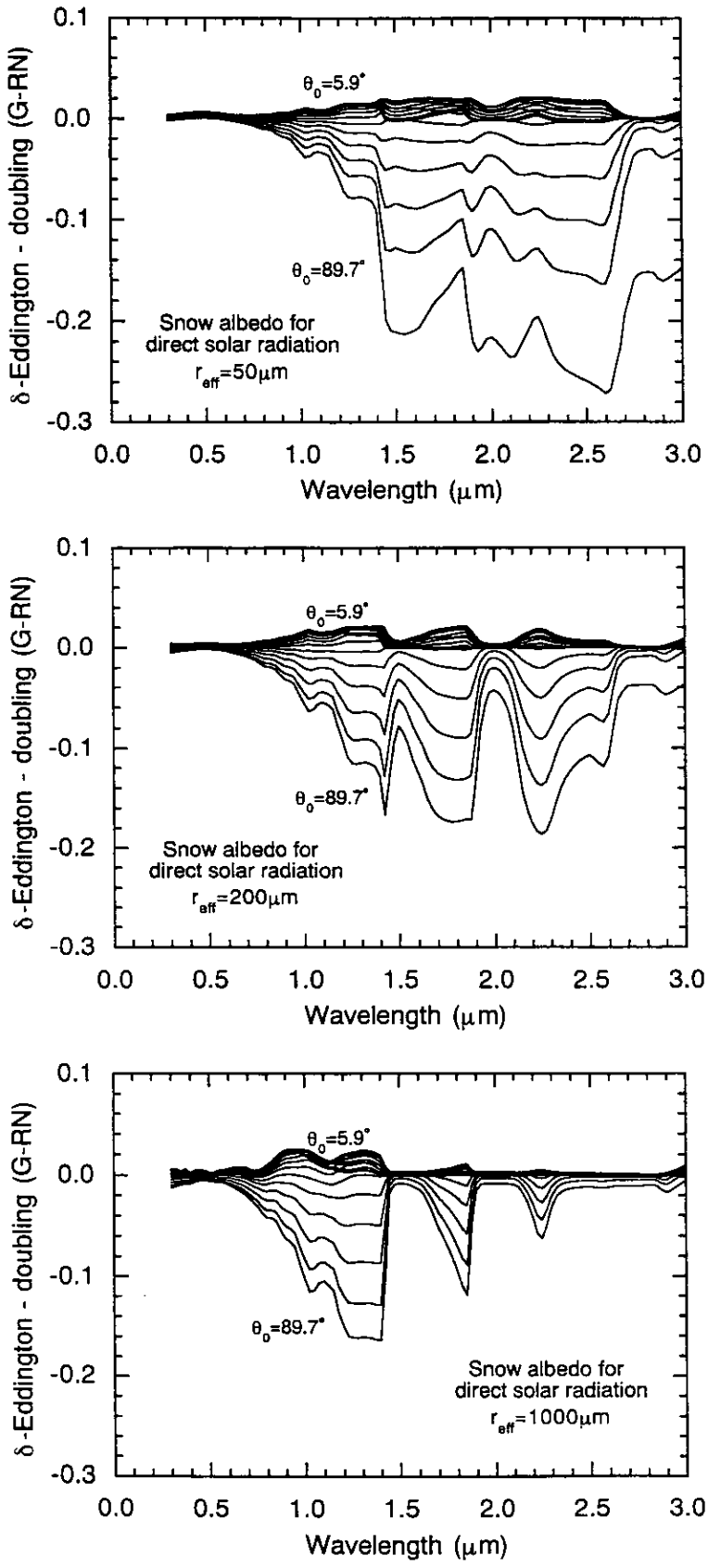

Fig. 4 Same as in Fig. 3, but calculated with the G-RN approximation instead of the H-RN approximation.

$$P^*(\cos\Theta) = 2f\delta(1-\cos\Theta) + (1-f)\sum_{n=0}^{2M-1}(2n+1)\chi_n^* P_n(\cos\Theta), \quad (6)$$

where f is the truncation fraction in phase function, δ is a delta function, Θ is the scattering angle and $P_n(\cos\Theta)$ is the Legendre polynomial of n-th degree. Coefficients χ_n^* and truncation fraction f are given by

$$\chi_n^* = \frac{\chi_n - f}{1-f}, \quad (7)$$

where $n = 0, \ldots\ldots, 2M-1$ and

$$f = \chi_{2M}, \quad (8)$$

where M is the order of approximation and we use $M=16$ as equal to the Gaussian quadrature points in zenith angle adopted in our calculation of multiple scattering. In Eq.(7), χ_n is the moment of the expansion of $P(\cos\Theta)$ by Legendre polynomial $P_n(\cos\Theta)$:

$$\chi_n = \frac{1}{2}\int_0^{\pi} P(\cos\Theta)P_n(\cos\Theta)\sin\Theta d\Theta. \quad (9)$$

Scaled optical depth $d\tau^*$, and scaled single scattering albedo ω^*, used in radiative transfer calculation using the truncated phase function, are given by

$$d\tau^* = (1-f\omega)d\tau, \quad (10)$$

and

$$\omega^* = \frac{(1-f)\omega}{1-f\omega}, \quad (11)$$

where $d\tau$ is an optical depth of snow and ω is single scattering albedo.

In calculating snow albedo with the doubling method using the truncated phase function by the DM approximation, we applied the H-RN procedure to correct for possible error and check energy conservation is computation, although Wiscombe (1977) noted this is not necessary. The same correction was applied to phase functions of both the reflection and transmission hemispheres, because the truncated phase function no longer has a forward peak. The amount of correction is represented by the so-called correction factor defined by $f_c = 1/(r+t)$, which is a good indicator for energy conservation. Correction factor values are very close to 1.0 and $1-f_c$ was of the order of $10^{-3}-10^{-4}$ for all cases.

The difference in snow albedo between the DE approximation and the doubling + DM approximation (Fig. 5) shows that, for $r_{eff} = 50$ and $200\,\mu$m, differences at small solar zenith angles are considerably smaller than those of the H-RN approximation (Fig. 3) and are close to those of the G-RN approximation (Fig. 4). For $r_{eff} = 200\,\mu$m, snow albedos of the DE approximation are, however, slightly smaller than those of the doubling + DM approximation at any solar zenith angle around $\lambda = 0.3$ and $0.8-0.9\,\mu$m. For $r_{eff} = 1000\,\mu$m, snow albedos of the DE approximation are smaller than those of the doubling + DM approximation for $\lambda < 1.4\,\mu$m. Since the DE approximation is accurate at small solar zenith angles, these results seem due to defects in the DM approximation. At least, these snow albedo differences should be small at visible wavelengths because light absorption by single particle is so weak that calculated snow albedos converge at 1.0, independent of the types of model, as mentioned in Section 3.

In the above calculations, we used a look-up table of phase function (Mie table) with a scattering angle resolution $\Delta\Theta = 0.1^\circ$ for $0 \leq \Theta \leq 2^\circ$ and $178 \leq \Theta \leq 180^\circ$, $\Delta\Theta = 0.2^\circ$ for $2 \leq \Theta \leq 5^\circ$ and $175 \leq \Theta \leq 178^\circ$, $\Delta\Theta = 0.5^\circ$ for $5 \leq \Theta \leq 10^\circ$ and $170 \leq \Theta \leq 175^\circ$, and $\Delta\Theta = 1^\circ$ for $10 \leq \Theta \leq 170^\circ$. These angle resolutions are generally sufficient for cloud or aerosol particles. Truncation fraction f calculated by Eq. (8) (Fig. 6a) should, because forward peak value of phase function increases with grain size, also increase with grain size, whereas f for $r_{eff} = 200\,\mu$m (Fig. 6a) is lower than that for $r_{eff} = 50\,\mu$m in region $\lambda < 1.0\,\mu$m. For $r_{eff} = 1000\,\mu$m, f is also lower than for both $r_{eff} = 200$ and $50\,\mu$m at some wavelengths. If f is underestimated, $d\tau^*$ and ω^* are overetimated. Since $d\tau$ is large enough, the overestimation of $d\tau^*$ has no effect on snow albedo. Overestimating ω^* will, however, increase snow albedo (Fig. 5).

As the reason of the underestimate of f it is supposed that the numerical integration in Eq.(9) was not performed accurately due to the lack of angle resolution in the forward peak of phase function. To check this supposition, we recalculated the snow albedo with a Mie table of ten times higher angle resolution of phase function in the forward region $0 \leq \Theta \leq 10^\circ$. The truncation fractions calculated with the Mie table of high angle resolution are shown in Fig. 6b. The value of f increases with grain size except for $r_{eff} = 1000\,\mu$m and $\lambda < 0.6\,\mu$m. Although we also calculated f with a higher truncation order of $M \gg 16$, the improvement was negligible. This shows that, for $r_{eff} = 1000\,\mu$m and $\lambda < 0.6\,\mu$m, the angle resolution in the forward peak of phase function is still insufficient and causes f to be underestimated.

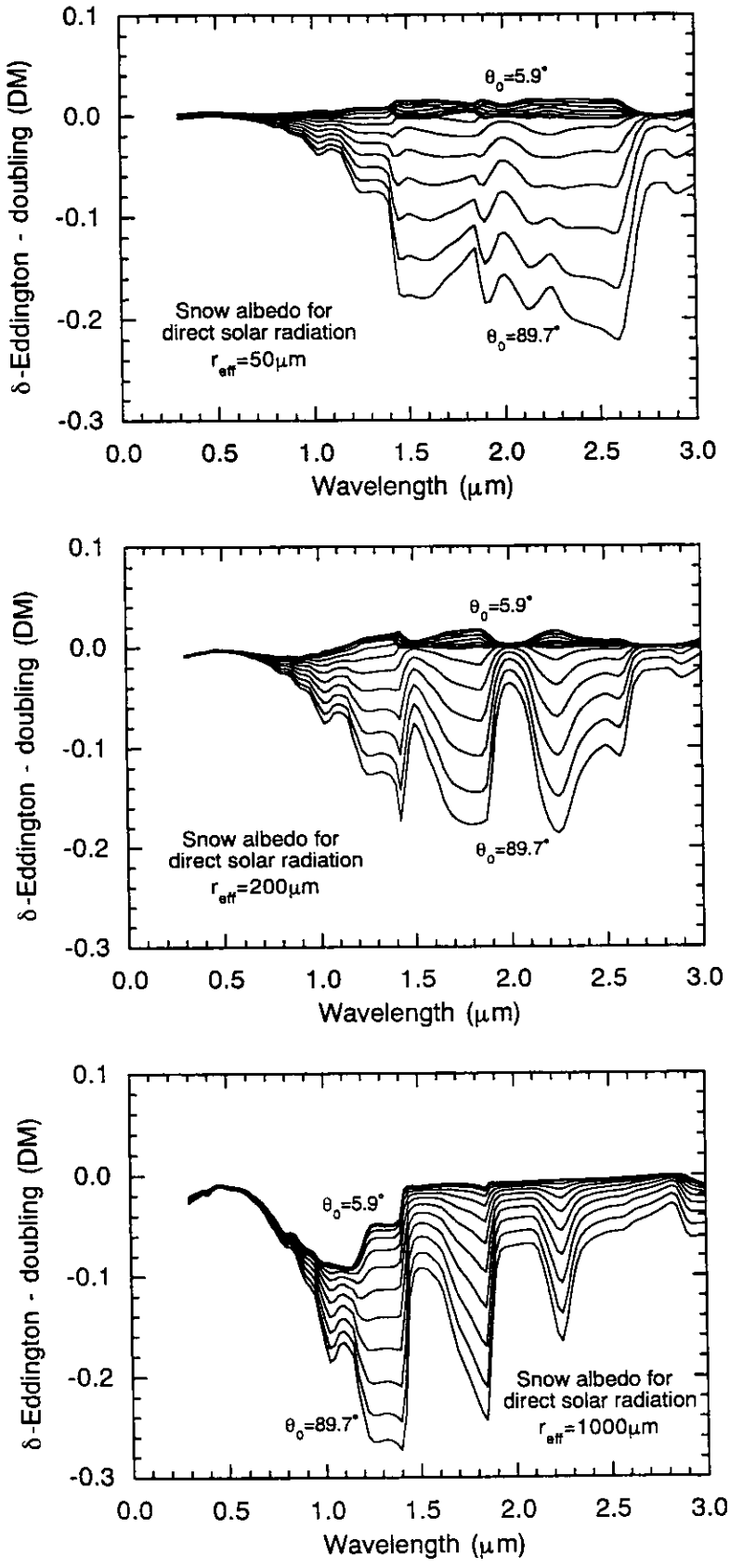

Fig. 5 Same as in Fig. 3, but calculated with the DM approximation instead of the H-RN approximation.

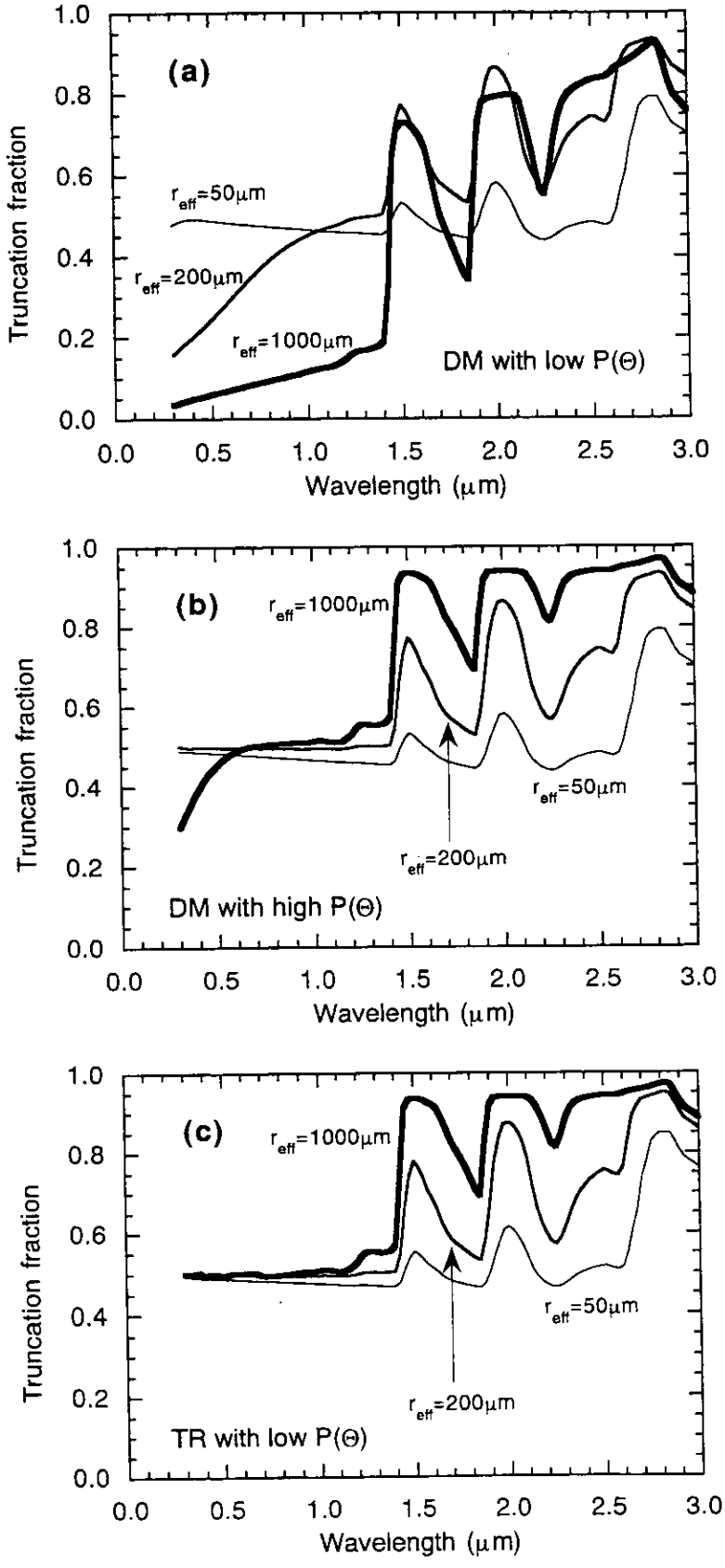

Fig. 6 Truncation fractions used in the DM approximation with the Mie tables for (a) original ($\Delta\Theta=0.1^\circ$ for $0\leq\Theta\leq2^\circ$) and (b) ten times higher angle resolution in forward region $0\leq\Theta\leq10^\circ$, and (c) used in the TR approximation.

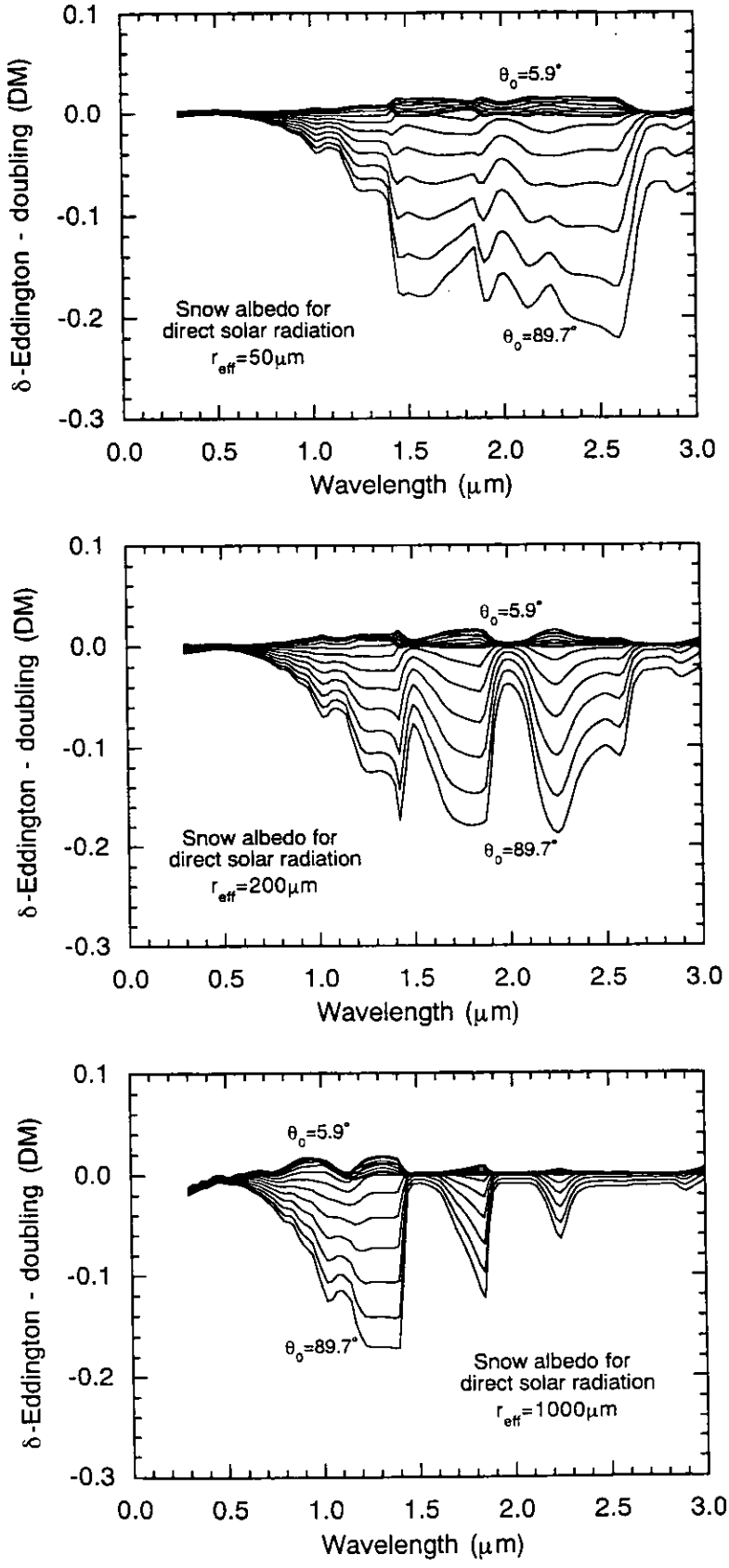

Fig. 7 Same as in Fig. 5, but calculated with the Mie table of ten times higher angle resolution than in Fig. 5 in forward region $0 \leq \Theta \leq 10^{\circ}$.

The difference in snow albedo between the doubling + DM approximation for these phase functions and the DE approximation (Fig. 7) indicates that, for $r_{eff} = 50\,\mu$m, results with the Mie table of high angle resolution are almost the same as those with low resolution (Fig. 5). For $r_{eff} = 200\,\mu$m, the inappropriate albedo behavior found in the Mie table of low angle resolution around $\lambda = 0.3$ and $0.8-0.9\,\mu$m has improved. The improvement can actually be seen in the wide wavelength region $\lambda < 1.2\,\mu$m. For $r_{eff} = 1000\,\mu$m, an improvement is seen at all wavelengths, but the defect still remains in the region $\lambda < 0.4\,\mu$m. This wavelength region does not agree with that of underestimated f ($\lambda < 0.6\,\mu$m) for $r_{eff} = 1000\,\mu$m because snow albedo is close to 1.0 due to the large single scattering albedo in the region $0.4 < \lambda < 0.6\,\mu$m. For some wavelengths in $\lambda > 1.5\,\mu$m and $r_{eff} = 1000\,\mu$m, the difference in snow albedo between two methods is small (Fig. 7), because snow albedo is close to zero due to low single scattering albedo. So far, we have found that the value of f for $r_{eff} = 1000\,\mu$m is lower than that for $r_{eff} = 200\,\mu$m in the regions $\lambda < 0.6\,\mu$m and snow albedo by the doubling + DM approximation is higher than that of the DE approximation in the regions $\lambda < 0.4\,\mu$m. Together, these facts indicate that it is still necessary to increase the angle resolution above 0.01° in the forward peak region. This requires much more computation time for the Mie calculation and large memory for storing the Mie table, which is not practical in our computer system. We looked for another way to calculate snow albedo accurately with the Mie table of low angle resolution.

6. The TR Approximation

The last method we studied is truncation method proposed by Hansen (1969a) and Potter (1970). The truncated phase function is obtained by making the slope of the logarithm of the phase function constant for $\Theta < \theta_t$ and equal to that of the untruncated phase function at θ_t. Here, θ_t is the truncation angle and the problem is how to determine the value of θ_t. A smaller truncation angle keeps the phase function shape closer to the original one, particularly for low solar elevations, where the effect of single scattering becomes dominant. If it is too small, however, an error in numerical integration occurs due to the for ward peak remainder of phase function. We must thus seek a suitable trade-off point between two effects. We studied the effects of truncation angles $\theta_t = 2.5$, 5.0, 7.5, 10, 15, 20 and 30° for snow albedo (Fig. 8). Results show that snow albedos for all truncation angles except for $\theta_t = 2.5°$ agree other at $\lambda = 0.5$ and $1.5\,\mu$m. However, at $\lambda = 1.0\,\mu$m, snow albedos for $\theta_t = 2.5$ and 30° differ from those for other truncation angles. In the region $\lambda > 1.5\,\mu$m, results similar to $\lambda = 1.5\,\mu$m were obtained. We also checked $r_{eff} = 50\,\mu$m and $200\,\mu$m, but observed no remarkable difference from $r_{eff} = 1000\,\mu$m. Thus, calculated snow albedos are not so sensitive to the truncation angle choice in the region $5 \leq \Theta \leq 20°$. Below we used 7.5° for θ_t.

We applied the H-RN approximation to the truncated phase function as for the DM approximation to avoid error and check energy conservation in integral as before. The initial values of $r + t$ in iteration of the H-RN approximation were close to 1.0 for all grain sizes studied, and the deviations of the correction factor from 1.0, $1 - f_t$, were of the order less than 10^{-4}, where the correction factor is the same definition as for the DM approximation.

In the TR approximation, scaled parameters are given by Eqs. (10) and (11) as before. Truncation fraction f was calculated from integration of truncated phase function. Numerical integration, in this case, is easy because there is no sharp forward peak in phase function. The values of f increases with grain size at all wavelength (Fig. 6c). The difference in snow albedo between the DE approximation and the doubling + TR approximation is shown in Fig. 9 as a function of wavelength. The differences in snow albedo between the two methods are almost the same as for the doubling + DM approximation with the Mie table of high angle resolution for all three grain sizes (Fig. 7) except for $\lambda < 0.4\,\mu$m and $r_{eff} = 1000\,\mu$m. For $\lambda < 0.4\,\mu$m and $r_{eff} = 1000\,\mu$m, the defect found in the DM approximation with the Mie table of high angle resolution has improved. These results show that the TR approximation is more appropriate than the DM method for large particles.

When we compare albedos of the TR approximation with the G-RN approximation, they agree with within 0.02 in all cases except for $\theta_0 = 89.7°$ in $r_{eff} = 50\,\mu$m. For $\theta_0 = 89.7°$ and $r_{eff} = 50\,\mu$m, the difference in snow albedo between the doubling + TR approximation and the DE approximation is larger than that for the G-RN approximation. This means that snow albedo of the TR approximation is smaller than for the G-RN approximation. This reason is considered as followings; the TR approximation treats scatterd light near the forward peak as direct light only in the forward direction. In the case of sunlight grazing the snow surface, the single scattered component, originally upward, is also calculated as the downward component. This is especially notable with small particles which have a relatively weaker forward peak of phase function than large particles. The TR ap-

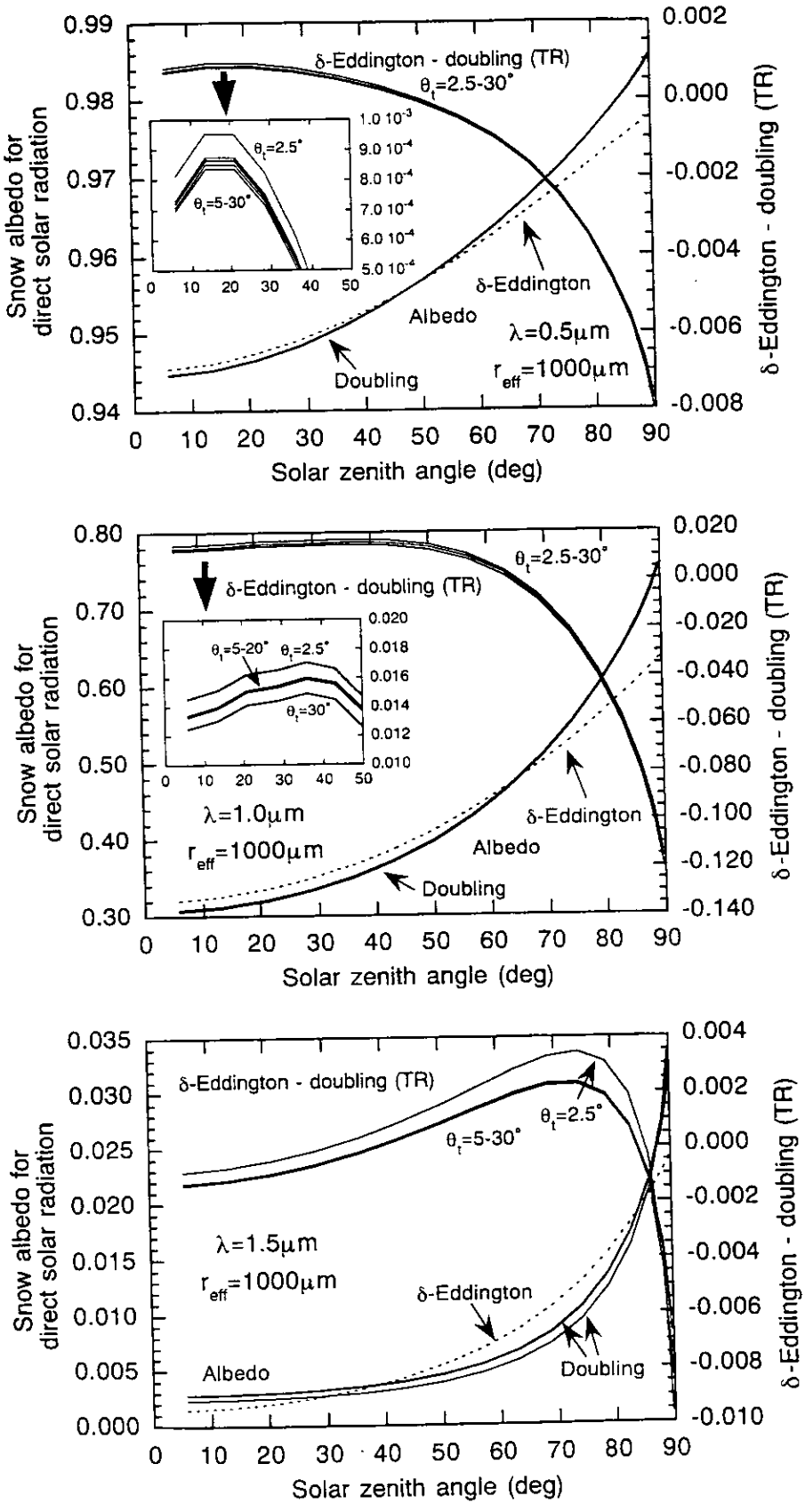

Fig. 8 Effects of truncation angles on snow albedo (left ordinate) for direct solar radiation calculated by the doubling + TR approximation. Albedo differences from those of the DE approximation are indicated on the right ordinate. Same snow albedo curves are enlarged (insets).

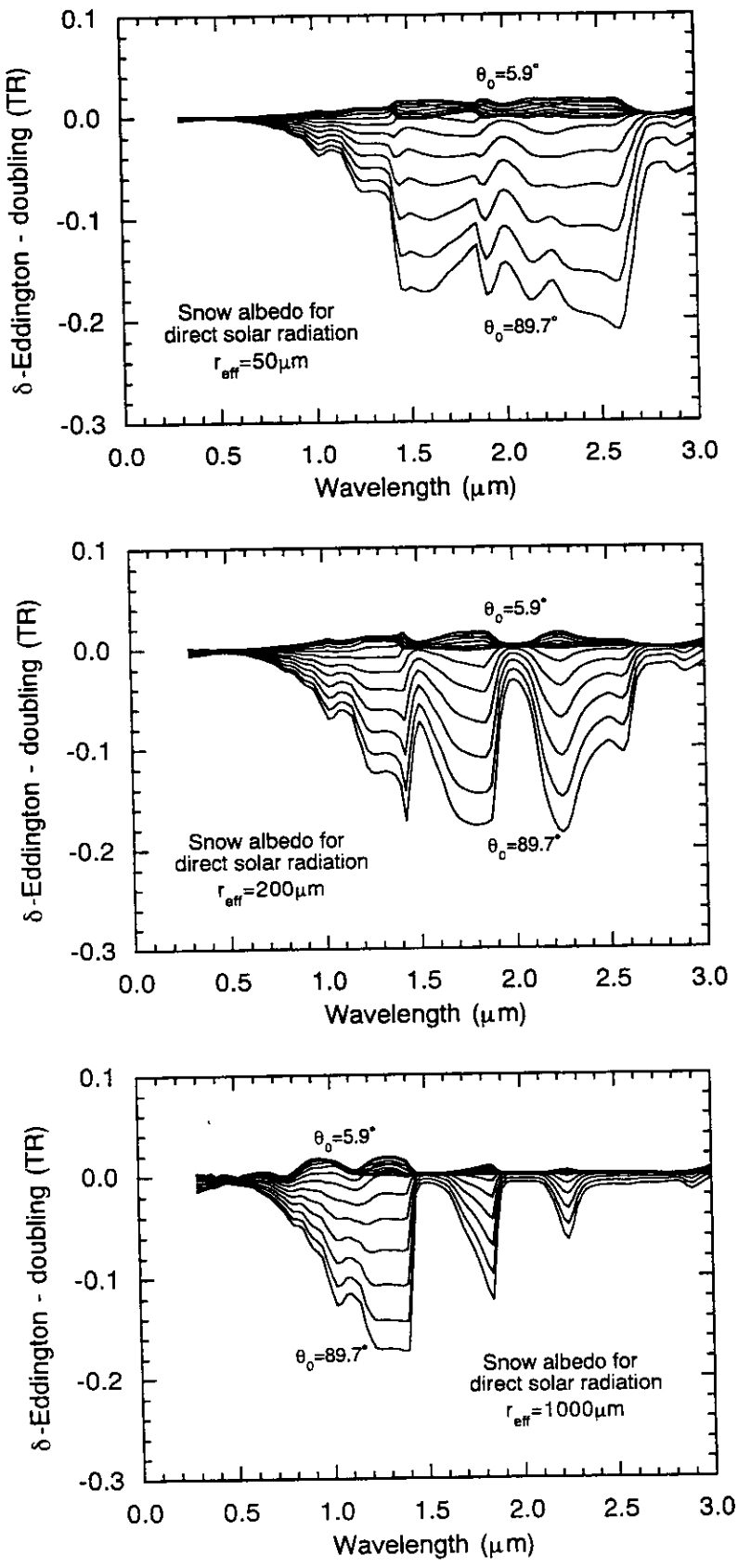

Fig. 9 Same as in Fig. 3, but calculated with the TR approximation instead of the H-RN approximation.

proximation may still underestimate snow albedo in the case of sunlight grazing the snow surface as suggested in Section 3. Since this is an extreme case practically impossible to verify experimentally, we do not take the result of calculation seriously. The maximum differences in snow albedo between the DE approximation and the doubling + TR approximation at $\theta_0 = 86.2^\circ$ are about 0.1 (third curves from the bottom in each graph in Fig. 9) for all three grain sizes. This is close to both results by Joseph *et al.* (1976) and the G-RN approximation in this paper.

Thus far, we have found no clear difference in accuracy and efficiency between the G-RN and TR approximations. At this stage, it can be safety to be concluded that both approximations are more appropriate for snow albedo calculation than the H-RN and DM approximations.

7. Summary

Four types of approximations of phase function — the H-RN, G-RN, DM and TR methods — have been investigated in multiple scattering calculation for snow particles of $r_{eff} = 50$, 200 and 1000 μm, by comparing with the DE approximation. In the H-RN approximation with the doubling method, the maximum deviation from the DE approximation for $r_{eff} = 1000\,\mu$m at small solar zenith angles exceeded 0.1. This is considered the real error in the H-RN approximation, because the DE approximation is expected to be more accurate for small solar zenith angles. To learn why such a large discrepancy occured, we studied correction factor f_c for phase function. The values of f_c ranged from 10^0 to 10^{-4}. Such small values occur because the sharp forward peak of phase function cannot be accurately numerically integrated in the model. In the G-RN approximation, a reasonable result was obtained for almost all conditions of r_{eff}, λ and θ_0. This is the simplest of the four approximations. The DM approximation seems to work well for $r_{eff} = 50\,\mu$m. For $r_{eff} = 1000\,\mu$m, however, snow albedo of the DM approximation is always larger than that of the DE approximation for any solar zenith angle in the region $\lambda < 1.4\,\mu$m. This seems to indicate that the DM approximation is not suitable for grain size as large as $r_{eff} = 1000\,\mu$m. Snow albedos and truncation fractions calculated using two Mie tables with angle resolutions of $\Delta\Theta = 0.1$ and 0.01° in the forward peak region $0 \leq \Theta \leq 2^\circ$ revealed that, for $r_{eff} = 1000\,\mu$m, an angle resolution higher than 0.01° is still needed in the region $\lambda < 0.6\,\mu$m. With the TR approximation, reasonable results were obtained for truncation fraction f and snow albedo for any grain size or wavelength. This result is not sensitive to the truncation angle in the wide range of $5 \leq \Theta \leq 20^\circ$ for all grain sizes.

We thus conclude that both the G-RN and TR approximations are applicable for radiative transfer calculation through the snow layer of large grain radii with the Mie tale of 0.1° angle resolution in the forward peak region. However, in the case of sunlight grazing the snow surface, the TR approximation may still underestimate the albedo due to the lack of a sharp forward peak in phase function.

Acknowledgements

We thank Dr. S. Warren for providing us with the Mie and albedo data to validate our model. We also thank Dr. A.Uchiyama for his invaluable advice.

References

Grenfell, T. C., S. G. Warren and P. C. Mullen, 1994: Relfection of solar radiation by the Antarctic snow surface at ultraviolet, visible, and near-infrared wavelengths. *J. Geophys. Res.*, **99**, 18669-18684.

Hansen, J. E., 1969a: Exact and approximate solutions for multiple scattering by cloudey and hazy planetary atmosphere. *J. Atmos. Sci.*, **26**, 478-487.

Hansen, J. E., 1969b: Radiative transfer by doubling very thin layers. *Astrophys. J.*, **155**, 565-573.

Hansen, J. E., 1971a: Multiple scattering of polarized light in planetary atmospheres. Part I. The doubling method. *J. Atmos. Sci.*, **28**, 120-125.

Hansen, J. E., 1971b: Multiple scattering of polarized light in planetary atmospheres. Part II. Sunlight reflected by terrestrial water clouds. *J. Atmos. Sci.*, **28**, 1400-1426.

Hansen, J. E. and L. D. Travis, 1974: Light scattering in planetary atmospheres. *Space Sci. Rev.*, **16**, 527-610.

Joseph, J. H., W. J. Wiscombe and J. A. Weinman, 1976: The delta-Eddington approximation for radiative flux transfer. *J. Atmos. Sci.*, **33**, 2452-2459.

Manabe, S. and R. T. Wetherald, 1975: The effects of doubling the CO_2 concentration on the climate of a general circulation model. *J. Atmos. Sci.*, **32**, 3-15.

Nakajima, T. and M. Tanaka, 1988: Algorithms for radiative intensity calculations in moderately thick atmospheres using a truncation approximation. *J. Quant. Spectrosc. Radiat. Transfer*, **40**, 51-69.

Potter, J. F., 1970: The delta function approximation

in radiative transfer theory. *J. Atmos. Sci.*, **27**, 943-949.

Yasunari, T., A. Kitoh and T. Tokioka, 1991: Local and remote responses to excessive snow mass over Eurasia appearing in the Northern spring and summer climates. - A study with MRI.GCM -. *J. Meteor. Soc. Japan*, **69**, 473-487.

Warren, S. G., 1982: Optical properties of snow. *Rev. Geophys. Space Phys.*, **20**, 67-89.

Warren, S. G., 1984: Optical constants of ice from the ultraviolet to the microwave. *Appl. Opt.*, **23**, 1206-1225.

Wiscombe, W. J., 1976: On initialization, error and flux conservation in the doubling method. *J. Quant. Spectrosc. Radiant. Transfer*, **16**, 637-658.

Wiscombe, W. J., 1977: The delta-M method: Rapid yet accurate radiative flux calculations for strongly asymmetric phase functions. *J. Atmos. Sci.*, **34**, 1408-1422.

Wiscombe, W. J. and S. G. Warren, 1980: A model for the spectral albedo of snow. I : Pure snow. *J. Atmos. Sci.*, **37**, 2712-2733.

多重散乱によって積雪の波長別アルベドを計算するときの位相関数の近似法

青木輝夫・青木忠生・深堀正志

積雪粒子による多重散乱をdoubling法で計算するときのMie位相関数に対する4種類の近似法について調べた。これらの近似法はHansen及びGrantによる2種類の"renormalization法"、"delta-M法"、"direct truncation法"である。4つの方法の比較は、積雪アルベドを積雪粒子の有効半径50, 200, 1000μm、波長域0.3～3.0μmに対して計算し、delta-Eddington近似をreferenceとして用いて行った。Hansenの"renormalization法"の場合、粒子の有効半径1000μmの積雪に対し、太陽天頂角が小さいときにアルベドの最大誤差が0.1以上になった。"delta-M法"によるアルベドは、粒子の有効半径1000μmの積雪に対し、1.4μm以下の波長域において、全ての太陽天頂角で過大評価となった。これは計算に用いたMie位相関数のlook-up tableの前方散乱角の分解能が不十分（その分解能は散乱角2°以下の前方散乱ピークの領域で0.1°）であったためである。そこで位相関数の散乱角10°以下の領域の分解能を10倍に上げたが、粒子の有効半径1000μmの積雪に対し、0.6μm以下の波長域では十分な精度は得られなかった。3つの粒径に対し、全波長域で満足できる結果は、Grantの"renormalization法"と"direct truncation法"によって得られた。これらの方法では前方散乱ピークの領域で0.1°の分解能を持つ位相関数でも十分な精度が得られるため、計算時間及び計算機のメモリーという点からも経済的である。さらに、"direct truncation法"の場合、位相関数の前方散乱ピークの切断角が、5°～20°の範囲であれば、計算結果に対してほとんど影響がないことがわかった。

Chapter 2

Numerical simulation of the atmospheric effects on snow albedo with a multiple scattering radiative transfer model for the atmosphere-snow system

Numerical Simulation of the Atmospheric Effects on Snow Albedo with a Multiple Scattering Radiative Transfer Model for the Atmosphere-Snow System

By Teruo Aoki, Tadao Aoki, Masashi Fukabori and Akihiro Uchiyama

Meteorological Research Institute, Tsukuba, Japan

(Manuscript received 1 September 1998, in revised form 27 January 1999)

Abstract

The atmospheric effects on the spectral and spectrally integrated snow albedos at the snow surface and top of the atmosphere (TOA) are investigated. A multiple scattering radiative transfer model based on the "doubling and adding" method, combined with the Mie theory is applied to estimate the effects of absorption and scattering by atmospheric molecules, absorptive gases, aerosols and clouds.

It is shown that the spectral surface albedo is reduced by the atmospheric absorptive gases at large solar zenith angles. The solar zenith angle dependence is weakened in the wavelength region shorter than 0.5 μm by the Rayleigh scattering, and at almost all wavelengths by the atmospheric aerosols and cloud cover. H_2O rich atmosphere decreases the spectral surface albedo at large solar zenith angles in the H_2O bands, while the additional reduction of downward solar flux in the near infrared region by H_2O absorption causes the spectrally integrated surface albedo to increase by several percent. Aerosols increase the spectrally integrated surface albedo at small solar zenith angles and reduce it at large solar zenith angles, however they reduce the spectrally integrated planetary albedo, except at large solar zenith angles. Optically-thick cloud cover increases both the spectrally integrated surface and planetary albedos at any solar zenith angle.

In the visible region at small solar zenith angles, the downward solar flux on the snow surface under cloudy sky can exceed that for the clear case, and both further exceed the extraterrestrial solar flux, resulting from the multiple reflection between snow surface and the atmosphere (cloud cover). The global solar radiation on the snow surface under cloudy sky, however, never exceeds that for the clear case and that at TOA.

1. Introduction

The cryosphere plays an important role for the earth energy budget because of its high reflectance, and the large variation of its areal extent. The snow-covered region of the earth's surface, in particular, has a large seasonal variation. Its albedo also varies greatly from that of freshly fallen snow to that of melting snow. Therefore, snow cover may constitute a sensitive mechanism for influencing global climate change. The melting of polar snow and ice by global warming, and the resultant sea level rise are matters currently causing much public anxiety (Warrick *et al.*, 1995). Recently, it is reported that the variation of the snow-covered region in the Eurasian Continent has an influence on annual variation of the East Asian climate (Yasunari *et al.*, 1991; Ose, 1996), and many Himalayan glaciers are retreating (Higuchi *et al.*, 1980; Yamada *et al.*, 1992). An understanding of the snow radiative process is important for two general applications. The first is the calculation of the radiation budget of snowpack and the planetary radiation budget over snow-covered surfaces. This is important both for hydrology — because radiation is usually the dominant component in the surface energy budget of snow — and for global climate modeling. The second application is for planning the remote sensing of snowpack properties. This requires modeling of the optical properties at a high spectral detail (Warren, 1982). The programs of high spectral resolutional satellite sensors MODIS (Moderate Resolution Imaging Spectroradiometer) and GLI (Global Imager), both having 36 channels in the ultraviolet, visible, near infrared and infrared regions, will provide us the possibilities to estimate snow parameters such as grain size, impurities and layer structure from space. We, therefore, developed

Corresponding author: Teruo Aoki, Meteorological Research Institute, 1-1 Nagamine, Tsukuba, Ibaraki 305-0052, Japan. E-mail: teaoki@mri-jma.go.jp

an accurate and realistic spectral albedo model of snow in the atmosphere-snow system.

Over the past four decades, a considerable number of studies have been made on the modeling of snow surface albedo. The first attempt for calculating the spectral albedo of snow with a multiple scattering radiative transfer in the visible and near infrared regions was done by Dunkle and Bevans (1956), who used the Schuster's two-stream approximation. Giddings and LaChapelle (1961) calculated snow albedo using a diffusion model. These two models were actually equivalent and valid only for diffuse incidence and high albedo (Warren, 1982). They did not start from the single scattering by each snow grain. In the 1970's, many multiple scattering models for snow albedo considering the single scattering by each snow grain have appeared (Barkstrom, 1972; Bohren and Barkstrom, 1974; Barkstrom and Querfeld, 1975; Berger, 1979; Choudhury and Chang, 1979a,b). Bergen (1970, 1971) calculated the transmittance of snow layer with radiative transfer. However, these models were not accurate enough for the wide range of wavelength, grain size and solar zenith angle. Wiscombe and Warren (1980a) and Warren and Wiscombe (1980) simulated the spectral albedo of snow by the delta-Eddington approximation for multiple scattering, and the Mie theory for single scattering based on realistic physical parameters. They studied the dependence of spectral albedo on solar zenith angle, snow grain size, illuminating conditions and snow impurities, and compared with observations. They also discussed the effect of close packing and nonsphericity of each snow grain. Choudhury and Chang (1981a,b) and Choudhury (1981) developed a two-stream model considering the effects of the atmospheric gaseous absorption and surface reflection.

Various snow studies in the field of dynamics, chemistry and optics were reviewed by Mellor (1977) and detailed optical properties were reviewed by Warren (1982). The latter made an excellent review of snow albedo models and observations. Li (1982) simulated the bi-directional reflection distribution function (BRDF) of snow with the Mie theory and doubling method. This was the first model for BRDF of snow. Chýlek *et al.* (1983) extended the model of Wiscombe and Warren (1980a) and calculated the albedo of soot-contaminated snow. Carroll (1982) and Wendler and Kelly (1988) calculated the effects of snow surface striations and sastrugi on snow albedo. Blanchet and List (1987) examined the effect of anthropogenic aerosols in Arctic haze and snow on the radiation budget, using the atmospheric radiative transfer model with an interactive snow layer based on the delta-Eddington approximation. Warren *et al.* (1990) extended their model for calculations of spectral albedo and emissivity of CO_2 in Martian polar caps. Aoki (1992) developed a multiple scattering model based on the Mie theory and "doubling and adding" method, applied to the Rayleigh atmosphere-snow system that includes realistic clouds. Aoki *et al.* (1993) simulated the surface albedo of two-layer snow with the same model. Grenfell *et al.* (1994) used a two-layer snow model extended from the Wiscombe and Warren (1980a) model and obtained a good agreement of snow albedo with observation under cloudy condition in Antarctica. However, some discrepancies remained at near infrared wavelengths under the clear sky. They quoted three possible reasons for these discrepancies; underestimation of snow grain size, inaccurate correction of the instrument, and a fault in the model. Aoki *et al.* (1998) found that for new snow the optically effective grain size is the order of branch size of dendrites, from the observed spectral albedo at Barrow, Alaska and theoretically calculated albedo with the model used in this study.

The Wiscombe and Warren (1980a) model has been used operationally since the 1980's (Chýlek *et al.*, 1983; Marshall and Warren, 1986). Since this model is based on the delta-Eddington approximation, it is not applicable for large solar zenith angles and cannot be extended to the radiance model. With regard to the atmospheric effects, Wiscombe and Warren (1980b) calculated the spectral albedo at the snow surface and TOA, and the spectrally integrated planetary albedos (the latter was shown in Warren (1982)) with the summer atmospheric condition of the Antarctic Plateau. They reported that the differences in albedo between the snow surface and TOA were due to the Rayleigh scattering and gaseous absorption, and varied with the solar zenith angle. Choudhury and Chang (1981a,b) and Choudhury (1981) calculated the spectral albedo taking account of atmospheric effects by parameterizing the effect of aerosols, cloud cover and atmospheric gases, but the radiative interaction between atmosphere and snow was not incorporated. Blanchet and List (1987) calculated the effect of aerosols on the radiation budget considering this interaction and the atmospheric absorption, but they also used the delta-Eddington approximation.

It is necessary to investigate the atmospheric effects quantitatively with a more accurate multiple scattering model in the atmosphere-snow coupled system for the applications, such as remote sensing of snowpack properties, and the studies of aerosol and cloud radiative forcing over snow surface. It is also important to estimate the variability of snow albedo due to the atmospheric effects for experimental study of snow optical properties in which the observed albedos are compared with those calculated theoretically. The purpose of this study is to investigate the atmospheric effect on spectral and spectrally integrated snow albedos at the snow surface and TOA for the realistic atmospheres containing

absorptive gases, aerosols and cloud cover.

2. Radiative transfer model for the atmosphere-snow system

Basic behavior of the spectral surface albedo of snow has been clarified by many studies mentioned in the preceding section. The surface albedo of snow is essentially determined by a multiple scattering by snow grains, and the radiative interaction between snowpack and atmosphere. The albedo depends not only on the snow physical parameters but also on the external parameters, such as atmospheric conditions and solar zenith angle. The physical parameters can be placed in two groups: those related to single scattering (snow grain size, morphology and impurities), and those related to multiple scattering (snow depth, layer structure, density, water contents, surface condition and impurities). The external parameters contain the atmospheric condition (cloud cover, aerosols, air pressure and atmospheric gases) and solar zenith angle. The atmospheric effects on snow albedo examined in this study belong to the external parameters. The amounts of these effects, however, vary with the physical parameters such as snow grain size. It should be noticed that the effects of external parameters on snow albedo are related to the physical parameters.

In order to consider the radiative interaction between the atmosphere and snowpack (we will use the term "snow" to refer to "snowpack" hereafter), one snow layer is added below the atmospheric layers. The natural snow grains are nonspherical and packed close together. Wiscombe and Warren (1980) discussed these points and noted that a possible adjustment for near-field effects and nonsphericity of snow grains, are judged to produce a few percent reduction of albedo for all wavelengths. In our model, snow grains are assumed to be mutually independent spherical ice particles, and radiative transfer in snow is treated as in the multiple scattering model in the atmosphere containing aerosols or cloud particles. Table 1 shows the processes and parameters used in our radiative transfer model for the atmosphere-snow system. We used the Mie theory for single scattering and the "doubling and adding" method for multiple scattering without polarization. Accuracy of snow albedo at large solar zenith angles is improved by using the "doubling and adding" method compared with the delta-Eddington approximation. Snow grain is so large that the Mie phase function has a very sharp forward peak. This induces a large error in direct calculation of multiple scattering. Aoki *et al.* (1997) examined four kinds of approximations for phase function: Hansen's renormalization (Hansen, 1971); Grant's renormalization (Wiscombe, 1976); delta-M method (Wiscombe, 1977); and truncation method (Hansen, 1969; Potter, 1970). Aoki *et al.* (1997) found that the operationally useful methods were the Grant's renormalization and truncation method for the phase function of snow particles. In the latter method, the result is not sensitive to the choice of the truncation angle between 5° and 20°. In this study, thus, we use the truncation method for the snow phase function with the truncation angle of 10° and the delta-M method for cloud and aerosol phase functions.

The atmospheric transmittance of gaseous absorption is calculated for H_2O, CO_2, O_2 and O_3. For the first three gases, we used the extended exponential-sum fitting of transmissions (ESFT) developed by Asano and Uchiyama (1987) with the spectral absorption coefficients calculated with the line-by-line algorithm developed by Uchiyama (1992). In ESFT, the number of weight in a sum of exponentials to calculate the transmission function (N) in Eq. (1) of Asano and Uchiyama (1987)) is 10 for each gas. For the atmosphere, three kinds of model atmospheres (Anderson *et al.*, 1986) are used. They are midlatitude winter (MW), subarctic winter (SW), and SW that does not include the lower layer less than 2 km. The last one is adopted to simulate the atmosphere over the Antarctic Plateau and in this study we call it as Antarctic summer (AS). The atmospheric effects on the surface albedo of snow are mainly examined for MW, because the column amounts of air and absorptive gases are richest and the largest atmospheric effects is expected. The precipitable water in MW, SW and AS is 0.86 g/cm^2, 0.42 g/cm^2 and 0.19 g/cm^2, respectively. The effects of aerosols and cloud cover are only examined for SW, because we intend to simulate the Antarctic summer coastal aerosols and high latitudinal middle clouds, respectively.

The radiative transfer and albedo calculations are made at 54 wavelengths (λ) in the range from 0.3 to 3.0 μm with the spectral resolution (bandwidth) of 0.05 μm. Although the wavelength region 0.3–3.0 μm covered in this model seems somewhat narrow for the calculation of the shortwave radiation budget, it is sufficient for the study of the atmospheric effects on snow albedo, because the snow surface albedo at $\lambda > 3.0$ μm is almost zero and the solar energy that reaches to the surface in $\lambda < 0.3$ μm and $\lambda > 3.0$ μm is negligible. In calculating the spectrally integrated albedo and radiant flux, we used the data of extraterrestrial solar radiation compiled by Thekaekara (1974). According to this data, solar energy contained in the wavelength region of the present study is about 96.6 % at TOA. In the "doubling and adding" method, numerical integration over the scattering angle to calculate the radiant flux is conducted using a Gaussian quadrature of 16 points from 0° to 90° in zenith angle (32 streams), shown in Table 1, and thus albedo is only calculated for these 16 values of solar zenith angles

Table 1. Processes or parameters in radiative transfer model for the atmosphere-snow system.

Process or parameter	Method, value and references
Single scattering	Mie theory
Approximation for snow phase function	Truncation method with the truncation angle of 10° (Hansen, 1969; Potter, 1970)
Approximation for aerosol and cloud phase functions	Delta-M method (Wiscombe, 1977)
Multiple scattering	Doubling and adding method
Polarization	No
Atmospheric gaseous absorption	Exponential-sum fitting of transmissions with $N = 10$ (Asano and Uchiyama, 1987)
Atmospheric absorptive gases	H_2O, CO_2, O_2 and O_3
Model atmospheres	Midlatitude Winter (MW), Subarctic Winter (SW) and Antarctic Summer (AS = SW > 2 km), (Anderson *et al.*, 1986)
Atmospheric layers	Plane parallel, 13 layers for MW and SW, 11 layers for AS
Wavelengths (λ)	0.3–3.0 μm, 54 wavelengths
Wavelength resolution ($\Delta\lambda$)	0.05 μm
Extraterrestrial solar radiation	Thekaekara (1974)
Zenith angle resolution	16 points from 0° to 90° (= 32 streams)
Solar zenith angles (θ_0)	89.7°, 88.4°, 86.1°, 83.0°, 79.0°, 74.3°, 68.9°, 63.1°, 56.8°, 50.1°, 43.2°, 36.0°, 28.6°, 21.1°, 13.5°, 5.9°
Snow size distribution	Gamma-type size distribution, $v_{eff} = 0.125$ (Hansen,1971)
Effective radius of snow grain (r_{eff})	50, 200 and 1000 μm
Snow optical depth (τ_s)	Semi-infinite (= 3200 at $\lambda = 0.5$ μm)
Refractive index of ice	Warren (1984)
Aerosol type	75 % sulfuric acid particles (SA) in troposphere and volcanic ash (VA) in stratosphere
Single scattering coalbedo at $\lambda = 0.5$ μm	8.81×10^{-8} for SA and 4.80×10^{-2} for VA
Size distribution of aerosols	Log-normal for both aerosol types, $v_{eff} = 0.25$ for SA and $v_{eff} = 0.15$ for VA
Effective radius of aerosol particles	0.1 μm for SA and 0.32 μm for VA
Optical depth of aerosols (τ_a)	0.02 (SA), 0.1 (SA+VA) and 0.3 (SA+VA) at $\lambda = 0.5$ μm
Refractive indices of SA and VA	AFGL (1985)
Cloud size distribution	Deirmendjian's cloud model (Deirmendjian, 1964), $v_{eff} = 0.11$
Cloud type	Spherical water droplet
Effective radius of cloud droplets	5 μm
Optical depth of cloud cover (τ_c)	2.5, 5 and 10 at $\lambda = 0.5$ μm
Refractive index of water	Hale and Querry (1973) for $\lambda < 0.7$ μm, Palmer and Williams (1974) for 0.7 μm $\leq \lambda < 2.0$ μm, Downing and Williams (1975) for $\lambda \geq 2.0$ μm

(θ_0). Since we use plane parallel layers of the atmosphere and snow, the error in air mass calculation increases for large θ_0. Kneizys *et al.* (1983) showed that the deviation of secant (*i.e.*, air mass of plane parallel atmosphere) from the spherical and refractive atmosphere, is within 1 % for $\theta_0 \leq 72°$, and this error is kept up to $\theta_0 = 82°$ for H_2O but only up to $\theta_0 = 60°$ for O_3. The error is due mainly to the effect of the earth's curvature, and not atmospheric refraction. As a result, we just discuss the results for $\theta_0 \leq 79.0°$ in this study and show the results at $\theta_0 = 83.0°$ and 86.1° for reference.

We calculate the spectral surface albedo (α^s) and the spectral planetary albedo (α^p) of snow for three values of effective grain radii, $r_{eff} = 50$, 200 and 1000 μm, following the gamma-type size distribution with effective variance $v_{eff} = 0.125$ as defined by Hansen (1971). According to Wiscombe and Warren (1980a), these three radii correspond to new snow, fine-grained older snow and old snow for the melting point. The snow layer is homogeneous with the optical depth $\tau_s = 3200$ at $\lambda = 0.5$ μm for all r_{eff} being large enough (semi-infinite) for the calculation of surface albedo to converge at a constant value. For

the complex refractive index of ice, the data compiled by Warren (1984) is used.

The effect of atmospheric aerosols is examined for three values of optical depths, τ_a = 0.02, 0.1 and 0.3, at λ = 0.5 μm in SW. The aerosol layer with τ_a = 0.02 is the background level in the Antarctic coast in summer (Shaw, 1982; JMA, 1995) consisting of sulfuric acid (Shaw, 1982; Ito, 1989). The background aerosols are distributed in the troposphere below the height of 5 km for any case of τ_a and follow a log-normal size distribution with the effective radius of 0.1 μm (mode radius of 0.057 μm). The aerosols with τ_a = 0.1 and 0.3 consist of volcanic ash + background aerosols mentioned above. The volcanic ash aerosols are distributed in the stratosphere above the height of 10 km and follow a log-normal size distribution with the effective radius of 0.32 μm (mode radius of 0.23 μm) (Herber *et al.*, 1996). High values of τ_a were observed in the Antarctic coastal stations after major volcanic eruptions: τ_a = 0.1 for El Chichon in 1984 (Shiobara *et al.*, 1987); $\tau_a > 0.3$ for Cerro Hudson in 1991; and, τ_a = 0.2–0.3 for Mt. Pinatubo in 1992 (Kaneto *et al.*, 1994; Herber *et al.*, 1996). For complex refractive indices of sulfuric acid and volcanic ash, the data compiled by AFGL (1985) is used. In the study of cloud effect, we assumed the high latitudinal middle clouds (Ac and As), because the middle clouds are considered to have possible maximum effects on snow surface albedos in the clouds with frequent appearance in the polar region. Since the annual mean altostratus appears at 2–3 km height in the high latitude (Liou, 1992), the cloud layer is fixed at this height. The water vapor amount is assumed to be saturated in the cloud layer. This increases the precipitable water of SW by 8.5 percent. The effects of cloud cover are examined for three values of optical depths of spherical water clouds, τ_c = 2.5, 5, and 10, at λ = 0.5 μm based on the size distribution of Deirmendjian cloud model (Deirmendjian, 1964) with the effective radius 5 μm. The solar disk cannot be seen through the cloud cover for $\tau_c \geq 5$, when the sun is at zenith direction.

3. Spectral surface albedo

Main characteristics that we notice about the spectral surface albedo of snow under the clear sky are: (1) the contrast between visible and near infrared wavelengths, (2) the snow grain size (r_{eff}) dependence, and (3) the solar zenith angle (θ_0) dependence, as shown in Fig. 1. In Fig. 1a the spectral surface albedos are shown not only for the three r_{eff} discussed in Section 2 but also for the other four values of r_{eff}, to see more details of the dependence of surface albedo on snow grain size. It can be seen that the surface albedo is high in the visible region, and low in the near infrared region. This is due mainly to the fact that the imaginary part of the refractive index of ice is low (less absorptive) in the visible region, and high (much absorptive) in the near infrared region. The surface albedo decreases with the increase of r_{eff}. This is significant especially in the near infrared region. The reason is that the single scattering albedo of a large snow grain is lower than that of a small grain, and its difference is large in the near infrared region. The monochromatic surface albedo at large θ_0 is higher than that at small θ_0 for clear sky as shown in Fig. 1b. The θ_0 dependence of surface albedo for clear sky is related to the direct solar beam and asymmetric phase function of the snow grain. Warren (1982) explained as follows: A photon on average undergoes its first scattering event closer the surface if it entered the snow at a grazing angle. If the scattering event sends it in an upward direction, its chance of escaping the snow without being absorbed is greater than it would be if it were scattered from deeper in the snow. This would be observed even if the ice par-

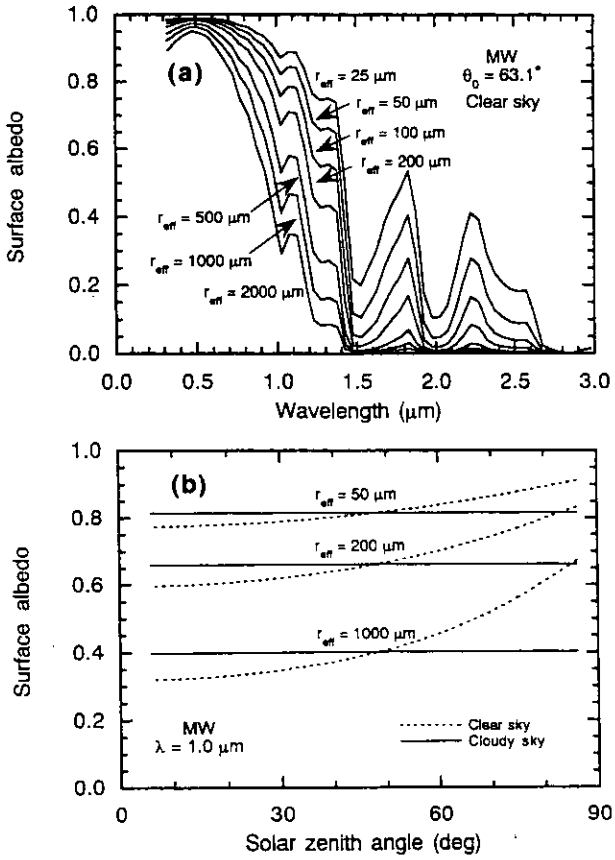

Fig. 1. (a) Spectral surface albedo of snow for various snow grain sizes r_{eff}, θ_0 = 63.1° under clear atmosphere of MW. (b) Solar zenith angle dependence of the monochromatic surface albedo of snow under clear atmosphere (dashed lines) and cloudy case (solid lines) of MW at λ = 1.0 μm for r_{eff} = 50, 200 and 1000 μm.

ticles scattered light equally in all directions. But the phenomenon is greatly enhanced by the extreme asymmetry of scattering function, whereby scattering within a few degrees of the forward direction is much more probable than scattering to other angles.

The snow surface is illuminated not only by the direct solar radiation but also the diffuse one. The θ_0 dependence of surface albedo is also related to these factors. In the case of no atmosphere the snow surface is illuminated only by the direct beam, and the albedo is higher for large θ_0 than that for small θ_0. However, it is modified by the diffuse component under the atmosphere. In the clear sky for small θ_0 the surface albedo is increased by the additional contribution of diffuse components from larger zenith angles, and vice versa for large θ_0. In the overcast case the direct solar beam is weakened or disappeared, and snow surface is illuminated mainly by diffuse radiation, and the surface albedo becomes constant — being independent of θ_0 as shown in the cloudy case of Fig. 1b. In Fig. 1b the value of θ_0 at which the cloudy sky albedo crosses the clear sky albedo is about 48°. Warren (1982) estimated this value as 50° from the albedo of snow surface illuminated by pure diffuse radiation. In the following subsections, we examine the effects of Rayleigh scattering, gaseous absorption, aerosols and cloud cover on the spectral surface albedo of snow via the theoretical calculations.

3.1 Effects of Rayleigh scattering and absorptive gases

Figure 2a shows the transmission function of gaseous absorption bands and Rayleigh scattering calculated by ESFT for direct solar radiation at the surface, where the values of $\theta_0 = 79.0°$ have been used to clearly show the weak absorption bands. The fractions of diffuse and direct components in the downward solar flux vary depending on the gaseous absorption and Rayleigh scattering. Figure 2b shows the fraction of the diffuse component in the downward solar flux. The reason that the fraction of diffuse component is generally high at the shorter wavelengths, is the dominance of Rayleigh scattering. In addition to this, the diffuse component increases significantly at large θ_0 in the strong gaseous absorption bands.

In order to examine the clear atmospheric effects on the spectral surface albedo of snow, calculations have been made for the atmosphere of MW containing Rayleigh scattering and absorption by H_2O, CO_2, O_2 and O_3 (we will denote this albedo by α^s_{4g}) and for no atmosphere (α^s_{na}). Figure 3 shows the difference between α^s_{4g} and α^s_{na} for three values of r_{eff}. The difference $|\alpha^s_{4g} - \alpha^s_{na}|$ is large in the region of strong Rayleigh scattering and strong gaseous absorption bands. In the region $\lambda < 0.5$ μm, the effects of Rayleigh scattering and O_3 absorption are

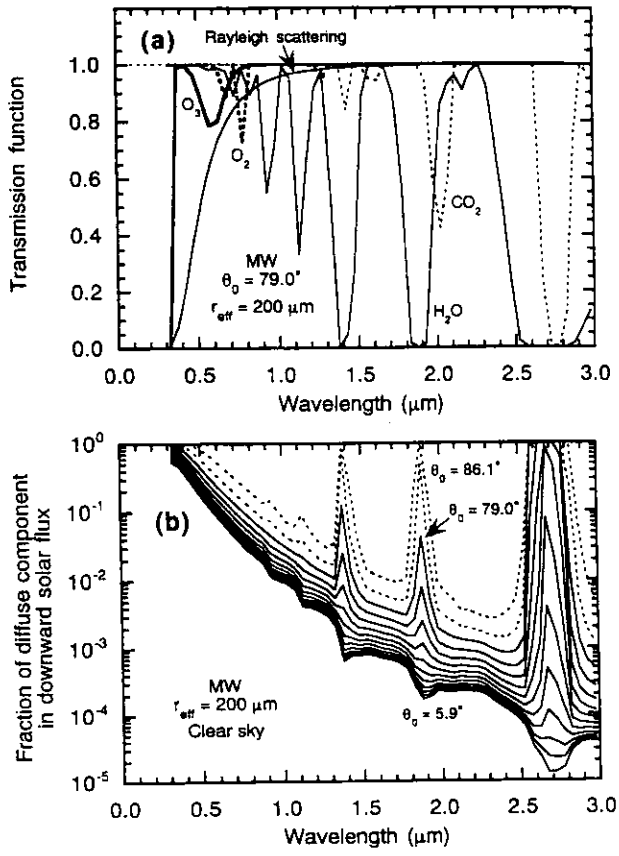

Fig. 2. (a) Spectral transmission function of the atmospheric absorption, and Rayleigh scattering at the surface for direct solar radiation of $\theta_0 = 79.0°$ and clear atmosphere of MW. (b) Spectral distribution of the fraction of diffuse component in the downward solar flux for clear atmosphere of MW on the snow surface with $r_{eff} = 200$ μm. They are shown for fourteen solar zenith angles from 5.9° to 86.1° shown in Table 1. The values for $5.9° \leq \theta_0 \leq 79.0°$ are indicated by solid lines, and $\theta_0 = 83.0°$ μm and 86.1° by dashed lines.

dominant, where it is found $\alpha^s_{4g} < \alpha^s_{na}$ at large θ_0 and $\alpha^s_{4g} > \alpha^s_{na}$ at small θ_0. In this wavelength region, the fraction of diffuse component in the downward solar flux is large even at small θ_0 due to the Rayleigh scattering. This makes the θ_0 dependence of surface albedo faint (Fig. 4a). We also see large values of $|\alpha^s_{4g} - \alpha^s_{na}|$ for large r_{eff} in the same region. This is because the θ_0 dependence of α^s_{na} is significant for large r_{eff}.

Figure 3 also shows that there are large difference $|\alpha^s_{4g} - \alpha^s_{na}|$ in the three wavelength regions of strong gaseous absorption at large θ_0. For example, the difference $|\alpha^s_{4g} - \alpha^s_{na}|$ increases significantly for $\theta_0 > 79°$ at $\lambda = 1.375$ μm (Fig. 4b). In the absorption bands the fraction of the diffuse component in downward solar flux becomes larger at large θ_0 (see

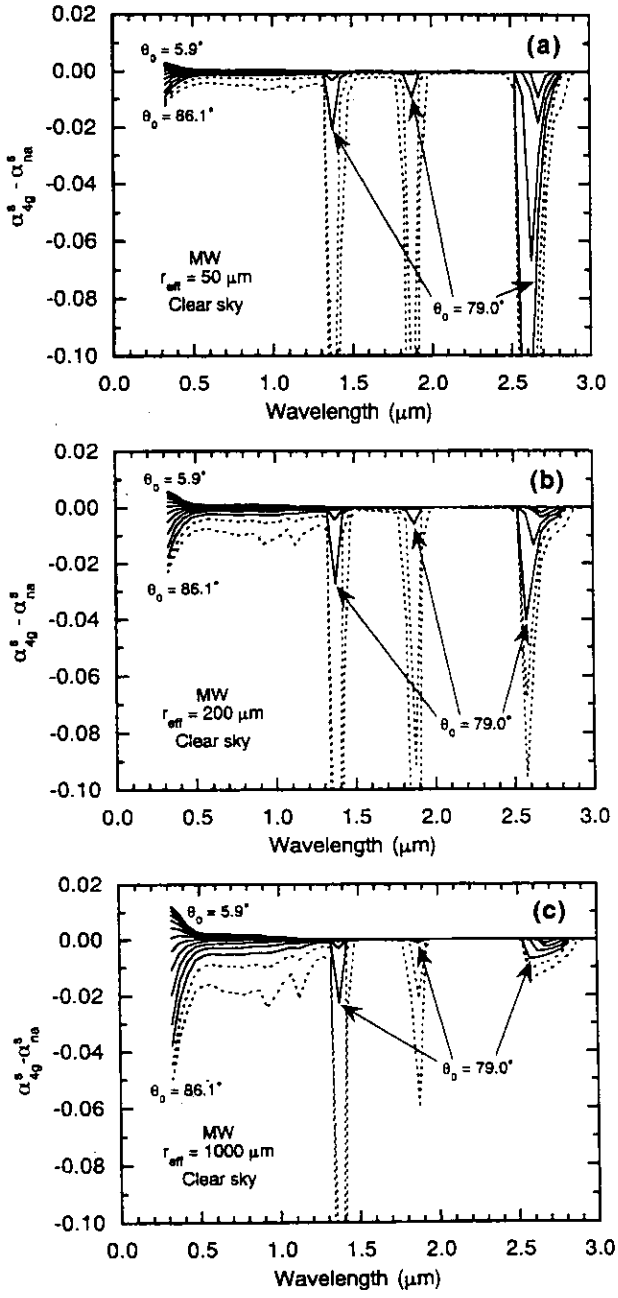

Fig. 3. Difference between the spectral surface albedo of snow for clear atmosphere of MW containing H_2O, CO_2, O_2 and O_3 (α^s_{4g}) and that for no atmosphere (α^s_{na}) for (a) $r_{eff} = 50$ μm, (b) $r_{eff} = 200$ μm and (c) $r_{eff} = 1000$ μm. The definitions of the solid line and dashed line are the same as Fig. 2.

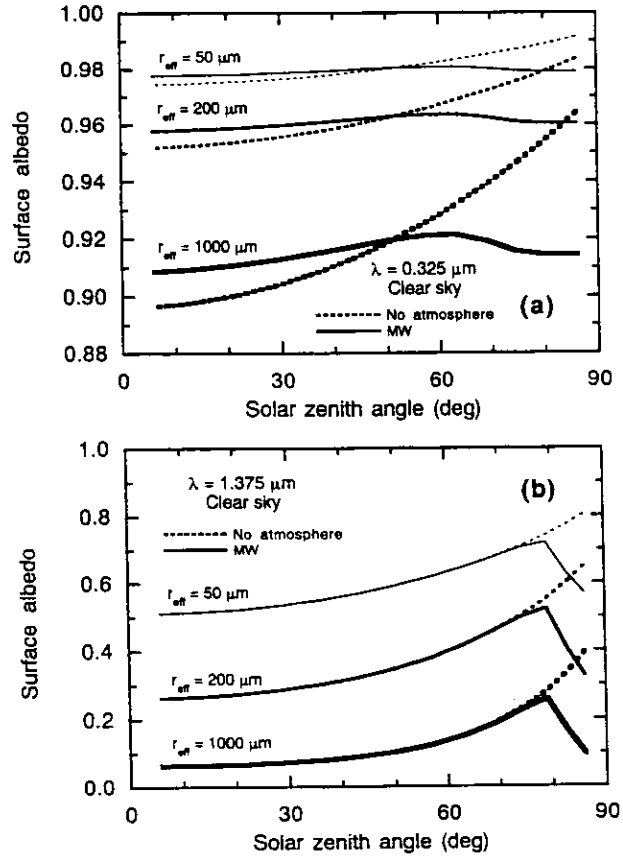

Fig. 4. Solar zenith angle dependence of the monochromatic surface albedo of snow with three values of r_{eff} for clear atmosphere of MW (solid line) and that for no atmosphere (dashed line) at (a) $\lambda = 0.325$ μm and (b) $\lambda = 1.375$ μm.

Fig. 2b) since the direct solar beam suffers strong absorption along the long path compared with diffuse radiation. This reduces the value of α^s_{4g} small. On the contrary, at small θ_0 the diffuse fraction rather becomes small and makes α^s_{4g} close to α^s_{na}. Thus, the value of α^s_{4g} is lower than that of α^s_{na} only at large θ_0 in the gaseous absorption bands.

Since the calculation of radiative transfer is time consuming, it is worth noting the possibility to omit the absorptive gases and Rayleigh scattering in calculating the spectral surface albedo. Restricting our discussion to the average transmittance for $\Delta\lambda = 0.05$ μm, the absorption by the atmospheric gases can be omitted for all r_{eff} for the atmosphere of MW for $\theta_0 \leq 63.1°$ within the error of 0.01. However, it should be remembered that this conclusion could be changed for different value of $\Delta\lambda$, since average transmittance varies greatly with band width.

3.2 Effects of aerosols and cloud cover

The fractions of diffuse component in downward solar flux are shown in Fig. 5a for the atmosphere containing aerosols and Fig. 5b for cloudy sky. It can be seen that aerosols and cloud cover increase the diffuse component in downward solar flux by comparing these figures with Fig. 2, where the diffuse component is shown for the clear sky of MW (basic behavior is same for SW). These figures will help to understand the behavior of the spectral surface albedo with aerosols or clouds shown in the following. Figure 6a shows the monochromatic surface albedos as a function of θ_0 for the atmosphere con-

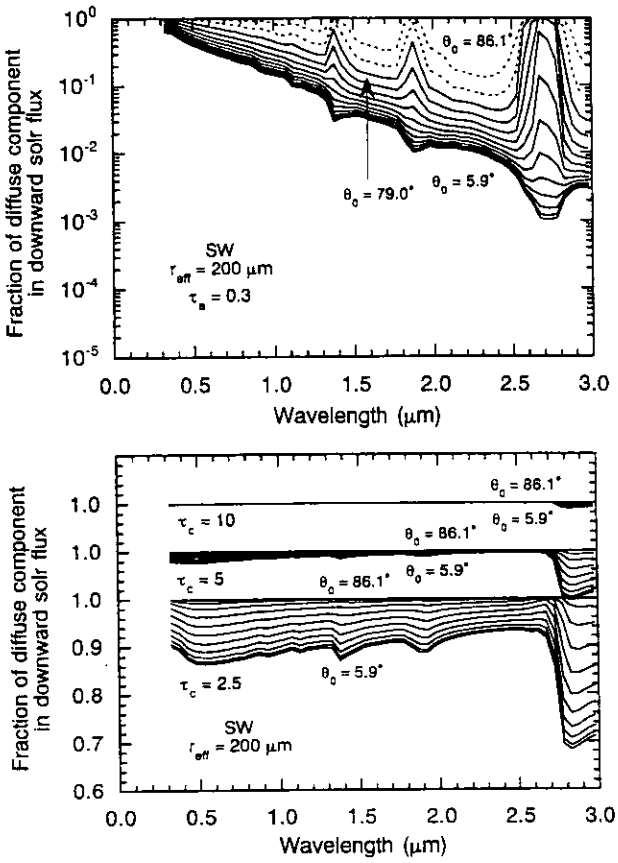

Fig. 5. (a) Same as Fig. 2b, but for the atmosphere of SW containing aerosols with $\tau_a = 0.3$. (b) Same as Fig. 2b, but for the cloudy atmosphere of SW with three kinds of τ_c. Curves are successively displaced upward by 0.1 except for $\tau_c = 2.5$.

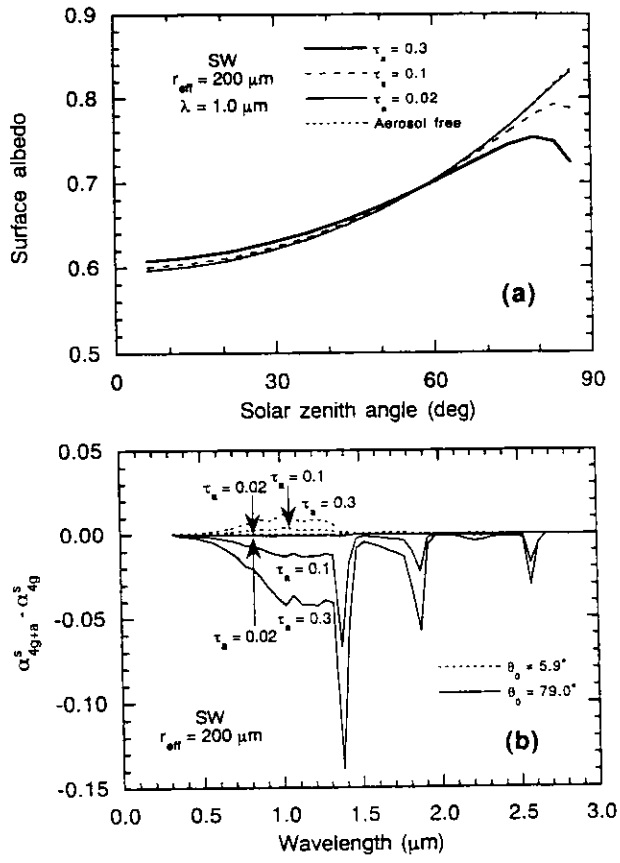

Fig. 6. (a) Monochromatic surface albedo of snow with $r_{eff} = 200$ μm as a function of θ_0 for the atmosphere of SW containing aerosols (α^s_{4g+a}) with three kinds of τ_a and aerosol free case (α^s_{4g}) at $\lambda = 1.0$ μm. (b) Difference between α^s_{4g+a} and α^s_{4g} as a function of wavelength at $\theta_0 = 5.9°$ (dashed line) and 79.0° (solid line).

taining aerosols (α^s_{4g+a}), and for the aerosol free case (α^s_{4g}). The θ_0 dependence of α^s_{4g+a} becomes weak with the increase of the optical depth of aerosols τ_a. The difference between α^s_{4g+a} and α^s_{4g} is larger for large θ_0 than that for small θ_0. Since the θ_0 dependence of each albedo varies with the wavelength, the difference between α^s_{4g+a} and α^s_{4g} also depends on the wavelength. Figure 6b shows $\alpha^s_{4g+a} - \alpha^s_{4g}$ as a function of wavelength at $\theta_0 = 5.9°$ and 79.0°. The effect of background aerosols ($\tau_a = 0.02$) on the surface albedo is very small. However, the difference $|\alpha^s_{4g+a} - \alpha^s_{4g}|$ rises up to 0.14 in the absorption band ($\lambda = 1.375$ μm) for $\tau_a = 0.3$ and $\theta_0 = 79.0°$. This is because the aerosols increase the fraction of diffuse component at large θ_0 in the absorption band as shown in Fig. 5a. At small θ_0 the diffuse component is rather reduced in the absorption bands compared with the non-absorbing region and results in very small values of $|\alpha^s_{4g+a} - \alpha^s_{4g}|$.

Figure 7a shows the monochromatic surface albedos of snow as a function of θ_0 for the cloudy atmosphere (α^s_{4g+c}) and clear case (α^s_{4g}). The θ_0 dependence of α^s_{4g+c} is completely lost for $\tau_c = 10$, where snow surface is illuminated only by diffuse radiation (see Fig. 5b). Figure 7b shows the spectral variation of $\alpha^s_{4g+c} - \alpha^s_{4g}$ at $\theta_0 = 5.9°$ and 79.0°. The value of $|\alpha^s_{4g+c} - \alpha^s_{4g}|$ is small around $\lambda = 0.5$, 1.5, 2.0 and 2.8 μm, where α^s_{4g} is close to unity or zero (see Fig. 1a). When the value of α^s_{4g} is close to unity, the light absorption by ice is so weak that a large part of the incident photons would escape from the snow surface almost independent of the incident angle. In the case of α^s_{4g} close to zero, the light absorption by ice is so strong that a large part of the incident photons would be absorbed in snow, almost independent of incident angle. Thus, the θ_0 dependence of surface albedo is small for clear sky in such wavelength regions, and the value of $|\alpha^s_{4g+c} - \alpha^s_{4g}|$ becomes small. Except for such wavelength regions, it can be seen that the effect of cloud cover on spectral surface albedo is quite large even for $\tau_c = 2.5$ at any value of θ_0. This is because the fraction of

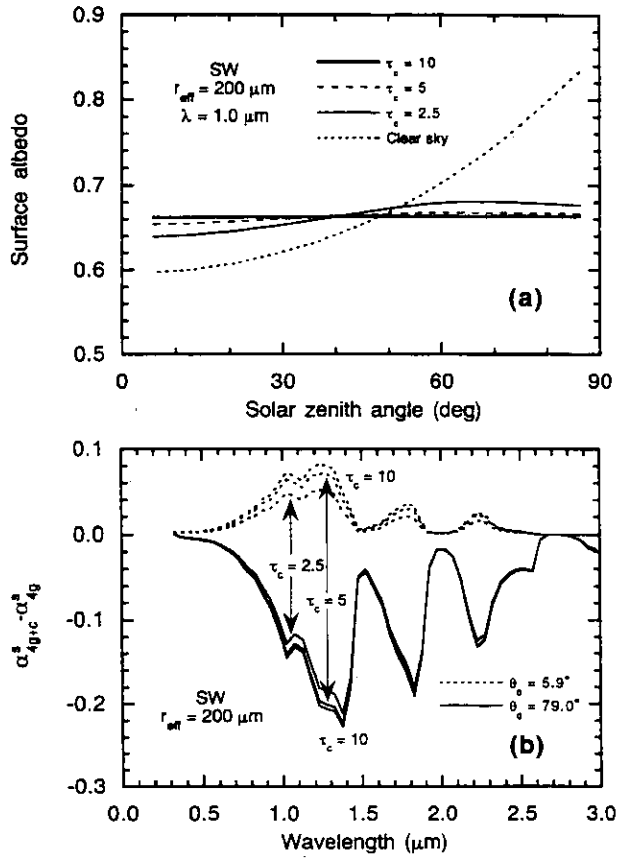

Fig. 7. (a) Same as Fig. 6a, but for the cloudy atmosphere of SW (α^s_{4g+c}) with three kinds of τ_c and clear case (α^s_{4g}). (b) Same as Fig. 6b, but for the cloudy atmosphere ($\alpha^s_{4g+c} - \alpha^s_{4g}$).

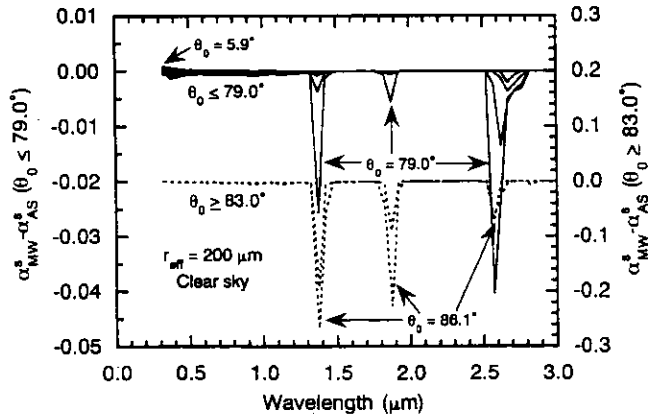

Fig. 8. Difference in the spectral surface albedo of snow with $r_{eff} = 200$ μm under the clear atmosphere between MW (α^s_{MW}) and AS (α^s_{AS}). The values for $5.9° \le \theta_0 \le 79.0°$ are indicated by solid lines on the left ordinate, and $\theta_0 = 83.0°$ and 86.1° by dashed lines on the right ordinate.

diffuse component is large enough at any value of θ_0 in the cloudy condition due to the large optical depth as shown in Fig. 5b.

3.3 Effect of difference in atmospheric type

We have seen the effects of clear atmosphere on surface albedo for MW in subsection 3.1. The atmosphere, however, varies with place and time. In this subsection we examine the dependence of surface albedo on the atmospheric type. In three model atmospheres — MW, SW and AS — the column amounts of air and H_2O, are largest for MW, less for SW and smallest for AS. For SW and MW, the column amounts of gases, except H_2O, are almost the same. Hence, the atmospheric effect is generally largest for MW and smallest for AS. We calculated the difference in spectral surface albedos between MW (α^s_{MW}) and AS (α^s_{AS}) to examine the maximum effect of difference in the atmospheric type on the surface albedo.

Figure 8 shows the spectral variation of $\alpha^s_{MW} - \alpha^s_{AS}$. The value of α^s_{MW} is lower than that of α^s_{AS} in the gaseous (H_2O) absorption bands due to the reason shown in Subsection 3.1 for the case of $\alpha^s_{4g} - \alpha^s_{na}$.

At large θ_0 in the H_2O bands the fraction of diffuse component increases with H_2O amount. As a result the spectral surface albedo for H_2O rich atmosphere (α^s_{MW}) is lower than that for H_2O poor atmosphere (α^s_{AS}) at large θ_0 only in the H_2O absorption bands. The calculations were also done for snow with $r_{eff} = 50$ and 1000 μm and these results showed that the effect of difference in the atmospheric type on the surface albedo is very small at $\theta_0 \le 63.1°$, and α^s_{MW} agrees with α^s_{AS} within 0.01. For $\theta_0 > 63.1°$, this effect gradually increases with θ_0 only in the H_2O absorption bands.

4. Spectral planetary albedo

4.1 Effect of the difference in atmospheric type

The effects of the gaseous absorption and Rayleigh scattering are too large to be neglected for the spectral planetary albedo. Wiscombe and Warren (1980b) calculated them over the snow surface in the Antarctic Plateau using the atmospheric radiative transfer model coupled with the snow albedo model of Wiscombe and Warren (1980a). They examined the atmospheric effects on the planetary albedo for the atmospheres in January and October, and pointed out that the planetary albedo is very slightly higher than the surface albedo only in the region $0.35 \le \lambda \le 0.43$ μm, due to the Rayleigh scattering. The reduction of the planetary albedo in the O_3 and H_2O absorption bands is more pronounced for October (large θ_0 and long slant path) than for January (midsummer).

We calculated the spectral planetary albedo (α^p_{4g}) over the snow for three kinds of model atmospheres (Fig. 9). It is easy to understand the atmospheric effects on α^p_{4g} by comparing these results with the

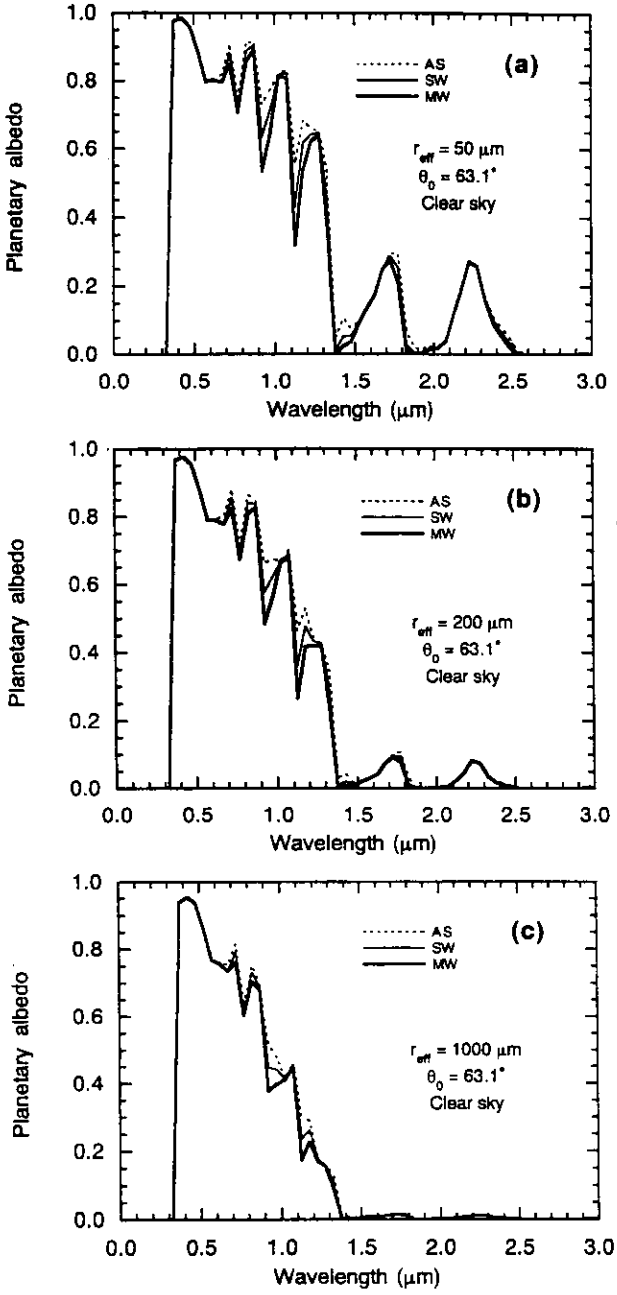

Fig. 9. Spectral planetary albedo for the atmosphere of MW, SW and AS at $\theta_0 = 63.1°$ over the snow with (a) $r_{eff} = 50$ μm, (b) $r_{eff} = 200$ μm and (c) $r_{eff} = 1000$ μm.

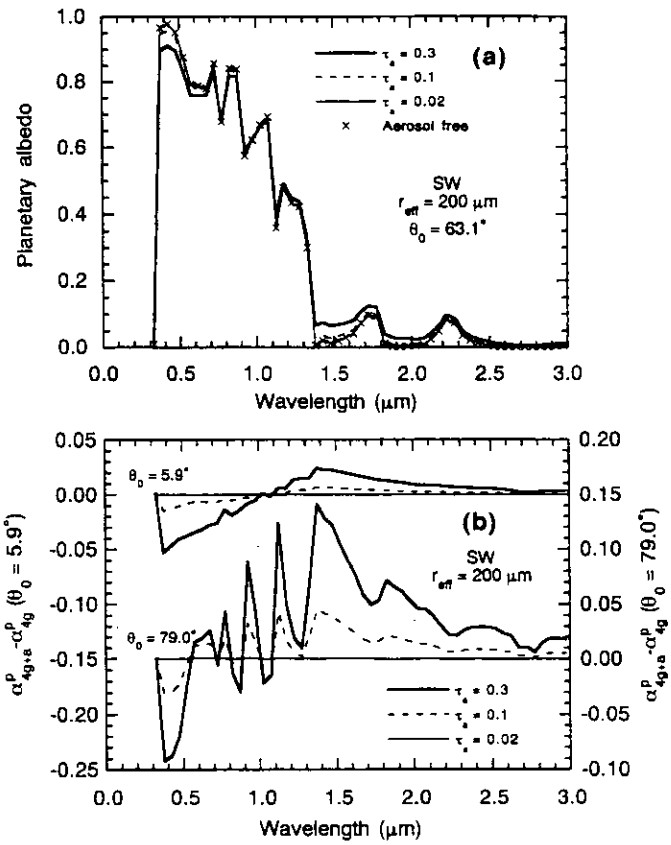

Fig. 10. (a) Spectral planetary albedos for the atmosphere of SW containing aerosols (α^p_{4g+a}) with three kinds of τ_a and aerosol free case (α^p_{4g}) at $\theta_0 = 63.1°$ over the snow with $r_{eff} = 200$ μm. (b) Difference between α^p_{4g+a} and α^p_{4g} as a function of wavelength at $\theta_0 = 5.9°$ (left ordinate) and 79.0° (right ordinate).

spectral surface albedo (α^s_{4g}) shown in Fig. 1a. The gaseous constituent that reduces the planetary albedo in ultraviolet and visible regions is O_3. The degrees of these reductions are almost independent of the model atmospheres because amounts of O_3 are roughly same in three model atmospheres studied here. The value of α^p_{4g} around $\lambda = 0.4$ μm is slightly higher than that of α^s_{4g} due to the Rayleigh scattering as noted by Wiscombe and Warren (1980b). In the near infrared region, the differences between model atmospheres become significant in the H_2O absorption bands, where the spectral planetary albedo for MW (α^p_{MW}) is lower than that for AS (α^p_{AS}). The reduction of planetary albedo by gaseous absorption is large for small r_{eff}. This is because the value of α^s_{4g} for snow with small r_{eff} is higher than those with larger r_{eff}. As an example, since the value of α^s_{4g} for $r_{eff} = 1000$ μm is originally close to zero at $\lambda > 1.5$ μm as shown in Fig. 1a, the apparent influence by gaseous absorption is very small. However, since the value of α^s_{4g} for $r_{eff} = 50$ μm is in the range 0.05–0.4 for $1.5 < \lambda < 2.6$ μm, it can be reduced by a significant amount due to gaseous absorption.

4.2 Effects of aerosols

The effect of aerosols on the planetary albedo varies with the geometric condition such as θ_0, and the properties of aerosols such as absorptivity, particle size and vertical profile. In this study, we assumed the sulfuric acid aerosols in the troposphere

were the background aerosols and the volcanic ash aerosols were in the stratosphere. Figure 10a shows the spectral planetary albedo for the atmosphere containing aerosols (α^p_{4g+a}), and the aerosol free case (α^p_{4g}). There is no significant change in the planetary albedo caused by the background aerosols, but the volcanic ash reduces the planetary albedo in the shorter wavelength region, and increases it in the longer wavelength region. To see the details of the effect of aerosols, the differences between α^p_{4g+a} and α^p_{4g} are calculated for $\theta_0 = 5.9°$ and 79.0° (Fig. 10b). The effect of aerosols is very small for $\tau_a = 0.02$ at both values of $\theta_0 = 5.9$ and 79.0°. In the case of $\tau_a \geq 0.1$, the value of α^p_{4g+a} is higher than that of α^p_{4g} in the longer wavelength region. In the region $\lambda > 1.4$ μm the single scattering albedo of volcanic ash particle is higher than that of snow grain. This is the reason for $\alpha^p_{4g+a} > \alpha^p_{4g}$ for $\lambda > 1.4$ μm. In the region $\lambda \leq 1.4$ μm, if there is no absorption by the atmospheric gases, it would be $\alpha^p_{4g+a} < \alpha^p_{4g}$ due to the difference in single scattering albedo between the volcanic ash and snow grain. Therefore, in the wavelength region with weak absorption or without absorption, the value of α^p_{4g+a} is lower than that of α^p_{4g}. In the wavelength regions with gaseous absorption (including the weak absorption bands for $\theta_0 = 79.0°$, because the atmospheric absorption is intensified along the long slant path), the planetary albedo is reduced by the atmospheric absorption for the aerosol free case. Since the volcanic ash distributes above most of the absorptive gases, the direct solar beam is scattered upward by the volcanic ash before suffering the atmospheric absorption. This is the reason of $\alpha^p_{4g+a} > \alpha^p_{4g}$ in the wavelength regions with gaseous absorption of $\lambda \leq 1.4$ μm. Thus, the spectral distribution of the effect of aerosols on the planetary albedo varies according to θ_0.

4.3 Effect of cloud cover

Figure 11a shows the spectral planetary albedo for the cloudy atmosphere (α^p_{4g+c}) and for the clear case (α^p_{4g}), where the cloud cover basically increases the planetary albedo, especially in the near infrared region. This is because a cloud droplet is smaller than a snow grain, and the single scattering albedo of a cloud droplet is higher than that of a snow grain. Valovcin (1978) noted that reflectance in the region $1.4 < \lambda < 1.8$ μm can be used in discriminating clouds from snow by aircraft observation. This method uses the difference in albedo between cloud cover and snow surface. An example of the θ_0 dependence of the monochromatic planetary albedo for the cloudy atmosphere is shown in Fig. 11b. The cloud cover increases the planetary albedo throughout the range of θ_0. However, it should be noted that although it is not shown here, this situation could be reversed in some cases. For example, the value of

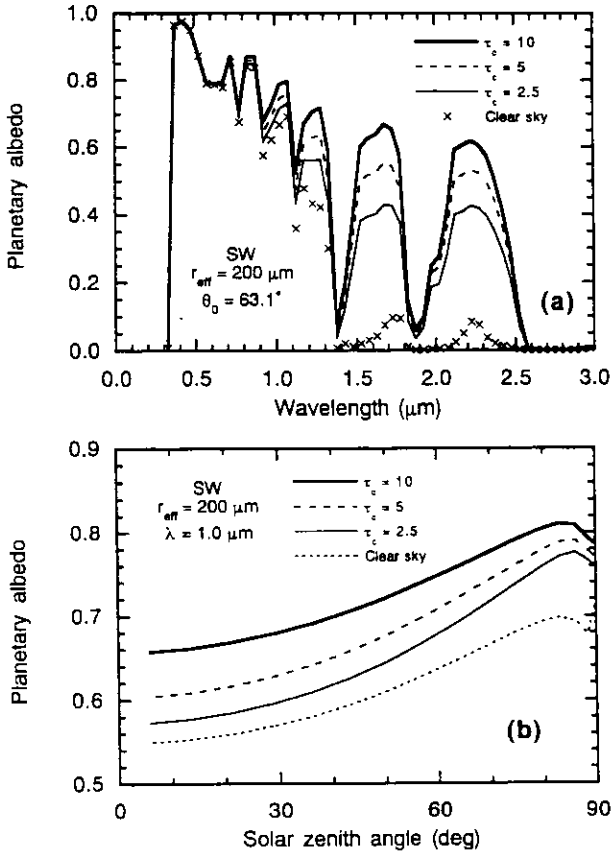

Fig. 11. (a) Same as Fig. 10a, but for the cloudy atmosphere of SW (α^p_{4g+a}) with three kinds of τ_c and clear case (α^p_{4g}). (b) Monochromatic planetary albedo as a function of θ_0 for the cloudy atmosphere and clear case at $\lambda = 1.0$ μm over the snow with $r_{eff} = 200$ μm.

α^p_{4g+c} is slightly lower than that of α^p_{4g} for $\theta_0 = 5.9°$, $0.5 < \lambda < 0.8$ μm, $\tau_c = 2.5$ and $r_{eff} = 200$ μm. This is because the multiple scattering by the cloud droplets increases the effective path length of diffuse radiation and thus increases the gaseous absorption.

5. Spectrally integrated surface and planetary albedos

5.1 Effect of the difference in atmospheric type

The "surface albedo" observed with a pyranometer is the spectrally integrated surface albedo ($\overline{\alpha}^s$). Its θ_0 dependence has been investigated in many observational studies (*e.g.*, Carroll and Fitch, 1981; Yamanouchi, 1983) and theoretical studies (Wiscombe and Warren, 1980a, Choudhury and Chang, 1981a). The argument whether surface specular reflection should be considered for the study of θ_0 dependence of the spectral surface albedo has been made between Warren and Wiscombe (1981) and Choudhury (1981). This controversy arises from the problem that the θ_0 dependence of observed albedo did not agree with the result of theoretical

calculation made on the assumption of spherical ice particles for snow grains. Warren (1982) argued that the reasons for the confusion are: (1) modeling error, (2) instrument error, (3) inadequate observation of snow grain size, impurity content, and surface roughness — all of which should affect the slope of surface albedo — and, (4) inadequate knowledge of the spectral distribution of the incident radiation. Yamanouchi (1983) compared the observation at Mizuho Station in Antarctica with the theoretical model of Wiscombe and Warren (1980a) without surface reflection, and found that the theoretical model can explain the measured snow albedo for a renewed snow surface with fine-grained rounded particles. However, the model cannot explain the snow albedo when the surface grains become more faced as mentioned by Choudhury (1981) or when sintering of particles occurred and surface specular reflection comes more pronounced. All of these effects have to be considered when observed surface albedos are compared with the theoretical calculations. In the followings, we would like to take a notice to another important factor, the atmospheric effect, that affects on $\overline{\alpha}^s$ of snow:

Figure 12a shows $\overline{\alpha}^s$ of snow as a function of θ_0 for three model atmospheres. It has been shown in Subsection 3.3 that the effect of difference in atmospheric type on the spectral surface albedo is very small ($|\alpha^s_{MW} - \alpha^s_{AS}| < 0.01$) for $\theta_0 \leq 63.1°$ and α^s_{MW} is lower than α^s_{AS} only in gaseous absorption bands for $\theta_0 > 63.1°$. However, the value of $\overline{\alpha}^s$ varies depending on the model atmospheres and $\overline{\alpha}^s$ for MW ($\overline{\alpha}^s_{MW}$) is higher than that for AS ($\overline{\alpha}^s_{AS}$) at any θ_0. Namely, the cause of differences in $\overline{\alpha}^s$ between model atmospheres is not attributed to the differences in spectral surface albedo in the gaseous absorption bands.

The spectrally integrated surface albedo $\overline{\alpha}^s$ is given by

$$\overline{\alpha}^s = \frac{\int_0^\infty \alpha^s(\lambda) F^\downarrow(\lambda) d\lambda}{\int_0^\infty F^\downarrow(\lambda) d\lambda}, \tag{1}$$

where $F^\downarrow(\lambda)$ is the downward solar flux at snow surface, and $\alpha^s(\lambda)$ is the spectral surface albedo of snow. The value of $F^\downarrow(\lambda)$ varies depending on the atmospheric condition, especially on H_2O amount. The Eq. (1) means that $\overline{\alpha}^s$ is the weighted mean of $\alpha^s(\lambda)$ with the weight of normalized downward flux. Even if $\alpha^s(\lambda)$ does not change with the atmospheric condition, $\overline{\alpha}^s$ could change depending on the atmosphere through $F^\downarrow(\lambda)$. The major H_2O bands are located in the near infrared region. Hence, $F^\downarrow(\lambda)$ for MW (H_2O rich) is smaller than that for AS (H_2O poor) in the near infrared region, but both are almost the same in the visible region. On the other hand, $\alpha^s(\lambda)$ is high in the visible region and low in the near infrared region. Since the weight ($F^\downarrow(\lambda)$) for low value of $\alpha^s(\lambda)$ in the near infrared region is small for MW and large for AS, the value of $\overline{\alpha}^s_{MW}$ becomes higher than that of $\overline{\alpha}^s_{AS}$. The maximum difference between $\overline{\alpha}^s_{MW}$ and $\overline{\alpha}^s_{AS}$ amounts to 0.015 for $r_{eff} = 50$ μm and 0.021 for $r_{eff} = 1000$ μm at $\theta_0 = 5.9°$. Thus, several percent of spectrally integrated surface albedo could vary with the H_2O amount, even for the same spectral surface albedo.

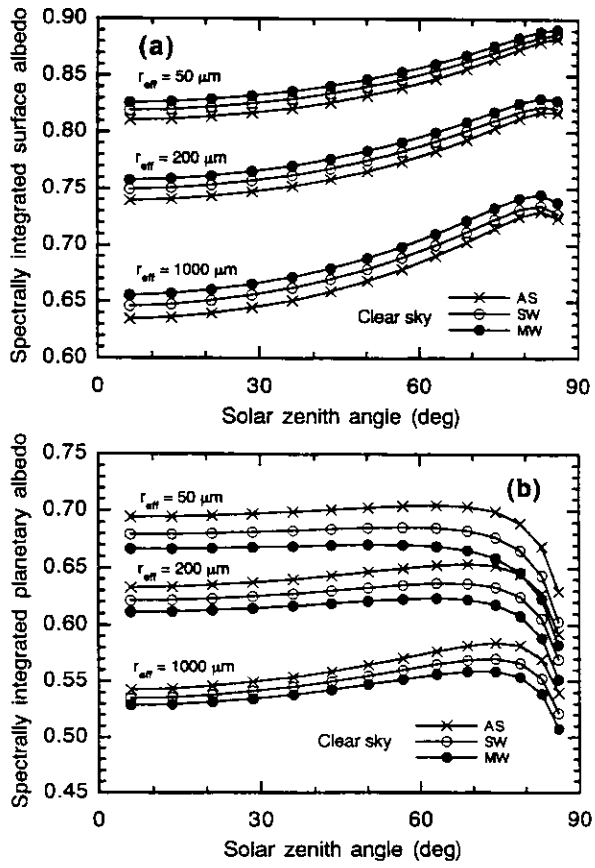

Fig. 12. Spectrally integrated albedos as a function of θ_0 at (a) snow surface ($\overline{\alpha}^s$) and (b) TOA ($\overline{\alpha}^p$) over the snow with $r_{eff} = 50$, 200 and 1000 μm for the clear atmospheres of MW, SW and AS.

Figure 12b shows the spectrally integrated planetary albedo ($\overline{\alpha}^p$) as a function of θ_0. In this case, $\overline{\alpha}^p$ has the same form as Eq. (1) with replacing $\alpha^s(\lambda)$ by $\alpha^p(\lambda)$ and $F^\downarrow(\lambda)$ by the downward solar flux at TOA. Since the downward solar flux at TOA does not depend on the atmospheric condition, the behavior of $\alpha^p(\lambda)$ would be directly reflected on $\overline{\alpha}^p$. Contrary to the case of $\overline{\alpha}^s$, the value of $\overline{\alpha}^p_{MW}$ is lower than that of $\overline{\alpha}^p_{AS}$. This is because $\alpha^p_{MW} < \alpha^p_{AS}$ mainly in the H_2O bands (see Fig. 9). The difference between $\overline{\alpha}^p_{MW}$ and $\overline{\alpha}^p_{AS}$ increases with θ_0, and amounts to 0.043 for $r_{eff} = 50$ μm and 0.028 for $r_{eff} = 1000$ μm at $\theta_0 = 79.0°$.

Although $\overline{\alpha}^s$ gradually increases with θ_0, $\overline{\alpha}^p$ rapidly decreases at around $\theta_0 = 75°$. The former reflects the property of θ_0 dependence of $\alpha^s(\lambda)$. The reason of the latter phenomenon is that the absolute

values of the downward solar flux on the snow surface is reduced by the strong absorption of the direct solar beam propagating along the long slant path at large θ_0 and the resultant upward solar flux at TOA is also small. The value of $\overline{\alpha}^p$ is lower than that of $\overline{\alpha}^s$ due to the atmospheric absorption, and the difference between $\overline{\alpha}^s$ and $\overline{\alpha}^p$ becomes roughly 0.1–0.3, although it depends on r_{eff}, θ_0 and the model atmospheres.

5.2 Effect of aerosols

The θ_0 dependence of spectrally integrated surface albedo for the atmosphere containing aerosols ($\overline{\alpha}^s_{4g+a}$) is shown in Fig. 13a. The effect of background aerosols $\tau_a = 0.02$ on $\overline{\alpha}^s$ is very small, and the curve is overlapped on that for aerosol free atmosphere ($\overline{\alpha}^s_{4g}$). When the optical depth of aerosols τ_a increases, the aerosols weaken the θ_0 dependence of $\overline{\alpha}^s$. This comes from the characteristic of θ_0 dependence of the monochromatic surface albedo, shown in Fig. 6a. The curve of $\overline{\alpha}^s_{4g+a}$ crosses that of $\overline{\alpha}^s_{4g}$ at around $\theta_0 = 55°$. That is, the aerosols increase $\overline{\alpha}^s$ at small θ_0, but reduce it at large θ_0. Blanchet and List (1987) showed the reduction of $\overline{\alpha}^s$ by 0.006 caused by their Arctic aerosol model 1 with $\tau_a = 0.081$ for $\theta_0 \sim 70°$ on the snow with the grain radius of 200 μm. The estimate of $\overline{\alpha}^s$ reduction by our aerosol model is 0.004 at $\tau_a = 0.1$, $\theta_0 = 70°$ and $r_{eff} = 200$ μm. According to Warren and Clark (1986) the aerosols, such as Arctic haze contained in snowfall and snowpack (snow impurities), could reduce $\overline{\alpha}^s$ up to 0.01–0.04 by absorbing the solar radiation in snow in the Arctic region. If the Antarctic snow is polluted by the absorptive impurities, the atmospheric aerosols could enhance its reduction of $\overline{\alpha}^s$ at $\theta_0 > 55°$.

The atmospheric aerosols have the effect of reducing the insolation to the surface by shading the downward solar radiation. Figure 13b shows the change in global solar radiation ($\overline{F}$) by aerosols as a function of θ_0. At small θ_0 the value of $\overline{F}$ is increased slightly by aerosols due to the reason that will be described in the next section. However, it is reduced by aerosols except for small θ_0. This reduction is estimated by 3 % for $\tau_a = 0.1$, and 11 % for $\tau_a = 0.3$ at $\theta_0 = 70°$. It is more significant than this for $\theta_0 > 70°$. From the viewpoint of the surface radiation budget in the shortwave region, this reduction in $\overline{F}$ (cooling the surface) compensates the reduction of $\overline{\alpha}^s$ (heating the surface) by the aerosols and snow impurities mentioned above. Particularly in the case of volcanic ash aerosols, the effect of reduction in $\overline{F}$ exceeds that of $\overline{\alpha}^s$ at $\theta_0 > 55°$.

Figure 13c shows the θ_0 dependence of spectrally integrated planetary albedo for the atmosphere containing aerosols ($\overline{\alpha}^p_{4g+a}$), where the curve of $\overline{\alpha}^p_{4g+a}$ with $\tau_a = 0.02$ overlaps with that for aerosol free atmosphere ($\overline{\alpha}^p_{4g}$). The effect of the background

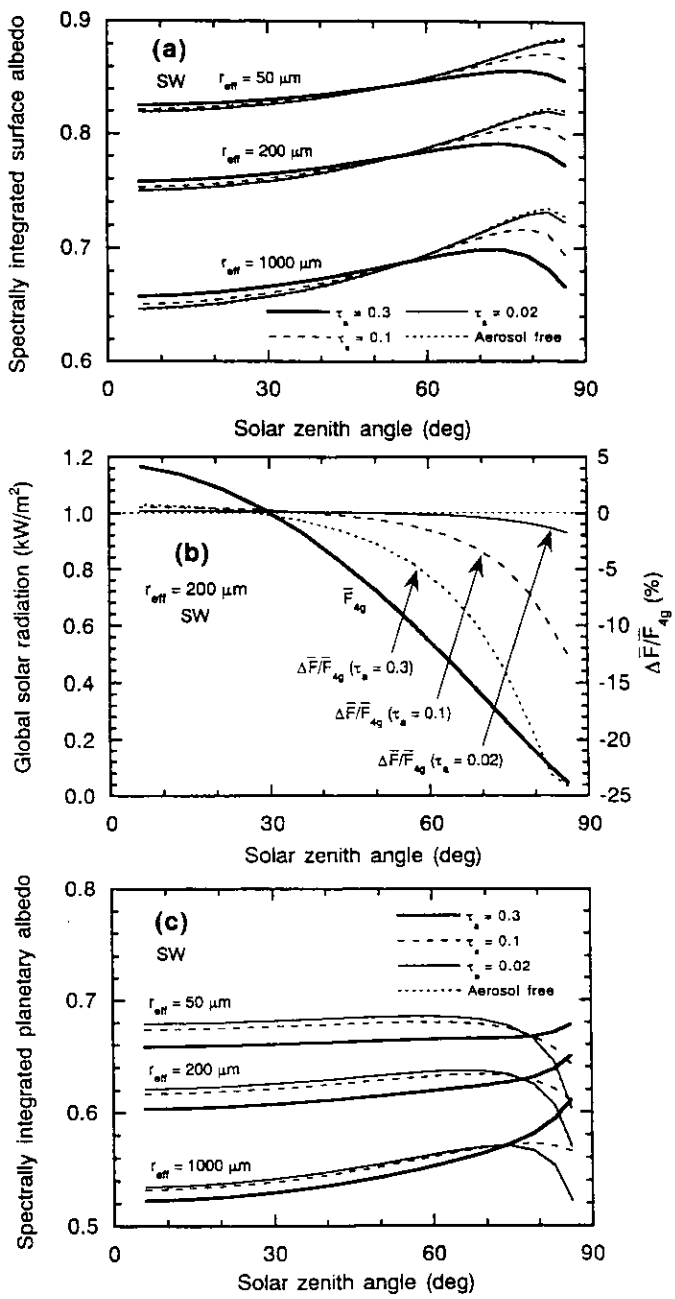

Fig. 13. (a) Same as Fig. 12a, but for the atmosphere of SW containing aerosols ($\overline{\alpha}^s_{4g+a}$) with three kinds of τ_a and aerosol free case ($\overline{\alpha}^s_{4g}$). (b) Global solar radiation ($\overline{F}_{4g}$) for aerosol free atmosphere of SW over the snow with $r_{eff} = 200$ μm (left ordinate) and the change in global solar radiation ($\Delta\overline{F}/\overline{F}_{4g}$) by the aerosols (right ordinate), where $\Delta\overline{F} = \overline{F}_{4g+a} - \overline{F}_{4g}$ and $\overline{F}_{4g+a}$ is the global solar radiation for the atmosphere of SW containing aerosols with three kinds of τ_a. (c) Same as Fig. 12b, but for the atmosphere of SW containing aerosols ($\overline{\alpha}^p_{4g+a}$) with three kinds of τ_a and aerosol free case ($\overline{\alpha}^p_{4g}$).

aerosols on $\overline{\alpha}^p$ is very small in the Antarctic, but this is due to small optical depth. In the cases of $\tau_a \geq 0.1$, the aerosols (mainly volcanic ash) reduce $\overline{\alpha}^p$ except at large θ_0. This means that the effect of volcanic ash in the Antarctic is positive (heating) on the radiation budget in the shortwave region at TOA except at large θ_0. Blanchet and List (1987) showed the reduction of $\overline{\alpha}^p$ by 0.021 caused by their Arctic aerosol model 1 with $\tau_a = 0.1$ for $\theta_0 \sim 70°$ on the snow with the grain radius of 200 μm. In our case the reduction of $\overline{\alpha}^p$ is estimated by 0.003 caused by the aerosols with $\tau_a = 0.1$ for $\theta_0 = 70°$ and $r_{eff} = 200$ μm. However, the reduction of $\overline{\alpha}^p$ amounts to 0.012 for $\tau_a = 0.3$. These results suggest that the thick volcanic ash aerosols over the Antarctic could have the effect of a same order as the Arctic haze at $\theta_0 = 70°$ on the radiation budget at TOA. On the other hand, volcanic ash increases $\overline{\alpha}^p$ of snow at large θ_0. Thus, it should be noticed that the radiative forcing of the Antarctic aerosols may vary with θ_0.

5.3 Effect of cloud cover

It is the well known phenomenon that the value of $\overline{\alpha}^s$ of snow under cloudy sky is higher than that for the clear case (Liljequist, 1956; Grenfell and Maykut, 1977; Wiscombe and Warren, 1980a; Warren, 1982; Yamanouchi, 1983). To reproduce such a situation theoretically, the spectrally integrated surface albedos are calculated in the case of a cloudy atmosphere ($\overline{\alpha}^s_{4g+c}$) for $r_{eff} = 50$ and 200 μm, and the cases of cloudy atmosphere ($\overline{\alpha}^s_{4g+c}$) and clear atmosphere ($\overline{\alpha}^s_{4g}$) for $r_{eff} = 1000$ μm (Fig. 14a). The value of $\overline{\alpha}^s_{4g+c}$ increases with τ_c and it becomes higher than $\overline{\alpha}^s_{4g}$ at any θ_0 for $\tau_c \geq 5$. This cannot be understood intuitively from the θ_0 dependence of the monochromatic surface albedo shown in Fig. 7a. Liljequist (1956) explained this phenomenon by the difference in spectral distribution of downward solar flux between the clear case and cloudy case. The details of this explanation could be given using Eq. (1) in the following: Under the cloudy atmosphere the downward solar flux $F^{\downarrow}(\lambda)$ is much smaller than that for the clear case in the near infrared region, whereas in the visible region both $F^{\downarrow}(\lambda)$ are not so much different or $F^{\downarrow}(\lambda)$ under the cloudy atmosphere is even larger than that for the clear case at small θ_0, as will be shown in the next section. On the other hand, the spectral surface albedo $\alpha^s(\lambda)$ is high in the visible region and low in the near infrared region under both clear and cloudy conditions. In Eq. (1) the spectrally integrated surface albedos $\overline{\alpha}^s$ is the flux weighted mean of $\alpha^s(\lambda)$ as mentioned in Subsection 5.1. Since the weight $(F^{\downarrow}(\lambda))$ for low $\alpha^s(\lambda)$ in the near infrared region is large for the clear case and small for the cloudy case, the value of $\overline{\alpha}^s_{4g+c}$ becomes higher than that of $\overline{\alpha}^s_{4g}$. In Fig. 14a it is also shown that the θ_0 dependence of

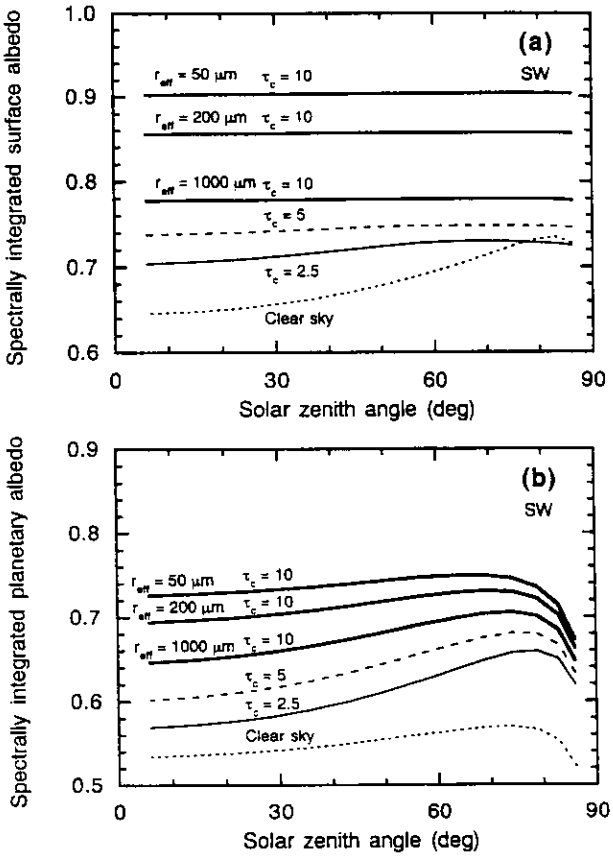

Fig. 14. (a) Spectrally integrated surface albedos as a function of θ_0 in the case of cloudy atmosphere of SW ($\overline{\alpha}^s_{4g+c}$) with $\tau_c = 10$ for $r_{eff} = 50$ and 200 μm, and the cases of cloudy atmospheres ($\overline{\alpha}^s_{4g+c}$) with three kinds of τ_c and clear atmosphere ($\overline{\alpha}^s_{4g}$) for 1000 μm. (b) Same as Fig. 14a, but for TOA in the cloudy case ($\overline{\alpha}^p_{4g+c}$) and clear case ($\overline{\alpha}^p_{4g}$).

$\overline{\alpha}^s_{4g+c}$ becomes weaker with the increase of τ_c. This comes from the characteristic of θ_0 dependence of the monochromatic surface albedo under the cloudy atmosphere shown in Fig. 7a. The cloud cover also has the effect to reduce the insolation to the surface by shading the downward solar radiation, as will be shown in the next section. Together with the effect of increasing $\overline{\alpha}^s$ mentioned above, the cloud cover has a cooling effect on the radiation budget in the shortwave region at snow surface.

Figure 14b shows the spectrally integrated planetary albedos for the cloudy atmosphere ($\overline{\alpha}^p_{4g+c}$), where $\overline{\alpha}^p_{4g+c}$ is higher than that for the clear case ($\overline{\alpha}^p_{4g}$) at any θ_0. This is because a cloud droplet is smaller than a snow grain and the single scattering albedo of a cloud droplet is higher than that of a snow grain. Thus, the cloud cover has the so-called "albedo effect" (cooling effect) on the radiation budget in the shortwave region at TOA. These results are consistent with the study of Yamanouchi and

Charlock (1995), using satellite data and radiation budget observation at the snow surface.

6. Effect of multiple reflection between snow surface and cloud cover

Wendler *et al.* (1981) discussed the increase of irradiance on the surface accompanied by the change of surface optical properties from tundra (low albedo) to snow (high albedo) under Arctic stratus cloud at Barrow, Alaska. They argued that this is due to the multiple reflection between snow surface and cloud cover. Yamanouchi (1983) also noticed that both the global solar radiations for clear and cloudy skies are larger than the observations in mid latitudinal regions due to the multiple reflection between snow surface and atmosphere (cloud cover).

Figure 15a shows the spectral distributions of downward solar flux ($F^{\downarrow}$) at snow surface under clear and cloudy skies, and $F^{\downarrow}$ at TOA (extraterrestrial solar flux). In the near infrared region, the value of $F^{\downarrow}$ is large in order of TOA, clear atmosphere, and cloudy atmosphere at any θ_0. In the visible region at $\theta_0 = 74.3°$ the value of $F^{\downarrow}$ are large in the same order as the near infrared region. However, at $\theta_0 = 43.2°$ the value of $F^{\downarrow}$ for the cloudy atmosphere is almost the same as that for the clear case, and both exceed the extraterrestrial solar flux in the region $0.375 \leq \lambda \leq 0.475$ μm. Furthermore, at $\theta_0 = 5.9°$ the value of $F^{\downarrow}$ for clear atmosphere is larger than the extraterrestrial solar flux for the broader region of $0.375 \leq \lambda \leq 0.525$ μm. The value of $F^{\downarrow}$ for the cloudy atmosphere exceeds both of $F^{\downarrow}$ for the clear case and extraterrestrial solar flux at almost all visible wavelengths.

The reason for this phenomenon is somewhat complicated to explain. We shall consider a simple model of cloud-snow system where there is no Rayleigh atmosphere, and no absorption by the atmospheric gases but only cloud. Let us denote the monochromatic surface albedo of snow by R_s, and those of cloud against the direct solar flux and upward solar flux by R_{cd} and R_{cu}, respectively. When the direct solar flux of an amount of unity illuminates this system, the total amount of monochromatic downward solar flux $F^{\downarrow}$ at the snow surface becomes

$$F^{\downarrow} = \frac{(1 - R_{cd})}{(1 - R_s R_{cu})}, \tag{2}$$

after the multiple reflection between snow surface and cloud layer. If R_{cd} and R_{cu} are the same, $F^{\downarrow}$ never exceeds unity. But they could be different in the real field. To examine this we only consider the visible region ($\lambda = 0.45$ μm) and small θ_0. The values of R_{cd} was calculated by one-layer cloud model with $\tau_c = 10$ (without underlying snow surface) illuminated by the direct solar beam, and we obtained $R_{cd} = 0.36$ at $\theta_0 = 5.9°$. For the calculation of R_{cu},

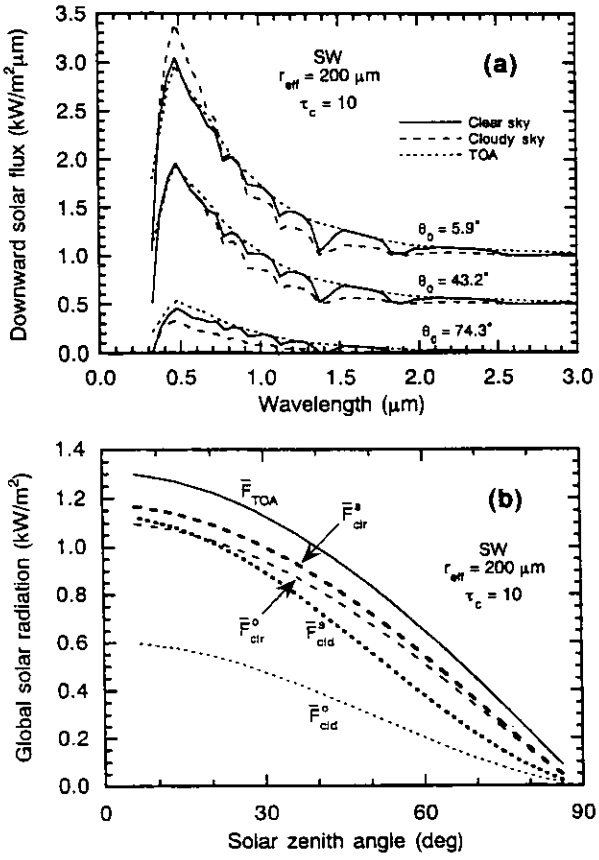

Fig. 15. (a) Spectral distribution of downward solar flux ($F^{\downarrow}$) at snow surface with $r_{eff} = 200$ μm under clear atmosphere of SW, and cloudy case with $\tau_c = 10$, and $F^{\downarrow}$ at TOA for three values of θ_0. Curves are successively displaced upward by 0.5 kW/m$^2\mu$m except for $\theta_0 = 74.3°$. (b) Global solar radiation at snow surface as a function of θ_0 for clear atmosphere ($\overline{F}^s_{clr}$) and cloudy case ($\overline{F}^s_{cld}$), that at sea surface for clear case ($\overline{F}^o_{clr}$) and cloudy case ($\overline{F}^o_{cld}$), and that at TOA ($\overline{F}_{TOA}$).

we assumed the cloud base is illuminated by diffuse radiation, which is equivalent to the direct insolation of solar beam at $\theta_0 = 48°$ as shown in Fig. 1b, and obtained $R_{cu} = 0.49$ from the one-layer cloud model described above. Similarly the snow surface is also illuminated by diffuse radiation, and we obtained $R_s = 0.98$ at $\theta_0 = 48°$ from one-layer snow model with $r_{eff} = 200$ μm illuminated by the direct solar beam. Using these parameters, we obtain $F^{\downarrow} = 1.23$, showing the downward solar flux on the snow surface exceeds the extraterrestrial solar flux.

For the case of clear atmosphere, R_{cd} and R_{cu} in Eq. (2) are replaced by the albedos of the atmosphere, R_{ad} and R_{au}, respectively. These values are calculated for the Rayleigh atmosphere illuminated by the direct solar beam without underlying snow surface, and we obtained $R_{ad} = 0.10$ at $\theta_0 = 5.9°$

Table 2. Major characteristics of the atmospheric effects on snow albedos: spectral surface albedo (α^s), spectral planetary albedo (α^p), spectrally integrated surface albedo ($\overline{\alpha}^s$) and spectrally integrated planetary albedo ($\overline{\alpha}^p$). Subscripts means as follows; $4g$: absorptive atmosphere with Rayleigh scattering, na: no atmosphere, AS: model atmosphere of Antarctic summer, MW: model atmosphere of midlatitude winter, $4g+a$: aerosol contained atmosphere, $4g+c$: cloudy atmosphere. Meanings of the other symbols are given in Table 1.

Albedo	Gaseous absorption and Rayleigh scattering	Difference of atmospheric type	Aerosols	Cloud cover
α^s	Gas: $\alpha^s_{4g} < \alpha^s_{na}$ in absorption bands at large θ_0, Rayleigh: Weaken the θ_0 dependence at $\lambda < 0.5$ μm (*1)	$\alpha^s_{MW} < \alpha^s_{AS}$ in H_2O bands at large θ_0	Weaken the θ_0 dependence (*1)	Weaken the θ_0 dependence (*1)
α^p	Gas: $\alpha^p_{4g} < \alpha^s_{4g}$ in absorption bands, Significant for small r_{eff}, Rayleigh: Slightly $\alpha^p_{4g} > \alpha^s_{4g}$ around $\lambda = 0.4$ μm	$\alpha^p_{MW} < \alpha^p_{AS}$ in H_2O bands	$\alpha^p_{4g+a} < \alpha^p_{4g}$ at shorter λ and $\alpha^p_{4g+a} > \alpha^p_{4g}$ at longer λ	$\alpha^p_{4g+c} > \alpha^p_{4g}$ in the near infrared (*2)
$\overline{\alpha}^s$	$\overline{\alpha}^s_{4g} > \overline{\alpha}^p_{4g}$, Significant for MW	$\overline{\alpha}^s_{MW} > \overline{\alpha}^s_{AS}$	Weaken the θ_0 dependence (*1)	Weaken the θ_0 dependence, $\overline{\alpha}^s_{4g+c} > \overline{\alpha}^s_{4g}$ at any θ_0 for large τ_c
$\overline{\alpha}^p$		$\overline{\alpha}^p_{MW} > \overline{\alpha}^p_{AS}$	$\overline{\alpha}^p_{4g+a} < \overline{\alpha}^p_{4g}$ except at large θ_0 and $\overline{\alpha}^p_{4g+a} > \overline{\alpha}^p_{4g}$ at large θ_0	$\overline{\alpha}^p_{4g+a} < \overline{\alpha}^p_{4g}$ at any θ_0

*1: Albedo is increased at small θ_0 and reduced at large θ_0, *2: Slightly $\alpha^p_{4g+c} < \alpha^p_{4g}$ for the visible, small θ_0 and small τ_c.

and $r_{au} = 0.14$ at $\theta_0 = 48°$ for $\lambda = 0.45$ μm. Using these values with $R_s = 0.97$ for direct illumination at $\theta_0 = 5.9°$, we obtain $F^{\downarrow} = 1.04$ showing again the downward solar flux on the snow surface is larger than the extraterrestrial solar flux.

The keys to the condition which these phenomena happen are "snow surface" (high R_s), "visible wavelength" (weak atmospheric absorption), and "small solar zenith angle" ($R_{cd} < R_{cu}$, $R_{ad} < R_{au}$). When θ_0 is large, R_{cd} (or R_{ad}) is not less than R_{cu} (or R_{au}), and thus $F^{\downarrow}$ never exceeds unity. For the near infrared region, the value of R_s is low and thus $F^{\downarrow}$ never exceeds unity again.

Figure 15b shows the spectrally integrated values (global solar radiation) of the downward solar flux at the snow surface under clear atmosphere ($\overline{F}^s_{clr}$) and the cloudy case ($\overline{F}^s_{cld}$), and those at the sea surface under the clear case ($\overline{F}^o_{clr}$) and the cloudy case ($\overline{F}^o_{cld}$) as a function of θ_0. For comparison, the corresponding value at TOA ($\overline{F}_{TOA}$) is also shown. In calculating the $\overline{F}^o_{clr}$ and $\overline{F}^o_{cld}$, the sea surface albedo was assumed to be Lambertian, with a value of 0.05 for all wavelengths. Although the monochromatic value of $F^{\downarrow}$ under the cloudy atmosphere exceeds the extraterrestrial solar flux at small θ_0 in the visible region as has seen above, $\overline{F}^s_{cld}$ never exceeds both $\overline{F}^s_{clr}$ and $\overline{F}_{TOA}$, and $\overline{F}^s_{clr}$ also never exceeds $\overline{F}_{TOA}$. On the other hand, $\overline{F}^s_{clr}$ (or $\overline{F}^s_{cld}$) is larger than $\overline{F}^o_{clr}$ (or $\overline{F}^o_{cld}$), and the ratio $\overline{F}^s_{clr}/\overline{F}^o_{clr}$ (or $\overline{F}^s_{cld}/\overline{F}^o_{cld}$) becomes 1.06 (or 1.87) at $\theta_0 = 5.9°$. These are due to the effect of multiple reflection between snow surface and the atmosphere (or cloud cover). In particular, the difference in global solar radiation between snow surface and sea surface is significant for the cloudy case. This shows the interaction between snow surface and cloud cover is very important for the radiation budget in the cryosphere.

7. Summary

The multiple scattering radiative transfer model for the atmosphere-snow system has been developed to estimate the atmospheric effects on the spectral and spectrally integrated snow albedos at the snow surface and TOA. In this model the interaction between the snow surface and atmosphere is calculated using the "doubling and adding" method for multiple scattering, combined with the Mie theory for single scattering by snow grain, aerosol particles and cloud droplets in the wavelength region from 0.3 to 3.0 μm. The atmospheric transmittance of gaseous absorption is calculated by the extended exponential-sum fitting of transmissions for three kinds of model atmospheres.

The surface albedo varies with the fraction of the diffuse component in the downward solar flux. This fraction changes with the atmospheric composition. As a result, the behavior of surface albedo is influenced by the atmosphere. The major characteristics of the atmospheric effects on snow albedos clarified in this study are summarized in Table 2. The atmospheric absorptive gases reduce the surface albedo α^s_{4g} in the absorption bands at large θ_0, compared with that for no atmosphere (α^s_{na}). In the H_2O absorption bands the surface albedo for H_2O rich atmosphere (α^s_{MW}) is lower than that for H_2O poor atmosphere (α^s_{AS}) for $\theta_0 > 63.1°$. However, the spectrally integrated surface albedo for MW ($\overline{\alpha}^s_{MW}$) is higher than that for AS ($\overline{\alpha}^s_{AS}$) by up to 0.021.

This is because the downward solar flux $F^{\downarrow}(\lambda)$ in the near infrared region is lower for H_2O rich MW than AS. This point is important for the interpretation of the snow albedo observed with such spectrally integrated instruments as pyranometers. On the other hand, the spectrally integrated planetary albedo for MW ($\overline{\alpha}^p_{MW}$) is lower than that for AS ($\overline{\alpha}^p_{AS}$) by up to 0.043. At any θ_0 the value of $\overline{\alpha}^p$ is lower than $\overline{\alpha}^s$ due to the atmospheric absorption. The difference between $\overline{\alpha}^p$ and $\overline{\alpha}^s$ lies in the range of 0.1–0.3.

Antarctic coastal aerosols weaken both the θ_0 dependences of spectral surface albedo α^s_{4g+a}, and spectrally integrated surface albedo $\overline{\alpha}^s_{4g+a}$ at almost all wavelengths. However, these aerosols have the effect of reducing the insolation to surface by the shading effect. Background sulfuric acid aerosols in the Antarctic have no significant effect on the planetary albedo α^p_{4g+a} (thus on $\overline{\alpha}^p_{4g+a}$), due to the low optical depth. The volcanic ash, however, reduces α^p_{4g+a} in the shorter wavelength region, and increases it in the longer wavelength region. The resultant effect on $\overline{\alpha}^p_{4g+a}$ by the volcanic ash is the reduction, except at large θ_0. Although these are basically due to the difference in single scattering albedo between the volcanic ash and snow grain, the difference in vertical profile between the volcanic ash and absorptive gases also affects the result.

High latitudinal middle clouds with large optical depth increase the spectrally integrated surface albedo $\overline{\alpha}^s_{4g+c}$ at any θ_0. This is explained by the difference in spectral distribution of downward solar flux between clear and cloudy cases. Due to this effect and the shading effect of insolation, the cloud cover has a cooling effect on the radiation budget in the shortwave region at the snow surface. The cloud cover increases the spectral planetary albedo α^p_{4g+c} in the near infrared region (and thus increases $\overline{\alpha}^p_{4g+c}$) at any θ_0 due to the difference of single scattering albedo between cloud droplet and snow grain. Thus, the cloud cover studied here has a cooling effect at any θ_0 in the shortwave region at TOA.

The downward solar flux on snow surface under cloudy sky can exceed that for clear case in the visible region at small θ_0, and both further exceed the extraterrestrial solar flux. This phenomenon is explained by the multiple reflection between snow surface and atmosphere (or cloud cover). Global solar radiation on snow surface under cloudy sky never exceeds that for clear case and that at TOA, but it is 1.87 times larger than that on the sea surface. Although the increase of downward solar flux by the presence of cloud cover over snow surface was observed in the past studies, the phenomenon that the downward solar flux exceeds the extraterrestrial solar flux has never been observed. This may be due to the lack of spectral observations under the condition of small θ_0 on snow surface. Such phenomenon may be observed at high mountain areas in the low latitude.

It has been found that the effects of clouds on albedo and radiation budget are important on the snow surface. We did not study the effects of high cloud or diamond dust, which frequently appear in the polar region. The investigations for such ice clouds with small optical depth are also important items in the snow covered area. However, the amount of their effects on snow albedo will be smaller than those studied in the present work.

Acknowledgments

We thank Prof. S. Warren of the University of Washington for his invaluable discussion and advise. This work has been done as part of "Snow and ice study using the data of ADEOS II / GLI" supported by NASDA (National Space Development Agency of Japan).

References

Aoki, Te., 1992: A multiple scattering model for the atmosphere-snow system. *Proc. NIPR Symp. Polar Meteor. Glaciol.*, **6**, 77–83.

Aoki, Te., Ta. Aoki and M. Fukabori, 1993: Spectral albedo and inside radiant flux density of snow by a multiple scattering model. in *Atmospheric Radiation*, Knut H. Stamnes, Editor, Proc. SPIE, **2049**, 275–278.

Aoki, Te., Ta. Aoki and M. Fukabori, 1997: Approximations of phase function in calculating the spectral albedo of snow surface with multiple scattering. *Pap. Met. Geophys.*, **47**, 141–156.

Aoki, Te., Ta. Aoki, M. Fukabori, Y. Tachibana, Y. Zaizen, F. Nishio and T. Oishi, 1998: Spectral albedo observation on the snow field at Barrow, Alaska. *Polar Meteor. Glaciol.*, **12**, 1–9.

Anderson, G.P., S.A. Clough, F.X. Kneizys, J.H. Chetwynd and E.P. Shettle, 1986: AFGL atmospheric constituent profiles (0–120 km). *AFGL-TR-86-0110*, Air Force Geophysics Laboratory, Hanscom, MA.

Asano, S. and A. Uchiyama, 1987: Application of an extended ESFT method to calculation of solar heating rates by water vapor absorption. *J. Quant. Spectrosc. Radiat. Transfer*, **38**, 147–158.

AFGL, 1985: *Handbook of geophysics and the space environment*. Air Force Geophysics Laboratory.

Barkstrom, B.R., 1972: Some effects of multiple scattering on the distribution of solar radiation in snow and ice. *J. Glaciol.*, **11**, 357–368.

Barkstrom, B.R. and C.W. Querfeld, 1975: Concerning the effect of anisotropic scattering and finite depth on the distribution of solar radiation in snow. *J. Glaciol.*, **14**, 107–124.

Bergen, J.D., 1970: A possible relation between grain size, density, and light attenuation in natural snow cover. *J. Glaciol.*, **9**, 154–156.

Bergen, J.D., 1971: The relation of snow transparency to density and air permeability in a natural snow cover. *J. Geophys. Res.*, **76**, 7385–7388.

Berger, R.H., 1979: Snowpack optical properties in the infrared. *CRREL Rep.*, **79-11**, U.S. Army Cold Reg. Res. and Eng. Lab., Hanover, N.H., 1–9.

Blanchet, J.-P. and R. List, 1987: On radiative effects of anthropogenic aerosol components in Arctic haze and snow. *Tellus*, **39B**, 293–317.

Bohren, C.F. and B.R. Barkstrom, 1974: Theory of the optical properties of snow. *J. Geophys. Res.*, **79**, 4527–4535.

Carroll, J.J., 1982: The effect of surface striations on the absorption of shortwave radiation. *J. Geophys. Res.*, **87**, 9647–9652.

Carroll, J.J. and B.W. Fitch, 1981: Effects of solar elevation and cloudiness on snow albedos at the south pole. *J. Geophys. Res.*, **86**, 5271–5276.

Choudhury, B.J. and A.T.C. Chang, 1979a: Two-stream theory of reflectance of snow. IEEE Trans. *Geosci. Electron.*, **GE-17**, 63–68.

Choudhury, B.J. and A.T.C. Chang, 1979b: The solar reflectance of a snow field. *Cold Reg. Sci. Technol.*, **1**, 121–128.

Choudhury, B.J., 1981: Radiative properties of snow for clear sky solar radiation. *Cold Reg. Sci. Technol.*, **4**, 103–120.

Choudhury, B.J. and A.T.C. Chang, 1981a: On the angular variation of solar reflectance of snow. *J. Geophys. Res.*, **86**, 465–472.

Choudhury, B.J. and A. T.C. Chang, 1981b: The albedo of snow for partially cloudy sky. *Boundary layer Meteor.*, **20**, 371–389.

Chýlek, P., V. Ramaswamy and V. Srivastava, 1983: Albedo of soot-contaminated snow. *J. Geophys. Res.*, **88**, 10837–10843.

Deirmendjian, D., 1964: Scattering and polarization properties of water clouds and hazes in the visible and infrared. *Appl. Opt.*, **3**, 187–196.

Downing, H.D. and D. Williams, 1975: Optical constants of water in the infrared. *J. Geophys. Res.*, **80**, 1656–1661.

Dunkle, R.V. and J.T. Bevans, 1956: An approximate analysis of the solar reflectance and transmittance of a snow cover. *J. Meteor.*, **13**, 212–216.

Giddings, J.C. and E. LaChapelle, 1961: Diffusion theory applied to radiant energy distribution and albedo of snow. *J. Geophys. Res.*, **66**, 181–189.

Grenfell, T.C. and G.A. Maykut, 1977: The optical properties of ice and snow in the Arctic Basin. *J. Glaciol.*, **18**, 445–463.

Grenfell, T. C., S. G. Warren, and P. C. Mullen, 1994: Reflection of solar radiation by the Antarctic snow surface at ultraviolet, visible and near-infrared wavelengths. *J. Geophys. Res.*, **99**, 18669-18684.

Hale, G.M. and M.R. Querry, 1973: Optical constants of water in the 200 nm to 200 μm wavelength region. *Appl. Opt.*, **12**, 555–563.

Hansen, J.E., 1969: Exact and approximate solutions for multiple scattering by cloud and hazy planetary atmosphere. *J. Atmos. Sci.*, **26**, 478–487.

Hansen, J.E., 1971: Multiple scattering of polarized light in planetary atmospheres. Part II. Sunlight reflected by terrestrial water clouds. *J. Atmos. Sci.*, **28**, 1400–1426.

Herber, A., L.W. Thomason, K. Dethloff, P. Viterbo, V. F. Radionov and U. Leiterer, 1996: Volcanic perturbation of the atmosphere in both polar regions: 1991–1994. *J. Geophys. Res.*, **101**, 3921–3928.

Higuchi, K., H. Fushimi, T. Ohata, S. Takenaka, S. Iwata, K. Yokoyama, H. Higuchi, A. Nagoshi and T. Iozawa, 1980: Glacier inventory in the Dudh Kosi region, East Nepal. *IAHS Publ.*, **126**, 95–101.

Ito, T., 1989: Antarctic submicron aerosols and long-range transport of pollutants. *Ambio*, **18**, 34–41.

JMA, 1995: *Antarctic meteorological data, Summary of meteorological observations at Syowa, Mizuho and Asuka Stations, 1961–1993, Special volume VI.* Japan Meteorological Agency.

Kaneto, S., T. Kishi and meteorological stuff of 33rd and 34th Japanese Antarctic Research Expeditions, 1994: Aerosol optical depth observation by JARE-33 and JARE-34 in 1991 and 1992. *Proc. NIPR Symp. Polar Meteor. Glaciol.*, **8**, 19–26.

Kneizys, F.X., E.P. Shettle, W.O. Gallery, J.H. Chetwynd, Jr., L.W. Abreu, J.E.A. Selby, S.A. Clough and R.W. Fenn, 1983: Atmospheric Transmittance/Radiance: Computer code LOWTRAN 6. *AFGL-TR-83-0187*, Air Force Geophysics Laboratory, Hanscom, MA.

Li, S., 1982: *A model for the anisotropic reflectance of pure snow.* M.S. thesis, 60pp, Univ. of Calif., Santa Barbara.

Liljequist, G.H., 1956: Energy exchange of an Antarctic snow-field: Short-wave radiation. in *Norwegian-British-Swedish Antarctic Expedition, 1949–52, Scientific Results*, Vol. 2, Part 1A, Norsk Polarinstitutt, Oslo.

Liou, K.N., 1992: *Radiation and cloud process in the atmosphere.* Oxford University Press, 487pp.

Marshall S. and S.G. Warren, 1986: Parameterization of snow albedo for climate models. *Glaciological Data*, **18**, 215–223.

Mellor, M., 1977: Engineering properties of snow. *J. Glaciol.*, **19**, 15–66.

Ose, T., 1996: The comparison of the simulated response to the regional snow mass anomalies over Tibet, Eastern Europe, and Siberia. *J. Meteor. Soc. Japan*, **74**, 845–866.

Palmer, K.F. and D. Williams, 1974: Optical properties of water in the infrared. *J. Opt. Soc. Am.*, **64**, 1107–1110.

Potter, J.F., 1970: The delta function approximation in radiative transfer theory. *J. Atmos. Sci.*, **27**, 943–949.

Shaw, G.E., 1982; Atmospheric turbidity in the polar regions. *J. Appl. Meteor.*, **21**, 1080–1088.

Shiobara, M., M. Tanaka, T. Nakajima and H. Ogawa, 1987: Spectral measurements of direct solar radiation and the sky brightness distribution at Syowa Station, Antarctica. in *Atmospheric Radiation — Progress and Prospects*, K.-N. Liou and Z. Xiuji (Eds.), Science Press, Beijing and Amer. Meteor. Soc., Boston, 629–637.

Thekaekara, M.P., 1974: Extraterrestrial solar spectrum, 3000–6100 Å at 1-Å intervals. *Appl. Opt.*, **13**, 518–522.

Uchiyama, A., 1992: Line-by-line computation of the atmospheric absorption spectrum using the decomposed Voigt line shape. *J. Quant. Spectrosc. Radiat. Transfer*, **47**, 521–532.

Valovcin, F.R., 1978: Spectral radiance of snow and clouds in the near infrared spectral region. *AFGL-TR-78-0289*, Air Force Geophysics Laboratory, Hanscom, MA.

Warren, S.G. and W.J. Wiscombe, 1980: A model for the spectral albedo of snow, II: Snow containing atmospheric aerosols. *J. Atmos. Sci.*, **37**, 2734–2745.

Warren, S.G., 1982: Optical properties of snow. *Rev. Geophys. Space Phys.*, **20**, 67–89.

Warren, S.G., 1984: Optical constants of ice from the ultraviolet to the microwave. *Appl. Opt.*, **23**, 1206–1225.

Warren, S.G. and A.D. Clarke, 1986: Soot from Arctic haze: radiative effects on the Arctic snowpack. *Glaciological Data*, **18**, 73–77.

Warren, S.G., W. Wiscombe and J.F. Firestone, 1990: Spectral albedo and emissivity of CO2-snow in Martian polar caps: model results. *J. Geophys. Res.*, **95**, 14717–14741.

Warrick, R.A., C. Le Provost, M.F. Meier, J. Oerlemans and P.L. Woodworth, 1995: Change in sea level, Chapter 7 in *Climate Change 1995*, Cambridge University Press, 572pp.

Wendler, G., D. Eaton and T. Ohtake, 1981: Multiple reflection effects on irradiance in the presence of Arctic stratus clouds. *J. Geophys. Res.*, **86**, 2049–2057.

Wendler, G. and J. Kelley, 1988: On the albedo of snow in Antarctica: Contribution to I.A.G.O. *J. Glaciol.*, **34**, 19–25.

Wiscombe, W.J., 1976: On initialization, error and flux conservation in the doubling method. *J. Quant. Spectrosc. Radiat. Transfer*, **16**, 637–658.

Wiscombe, W.J., 1977: The delta-M method: Rapid yet accurate radiative flux calculations for strongly asymmetric phase functions. *J. Atmos. Sci.*, **34**, 1408–1422.

Wiscombe, W.J. and S. G. Warren, 1980a: A model for the spectral albedo of snow, I: Pure snow. *J. Atmos. Sci.*, **37**, 2712–2733.

Wiscombe, W.J. and S.G. Warren, 1980b: Solar and infrared radiation calculations for the Antarctic Plateau using a spectrally-detailed snow reflectance model. in *International Radiation Symposium Volume of Extended Abstract*, 380–382, Colorado State University, Fort Collins.

Yamada, T., T. Shiraiwa, H. Iida, T. Kadota, T. Watanabe, B. Rana, Y. Ageta and H. Fushimi, 1992: Fluctuation of the glaciers from the 1970s to 1989 in the Kumbu, Shorong and Langtang regions, Nepal Himalayas. *Bull. Glacier Res.*, **10**, 11–19.

Yamanouchi, T., 1983: Variation of incident solar flux and snow albedo on the solar zenith angle and cloud cover, at Mizuho Station, Antarctica. *J. Meteor. Soc. Japan*, **61**, 879–893.

Yamanouchi, T., T.P. Charlock, 1995: Comparison of radiation budget at the TOA and surface in the Antarctic from ERBE and ground surface measurements. *J. Climate*, **8**, 3109–3120.

Yasunari, T., A. Kitoh and T. Tokioka, 1991: Local and remote responses to excessive snow mass over Eurasia appearing in the northern spring and summer climates. — A study with MRI.GCM —. *J. Meteor. Soc. Japan*, **69**, 473–487.

大気—積雪系の多重散乱放射伝達モデルによる積雪アルベドに及ぼす大気の効果の数値シミュレーション

青木輝夫・青木忠生・深堀正志・内山明博
（気象研究所）

雪面及び大気上端 (TOA) における波長別及び波長積分した積雪アルベドに対する大気の効果を調べた。そこでは空気分子、吸収気体、エアロゾル、雲による吸収と散乱の効果を、doubling and adding 法と Mie 理論に基づいた大気—積雪系の多重散乱放射伝達モデルによって見積もった。

波長別雪面アルベドは太陽天頂角が大きいとき、大気中の吸収気体によって大気がないときに比べて減少することが示された。その太陽天頂角依存性は波長 0.5 μm 以下でレイリー散乱によって弱められ、ほとんどの波長でエアロゾル及び雲によって弱められた。水蒸気の豊富な大気は、太陽天頂角が大きいとき、水蒸気の吸収帯で波長別アルベドを減少させた。ところが近赤外域の下向きフラックスが水蒸気の吸収によって減少するため、波長積分したアルベドは数パーセント高くなった。エアロゾルは太陽天頂角が小さいとき波長積分した雪面アルベドを増加させ、太陽天頂角が大きいときには減少させた。しかし、エアロゾルは太陽天頂角が大きいときを除き、波長積分したプラネタリーアルベドを減少させた。光学的に厚い雲は太陽天頂角に依らず波長積分した雪面及びプラネタリーアルベドの両者を増加させた。

太陽天頂角が小さいとき可視域では、雪面上における曇天時の下向きフラックスが晴天時のそれを上回り、また両者はさらに大気外日射フラックスを上回り得ることがわかった。この現象は雪面と大気 (雲) の間の多重反射によって説明できる。しかし、雪面上における曇天時の全天日射量は、晴天時及び TOA におけるそれらを上回ることはなかった。

Chapter 3

Spectral albedo observation on the snow field at Barrow, Alaska

Reprinted from

Polar Meteorology and Glaciology, No. 12

SPECTRAL ALBEDO OBSERVATION ON THE SNOW FIELD AT BARROW, ALASKA

Teruo AOKI, Tadao AOKI, Masashi FUKABORI, Yoshihiro TACHIBANA, Yuji ZAIZEN, Fumihiko NISHIO and Tomohiko OISHI

National Institute of Polar Research, Tokyo, November 1998

Polar Meteorol. Glaciol., **12**, 1–9, 1998

SPECTRAL ALBEDO OBSERVATION ON THE SNOW FIELD AT BARROW, ALASKA

Teruo AOKI[1], Tadao AOKI[1], Masashi FUKABORI[1], Yoshihiro TACHIBANA[2], Yuji ZAIZEN[1], Fumihiko NISHIO[3] and Tomohiko OISHI[4]

[1]*Meteorological Research Institute, 1–1, Nagamine, Tsukuba 305-0052*
[2]*Research Institute of Civilization, Tokai University, 1117, Kitakaname, Hiratsuka 259-1292*
[3]*Hokkaido University of Education, Shiroyama 1-chome, Kushiro 085-8580*
[4]*Tokai University, Orido 3-chome, Shimizu, 424-8610*

Abstract: Spectral albedo observation at the visible and near infrared wavelengths was carried out on the snow field at Barrow, Alaska in April, 1997. The data are compared with the theoretical calculations made by a multiple scattering radiative transfer model for the atmosphere-snow system using the snow physical parameters observed by snow pit work. It is found that the optically effective snow grain size is of the order of branch size for new snow consisting of dendrites, but is not of the crystal size. The observed spectral albedo was lower than theoretically calculated for "pure snow" in the visible and a part of the near infrared; such reduction is explained by the internal mixture of soot and external mixture of dust for snow particles. The theoretical spectral albedo calculated for a two-layer snow model that contains impurities agrees very well with the observations at all wavelengths.

1. Introduction

The cryosphere is a very sensitive region for climate change and has large feedback effects for the climate system. Snow and ice albedos in the visible region are very high and this makes the cryosphere act as a cold source on the global scale. However, soot in the Arctic snowpack originating from the Arctic haze reduces the albedo by up to 0.035 (WARREN and CLARKE, 1986). Such a reduction of snow albedo acts to accelerate the snow melting and reduces the albedo further. On the other hand, the near infrared albedo decreases with increase of the snow grain size (WISCOMBE and WARREN, 1980). In general, the snow grain size increases with snow age due to sintering that depends on the snow temperature. Thus, we may say that the snow grain size reflects the history of the snow.

There are possibilities of remote sensing for snow impurities by observation of the visible albedo, and the snow grain size using the near infrared albedo (WARREN, 1982). One of the most suitable optical sensors for such observations may be the GLI (Global Imager) in ADEOS-II (Advanced Earth Observing Satellite-II) that will be launched in 1999. GLI has 36 channels from the visible to infrared regions with 250 m or 1 km spatial resolution, 1600 km swath and global coverage in 4 days (NAKAJIMA *et al.*, 1994). We will estimate the snow impurities and snow grain size with GLI data. The basis of these studies is a multiple scattering radiative transfer model for the

atmosphere-snow system that simulates the spectral albedos at the snow surface and the top of the atmosphere. To validate this model, field observations for the spectral albedo and snow physical parameters have been done on the snow field at Barrow, Alaska, from April 14 to 27, 1997. Under a clear sky, even a gentle slope of the snow surface affects the snow albedo (GRENFELL and WARREN, 1994). As a simpler case in which it is unnecessary to consider such an effect, the relation between the spectral albedo and snow physical parameters under overcast condition on April 21 after new snowfall is discussed in this study.

2. Observation

The observation site was a snow field on tundra 5 km of northeast of Barrow town as shown in Fig. 1. The snow depth was 60 cm and the surface was covered by new snow of 1 cm depth that fell on the day before the observation (Fig. 2). The grain shape of surface new snow was dendrites with crystal size (radius) of 1–2 mm and branch size (radius) of 20–50 μm. The second layer was fine-grained old snow with the grain radius of 100–150 μm and the third layer was faceted crystals with the grain radius of 250–400 μm. The lowest two layers were depth hoar with the grain radius of 1–3 mm. These grain sizes were estimated using a portable microscope. Snow impurities were filtered within a day by 25-mm Nuclepore filters with the pore size of 0.2 μm after melting the snow samples of the surface and 5–10 cm depth snow layers. The concentrations of impurities were estimated by direct weight measurements of the Nuclepore filters, before and after filtering, with a balance. The sky condition was overcast with altocumulus. Air and snow surface temperatures were -14.2°C and -11.0°C, respectively at 1200 LT.

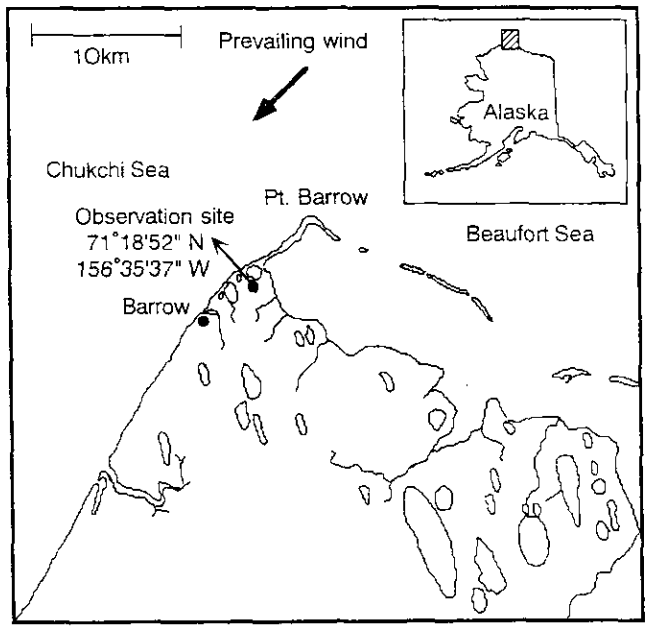

Fig. 1. Location map of the observation site around Barrow.

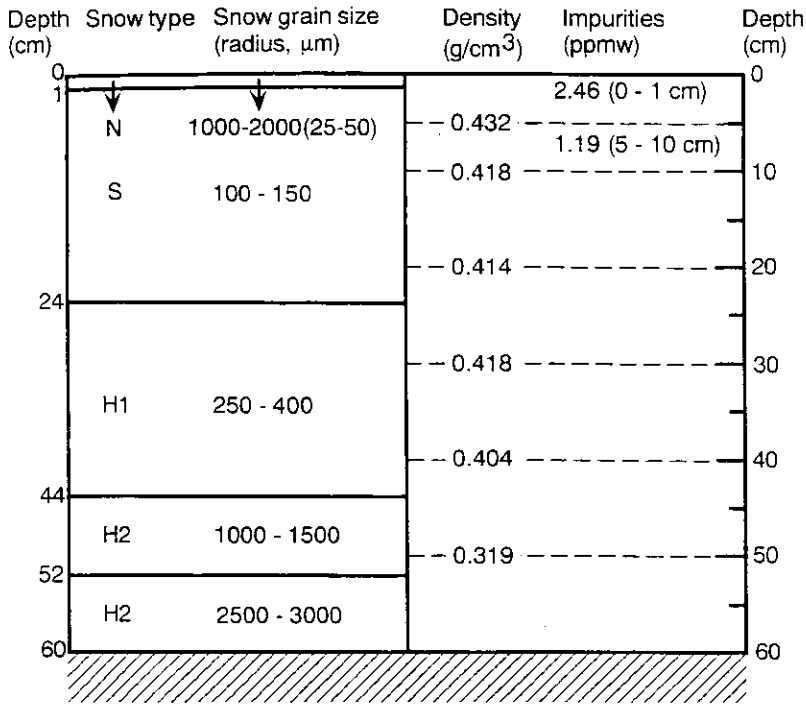

Fig. 2. Vertical profile of the snowpack used for the spectral albedo observations. Snow types are indicated by N for new snow, S for fine-grained old snow, H1 for faceted crystals and H2 for depth hoar. Snow grain sizes were estimated by the portable microscope. The values in parentheses in the surface layer indicate the branch size of the dendrites. Snow impurities were filtered within a day by 25-mm Nuclepore filters with pore size of 0.2 μm and the concentrations were estimated by direct weighting of Nuclepore filters with a balance.

The spectral snow albedo was observed by a grating type spectrometer, "FieldSpec FR", made by ASD Inc. (USA). It is necessary to observe the downward and upward flux to obtain the albedo. The downward flux was observed by directing the optical fiber of the spectrometer toward the surface of a standard white reflection plate that is set horizontally above the snow surface (Fig. 3). This method has the merit that the so-called "cosine property" of reflection is very good compared with the case of using a cosine collector. The upward flux was observed by directing the optical fiber toward the underside of the standard white reflection plate. Another advantage is that it is unnecessary to know the reflectance of the standard white reflection plate. The scanning spectral range of the spectrometer is 0.35–2.5 μm with the spectral resolution of 3 nm for the wavelength (λ) of 0.35–1.0 μm and 10 nm for λ= 1.0–2.5 μm. The scanning time is one second with the sampling interval of 1 nm for the full spectral range. Detectors are one dimensional Si photodiode CCDs for λ=0.35–1.0 μm and two different types of InGaAs photodiode for λ= 1.0–1.8 μm and λ= 1.8–2.5 μm. The spectral snow albedo is the average of five spectral albedos obtained from five pairs of measurements for the downward and snow reflected solar fluxes. It takes several minutes to obtain these quantities. To calculate the albedo, we used the raw digitized out-

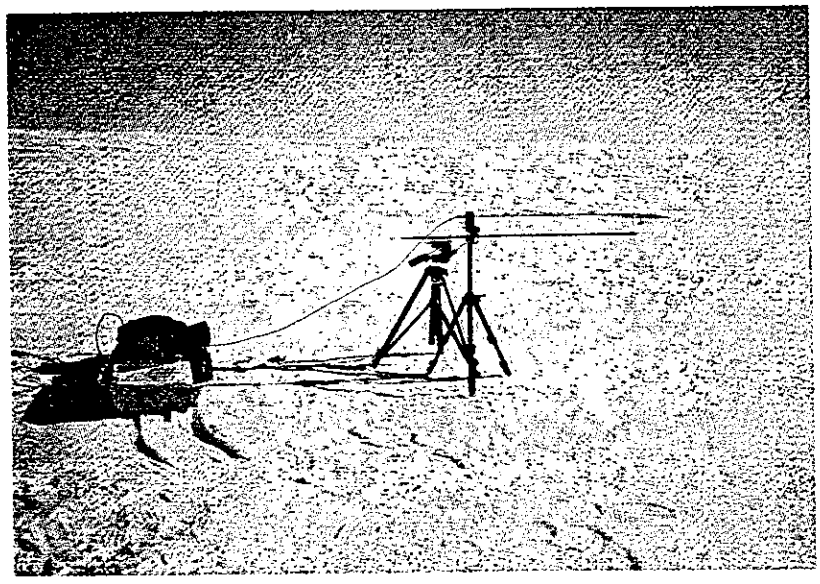

Fig. 3. A photo of the measurements of the downward solar flux on the snow surface with the spectrometer.

put count from the detector in which there is less error than the value calibrated with a standard lamp.

3. Radiative Transfer Model

The observed spectral snow albedo is compared with the theoretical calculations by a multiple scattering model for the atmosphere-snow system. In the snow layer(s), snow grains are assumed to be mutually independent ice particles and radiative transfer is treated the same as the usual multiple scattering model in the atmosphere containing aerosols or cloud particles. Radiative transfer processes are based on the Mie theory for single scattering and the "doubling and adding" method for multiple scattering omitting polarization (for details see AOKI *et al.*, 1997). According to AOKI *et al.* (1999), the effect of gaseous absorption on the spectral snow albedo is less than 0.01 at the solar zenith angle $\theta_0=64^\circ$, at which our observation was made, so that we neglected gaseous absorption. Since the effect of cloud on spectral albedo cannot be ignored (WISCOMBE and WARREN, 1980), we assumed an ice cloud layer of 4–5 km height in the Rayleigh atmosphere. The optical depth of cloud is 10 at $\lambda=0.5$ μm and Deirmendjian's cloud model (DEIRMENDJIAN, 1964) with the effective radius 15 μm is employed for the size distribution. Since the effect of aerosols on the snow albedo is smaller than that of cloud (AOKI *et al.*, 1999), the aerosols were not considered in the model atmosphere.

4. Results and Discussion

4.1. Snow grain size

The observed spectral albedo is compared with the theoretical calculations for a

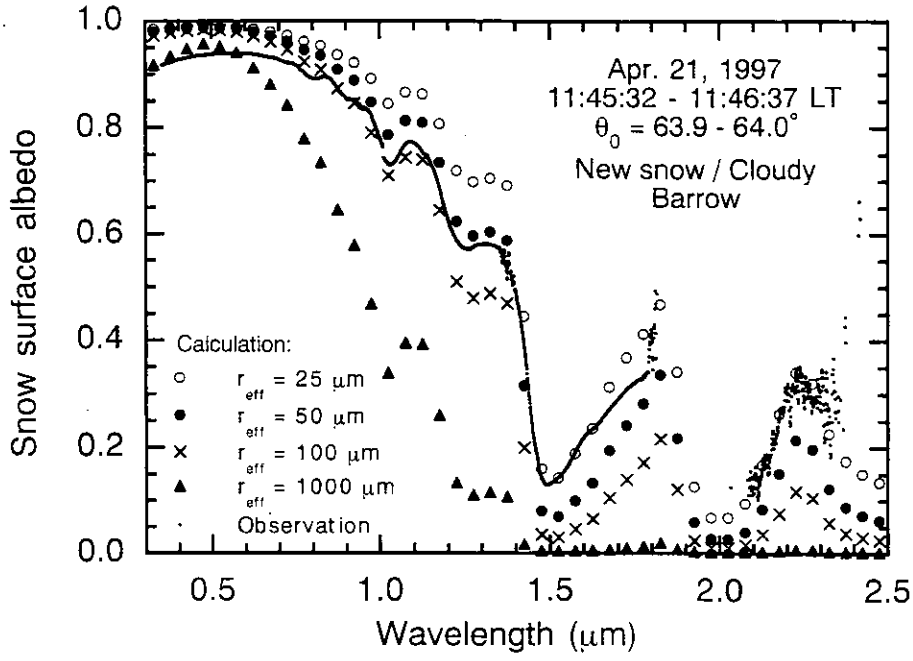

Fig. 4. Observed spectral snow albedo on April 21, 1997 at Barrow and theoretical results for the effective snow grain radii (r_{eff}) of 25, 50, 100 and 1000 μm, and the semi-infinite geometric depth. Solar zenith angle (θ_0) was 63.9–64.0° during the observations and that for theoretical calculation is 64.0°.

single snow layer with the effective snow grain radii (r_{eff}) of 25, 50, 100 and 1000 μm. Figure 4 shows the observed and theoretical spectral albedos. In the absorption bands of the atmospheric water vapor and carbon dioxide such as the wavelength regions $1.8<\lambda<2.0$ μm and $\lambda>2.4$ μm, the energy of downward solar flux is so weak compared to the detector sensitivity that the obtained spectral albedo highly fluctuates. Thus, observational data in which the downward or snow reflected solar flux is zero are not shown in Fig. 4. The observed albedo is lower than any theoretical results for $r_{eff}=25$–100 μm at the wavelengths $\lambda<0.9$ μm and that for $r_{eff}=1000$ μm at the wavelengths $\lambda<0.6$ μm. WARREN and WISCOMBE (1980) showed that snow impurities reduce the spectral albedo mainly in the visible region. This is because the difference of absorption coefficient between ice and impurities such as soot and dust becomes maximum in the visible region. The discrepancy between observed and calculated albedos for $\lambda<0.9$ μm or $\lambda<0.6$ μm in Fig. 4 seems to be due to the snow impurities as will be examined in the following sections. The theoretical spectral albedo for $r_{eff}=25$ μm agrees well with the observed one for $\lambda>1.5$ μm. In this region, there is no significant effect of snow impurities on spectral albedo (WARREN and WISCOMBE, 1980). The grain shape of surface new snow on the observation site was dendrites with crystal size (radius) of 1–2 mm and branch size (radius) of 25–50 μm. The theoretical spectral albedo for $r_{eff}=1000$ μm is considerably different from the observed one at all of the near infrared wavelengths. We, therefore, conclude that the optically effective snow grain size is on the order of branch size for the snow of dendrites, but is not of the crystal size.

4.2. Snow impurities

The observed concentration of snow impurities was 2.46 ppmw for surface snow and 1.19 ppmw for 5–10 cm depth. These were the results of direct weight measurements of Nuclepore filters on which the impurities were stuck by passing the melted snow sample. We have not yet analyzed the constituents of impurities, but according to the microscopic observation of impurities on Nuclepore filters, mineral particles with size smaller than 50 μm and further small unknown particles were recognized. Theoretical spectral albedos were calculated for snow with $r_{eff}=25$ μm and three kinds of impurities, including soot-contaminated snow containing 2 ppmw internal mixture, soot-contaminated snow containing 2 ppmw external mixture and dust-contaminated snow containing 2 ppmw external mixture. For external mixture, the method by WARREN and WISCOMBE (1980) is used for the soot and dust whose effective radii are 0.1 μm and 1.0 μm, respectively. For the internal mixture, eqs. (13)–(14) in CHÝLEK *et al.* (1983) with the same soot size as the external mixture and soot density $\rho_s=1.0$ g/cm^3 (WARREN and WISCOMBE, 1980) are used. The refractive indices are assumed to be $m=1.8$–$0.5i$ for soot, and the compiled data by AFGL (1985) are used for dust.

Figure 5 shows the comparison of the observed spectral albedo with the theoretical results for three kinds of snow impurities. The amount of 2 ppmw dust is too low and the amount of 2 ppmw soot is too high even for internal and external mixtures to account for the observed spectral albedo at the wavelengths λ <0.9 μm. This suggests that a small amount of highly absorptive material such as soot, and large amount

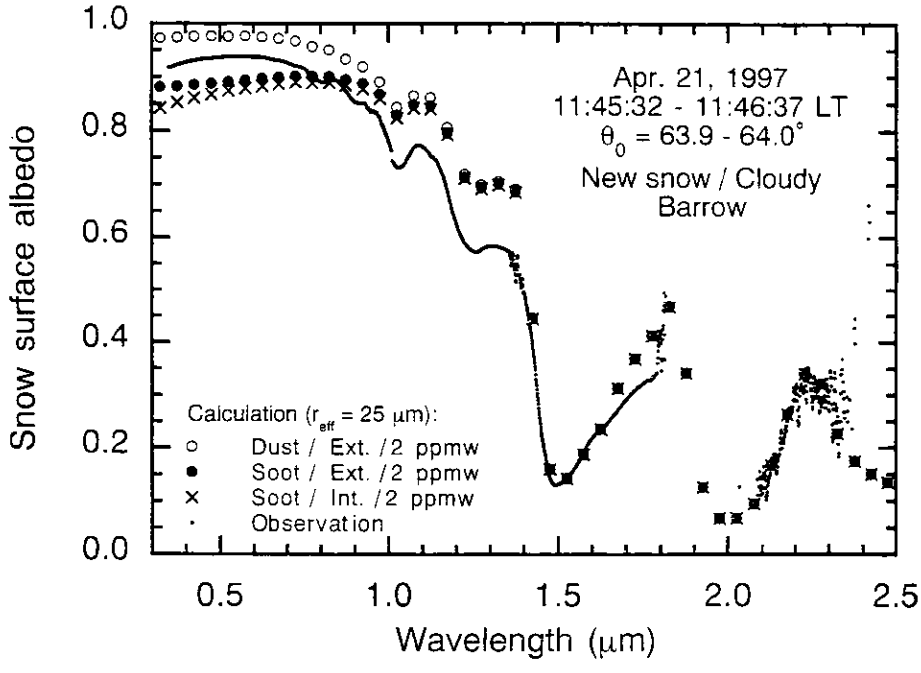

Fig. 5. Same as Fig. 4, except for theoretical results, which are calculated for $r_{eff}=25$ μm with soot-contaminated snow containing 2 ppmw internal mixture, soot-contaminated snow containing 2 ppmw external mixture and dust-contaminated snow containing 2 ppmw external mixture.

of weakly absorptive material such as dust, are simultaneously contained in the snow. The former contributes to the spectral albedo reduction in the visible and a part of the near infrared, and the latter contributes to raise the concentration of snow impurities measured by using Nuclepore filters. Therefore, we must consider a contaminated snow model with both soot and dust. However, impurities cannot account for the discrepancy between theoretical and observed albedos at the wavelengths $0.9<\lambda<1.35$ μm. This discrepancy and the spectral albedo reduction by snow impurities at $\lambda < 0.9$ μm are further studied by calculating the spectral albedo for a two-layer snow model in the following section.

4.3. Snow layer structure

The observed geometric depth of the surface layer was 1 cm (Fig. 2), but we could not measure the density due to the very low density and thinness of the layer. It is known that the mean density of new snow consisting of spatial dendrites is 0.036–0.059 g/cm^3 except in a snowstorm, and the minimum is 0.02 g/cm^3 (KAJIKAWA, 1989). There was no snowstorm when new snow fell on the surface on April 20 at Barrow. So we assume the density of new snow to be 0.05 g/cm^3.

We calculated the theoretical spectral albedos for some combinations of snow layer structure and snow impurities and obtained the best fitting of theoretical spectral albedo to the observed one (Fig. 6). The theoretical calculations were carried out

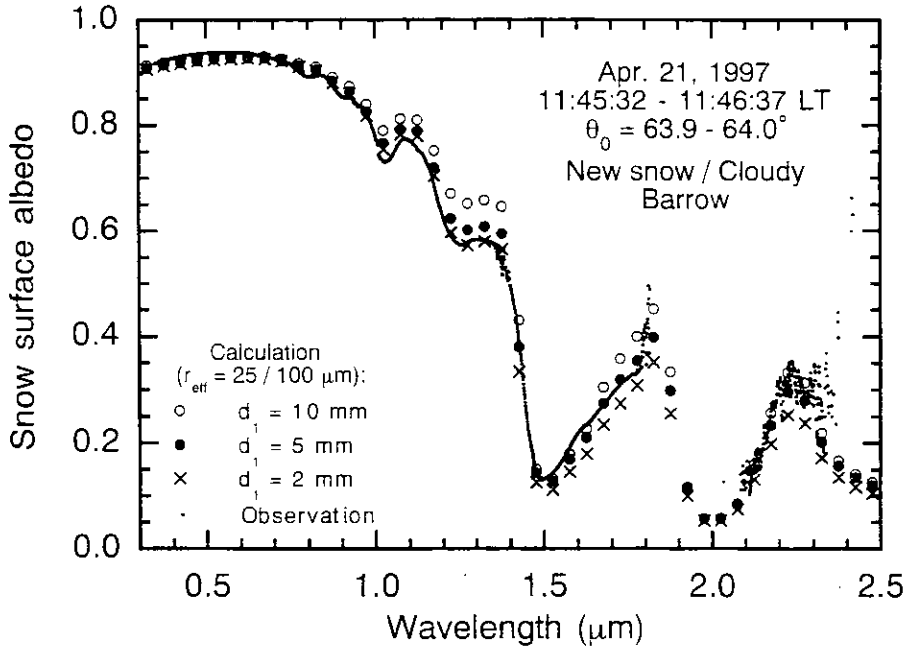

Fig. 6. Same as Fig. 4, except for theoretical results. The theoretical calculations are done for two-snow layer models with three geometric depths (d_1), 2, 5 and 10 mm, with density of 0.05 g/cm^3 and r_{eff}=25 μm in the first layer, and semi-infinite geometric depth with r_{eff}=100 μm in the second layer. The first snow layer is contaminated by 0.1 ppmw internal soot mixture and 2 ppmw external dust mixture. The second snow layer is contaminated by 0.1 ppmw internal soot mixture and 1 ppmw external dust mixture.

for two-layer snow models with three geometric depths (d_1), 2, 5 and 10 mm, with density of 0.05 g/cm^3 and $r_{eff}=25$ μm, in the first layer, and semi-infinite geometric depth with $r_{eff}=100$ μm in the second layer. The first snow layer is contaminated with 0.1 ppmw internal soot mixture and 2 ppmw external dust mixture. The second snow layer is contaminated by 0.1 ppmw internal soot mixture and 1 ppmw external dust mixture.

Good agreement is obtained for the model with geometric depth $d_1=2$ and 5 mm for the first layer at almost all wavelengths. In the case of $d_1=10$ mm, which is the value observed in this study, the theoretical spectral albedo is higher than the observed one by 0.05 to 0.1 at the wavelengths $1.0<\lambda<1.35$ μm. If we assume the value of snow density to be 0.02 g/cm^3, which is the minimum value of KAJIKAWA (1989), the geometric depths $d_1=2$ and 5 mm in Fig. 6, respectively, become to $d_1=5$ and 12.5 mm. These values are consistent with the observed geometric depth.

On the other hand, soot concentration of 0.1 ppmw with internal mixture in both snow layers leads to good agreement between theoretical and observed spectral albedos. The Arctic background concentration of snow impurities ranges from 0.005 to 0.045 ppmw (WARREN and CLARKE, 1986). Our value 0.1 ppmw is twice the highest value of WARREN and CLARKE (1986). Since our observation site was close to Barrow town, there is a possibility that the snow was polluted by locally emitted soot. Dust concentrations of 2 ppmw in the first layer and 1 ppmw in the second layer are consistent with the measured results obtained by using Nuclepore filters.

5. Summary

Spectral albedo observation was carried out on the snow field at Barrow, Alaska in April, 1997 and compared with the theoretical calculations made by a multiple scattering radiative transfer model for the atmosphere-snow system using the snow physical parameters observed by snow pit work. Optically effective snow grain size is on the order of branch size for new snow of dendrites, but is not of crystal size. Snow impurities reduce the albedo in the visible and a part of the near infrared. The observed albedo reduction in these regions is explained by the theoretical model for snow contaminated by an internal mixture of soot and external mixture of dust, where a small amount of highly absorptive material such as soot contributes to the albedo reduction in these regions and a large amount of weakly absorptive material such as dust contributes to the gross concentration of snow impurities. The soot concentration estimated by the comparison between the theoretically calculated and the observed spectral snow albedo is 0.1 ppmw. This value is higher than the Arctic background level of 0.005 to 0.045 ppmw observed by WARREN and CLARKE (1986). Since our observation site is close to Barrow town, there is a possibility that the snow was polluted by the local emission of soot. An optical method such as that by the CLARKE (1982a, b) may have to be introduced to clarify the concentration ratio of soot and dust for snow impurities on Nuclepore filters. Snow layer structure is important for the spectral albedo at the wavelengths $1.0<\lambda<1.35$ μm. We obtained good agreement between the theoretical and observed spectral albedos using a two-snow layer model based on the assumption that the density of new surface snow is 0.02 g/cm^3. This is the low-

est density known for new snow.

Acknowledgments

We are indebted to Mr. Y. NAKAJIMA and Miss Y. TSURUGA of RESTEC (Remote Sensing Technology Center), and Mr. Y. SARUYA for their logistic support. We also thank Mr. D. ENDRES and Mr. M. GAYLORD of NOAA/CMDL (National Oceanic and Atmospheric Administration/Climate Monitoring and Diagnostic Laboratory), Dr. G. W. SHEEHAN of UIC/NARL (Ukpeagvik Inupiat Corporation/Naval Arctic Research Laboratory) for their help in this field experiment. Discussions with Drs. K. STAMNES, M. JEFFRIES, A.J. ALKEZWEENY and S.-I. AKASOFU of GI/UAF (Geophysical Institute/University of Alaska Fairbanks) were fruitful for this study. This work has been done as part of the ADEOS Field Campaign supported by NASDA (National Space Development Agency of Japan).

References

AFGL (1985): Handbook of geophysics and the space environment. Air Force Geophysics Laboratory, Hanscom. MA.

AOKI, Te., AOKI, Ta. and FUKABORI, M. (1997): Approximations for phase function in calculating the spectral albedo of snow surface with multiple scattering. Pap. Meteorol. Geophys., **47**, 141–156.

AOKI, Te., AOKI, Ta., FUKABORI, M. and UCHIYAMA, A. (1999): Numerical simulation of the atmospheric effects on snow albedo with a multiple scattering radiative transfer model for the atmosphere-snow system. submitted to J. Meteorol. Soc. Jpn.

CLARKE, A. D. (1982a): Integrating sandwich: A new method of measurement of the light absorption coefficient for atmospheric particles. Appl. Opt., **21**, 3011–3020.

CLARKE, A. D. (1982b): Effect of filter internal reflection coefficient on light absorption measurements made using the integrating plate method. Appl. Opt., **21**, 3021–3031.

CHÝLEK, P., RAMASWAMY, V. and SRIVASTAVA, V. (1983): Albedo of soot-contaminated snow. J. Geophys. Res., **88**, 10837–10843.

DEIRMENDJIAN, D. (1964): Scattering and polarization properties of water clouds and hazes in the visible and infrared. Appl. Opt., **3**, 187–202.

GRENFELL, T. C. and WARREN, S. G. (1994): Reflection of solar radiation by the Antarctic snow surface at ultraviolet, visible and near-infrared wavelengths. J. Geophys. Res., **99**, 18669–18684.

KAJIKAWA, M. (1989): Relation between new snow density and shape of snow crystals. Seppyo (J. Jpn. Soc. Snow Ice), **51**, 178–183 (in Japanese with English abstract).

NAKAJIMA, M., KOJIMA, Y. and MORIYAMA, T. (1994): Mission overview and instrument concept of the Global Imager (GLI). SPIE Proc., **2268**, 122–129.

WARREN, S. G. and CLARKE, A. D. (1986): Soot from Arctic haze: Radiative effects on the Arctic snowpack. Glaciol. Data, **18**, 73–77.

WARREN, S. G. and WISCOMBE, W. J. (1980): A model for the spectral albedo of snow, II: Snow containing atmospheric aerosols. J. Atmos. Sci., **37**, 2734–2745.

WARREN, S. G. (1982): Optical properties of snow. Rev. Geophys. Space Phys., **20**, 67–89.

WISCOMBE, W. J. and WARREN, S. G. (1980): A model for the spectral albedo of snow, I: Pure snow. J. Atmos. Sci., **37**, 2712–2733.

(Received January 7, 1998; Revised manuscript accepted February 23, 1998)

Chapter 4

Effects of snow physical parameters on spectral albedo and bidirectional reflectance of snow surface

Effects of snow physical parameters on spectral albedo and bidirectional reflectance of snow surface

by

Teruo Aoki

Meteorological Research Institute

1-1 Nagamine, Tsukuba, Ibaraki 305-0052, Japan

Abstract. Observations of spectral albedo and bidirectional reflectance in the wavelength region of $\lambda = 0.35 - 2.5 \mu m$ were made together with snow pit work on a flat snowfield in eastern Hokkaido, Japan. The effects of snow impurities, density, layer structure, and grain size attained by in situ and laboratory measurements were taken into account in snow models for which spectral albedos were calculated using a multiple scattering model for the atmosphere-snow system. Comparisons of these theoretical albedos with measured ones suggest that the snow impurities were concentrated at the snow surface by dry fallout of atmospheric aerosols. The optically equivalent snow grain size was found to be of the order of a branch width of dendrites or of a dimension of narrower portion of broken crystals. This size was smaller than both the mean grain size and the effective grain size obtained from micrographs by image processing. The observational results for the bidirectional reflection distribution function (BRDF) normalized by the radiance at the nadir showed that the anisotropic reflection was very significant in the near infrared region especially for $\lambda > 1.4 \mu m$, while the visible normalized BRDF (NBRDF) patterns were relatively flat. Comparison of this result with two kinds of theoretical NBRDFs, where one having been calculated using single scattering parameters by Mie theory and the other using the same parameters except for Henyey-Greenstein (HG) phase function obtained from the same asymmetry factor as in Mie theory, showed that the observed NBRDF agreed with the theoretical one using HG phase function rather than with that using Mie phase function, while the albedos calculated with both phase functions agreed well with each other.

1. Introduction

Snow cover is very sensitive to a climate change and has large feedback effects on the climate system. The former is because local climate affects the phase change of ice (snow) and the latter is caused by the high albedo in the visible region. The modern radiative transfer model for the snow albedo has brought us a better understanding of the optical properties of snow in the shortwave spectral region. For example, the effects of solar zenith angle, snow grain size, impurities, snowpack thickness, and incident condition on the spectral albedo were examined by *Wiscombe and Warren* [1980] and *Warren and Wiscombe* [1980] using the delta-Eddington approximation and Mie theory. *Warren* [1982] reviewed the historical development of snow albedo modelings and snow albedo observations, and also described the possibility of remote sensing to estimate the snow physical parameters such as snow grain size and impurities. Satellite remote sensing of snow is important for the studies of climate change because of the large impact of the cryosphere on to the climate system. *Li* [1982] calculated the BRDF of snow using Mie theory and the "doubling method" and showed the anisotropic reflection property of snow. This is important for satellite remote sensing of a snow surface. *Han* [1996] developed the snow BRDF model using the discrete ordinate method and Mie theory to retrieve the surface albedo from satellite measurements in the Arctic. *Leroux et al.* [1997] and *Leroux et al.* [1999] developed the polarized BRDF model using the "doubling and adding" model together with Mie theory and ray optics, and compared the theoretical values with measurements in the principal plane at $\lambda = 1.65 \mu m$. They demonstrated that the snow grain shape strongly affects the BRDF in the near infrared region and that hexagonal particles rather than spherical particles give a better agreement with measurements. *Leroux and Fily* [1998] developed the BRDF model including the effect of sastrugi with regularly spaced identical rectangular protrusions. *Aoki et al.* [1999] examined the atmospheric effects, such as atmospheric molecules, absorptive gases, aerosols, and clouds, on the spectral and spectrally integrated snow albedos at the surface and at the top of the atmosphere. Thus, the snow albedo models have been incorporated into the atmosphere-snow system and have become applicable to the remote sensing of a snow surface with BRDF properties being taken into consideration.

In order to study the optical properties of snow, it is necessary to make spectral measurements of snow as well as to apply theoretical approaches. *Liljequist* [1956] have observed the albedos in four visible bands using a photoelectric cell and color filters, and reported that the maximum albedo was 0.97 in the band of $\lambda = 0.52\mu m$. Measurements of albedo with higher spectral resolution have been made by *Grenfell and Maykut* [1977] for $\lambda = 0.4 - 1.0\mu m$ using a prism spectrometer on ice and snow in the Arctic sea. They demonstrated an effect of the aging of snow on albedo and that the maximum albedo of dry snow was in the range of $\lambda = 0.4 - 0.6\mu m$. *Kuhn and Siogas* [1978] reported results on spectral albedo for a wider spectral range of $\lambda = 0.39 - 1.55\mu m$ for different types of snow in the Antarctic using a spectrometer. The visible albedos observed by *Grenfell and Maykut* [1977] and *Kuhn and Siogas* [1978] were too low compared to the theoretically predicted ones for pure snow in the polar region. *O'Brien and Koh* [1981] observed the shallow snow reflectance in the six near infrared bands from $\lambda = 0.81$ to $1.80\mu m$ using a radiometer equipped with bandpass filters. They determined the snow grain size through image processing for replicated snow samples. Since this was actually the size of snow aggregates, the theoretically predicted grain size of new snow as estimated from the values of the near infrared reflectance was much smaller than that estimated on the basis of image processing. Spectral albedo measurements for a wide solar spectrum range ($\lambda = 0.38 - 2.45\mu m$) have been made by *Grenfell et al.* [1981] on a snowfield in the Cascade Mountains in the USA using the spectrometer described by *Grenfell* [1981]. They examined the effects of snow grain size and impurities on the spectral albedo for a wide range of snow life-time from new snow to granular snow. *Grenfell and Perovich* [1984] observed spectral albedos for different types of sea ice in the Arctic sea. They concluded that the variation in albedos is due primarily to differences in vapor bubble density, crystal structure, and free water content of the upper layers of the ice. *Warren et al.* [1986] observed the spectral albedo for $\lambda = 0.3 - 2.5\mu m$ in Antarctica using two kinds of spectrometers including the type described by *Grenfell* [1981] and obtained a high value (close to unity) at visible wavelengths, as was theoretically predicted for pure snow. However, in the near infrared region, the observed albedo were higher than those predicted for

homogeneous snow, suggesting that the snow surface was covered by smaller snow grains. *Grenfell et al.* [1994] observed spectral albedos on an Antarctic snowfield under cloudy conditions which showed a good agreement with the theoretical ones calculated by means of a two-layer snow model. On the other hand, some discrepancies remained at the near infrared wavelengths under a clear sky. The reason for these discrepancies was not yet realized although they quoted these possibilities: underestimation of snow grain size; inaccurate correction of the instrument; and a fault in the model. *Sergent et al.* [1998] showed the dependency of spectral hemispherical-directional reflectance on four types of snow in the region of $\lambda = 0.9 - 1.45 \mu m$ in a cold laboratory. *Aoki et al.* [1998] examined the spectral albedos for $\lambda = 0.35 - 2.5 \mu m$ using a grating spectrometer on a snowfield at Barrow, Alaska under a cloudy condition, and demonstrated that the optically equivalent grain size (although they originally used "optically effective grain size", we will use this term to avoid any confusion with "effective radius" used for the size distribution) is of the order of the branch width of dendrites for new snow.

Most measurements mentioned above were made under cloudy conditions. However, it is necessary to examine the optical properties of snow under a clear sky in preparation for the satellite remote sensing of snow using an optical sensor. The measurement of spectral albedos under clear conditions is very difficult due to the following three reasons [*Warren et al.*, 1986]: The incident radiation is primarily a direct solar beam while the upward radiation is diffuse. (1) A little deviation of the level setting of the instrument causes an error. (2) The deviation from the so-called "cosine property" of the incident angular sensitivity of the instrument must be corrected precisely. This correction must be applied to the diffuse component as well as to the direct component, where the correction factor generally depends on the wavelength. (3) Even a gentle slope of the snow surface can cause the snow albedo to be computed erroneously if not accounted for. In general, an optically thin cosine collector that measures transmitted light has an incident angle dependence which deviates much from the perfect cosine property. Although this deviation would become small for an optically thick cosine collector, the transmittance becomes degraded as the thickness increases. This causes a poor signal to noise ratio (SNR).

Therefore, for the accurate spectral albedo measurement under a clear sky, the following are required: (1) introduction of a measurement technique with less systematic errors; (2) appropriate correction on the measured spectrum; and (3) careful selection of the snow surface on the observation site. We have obtained the spectral albedo under a clear sky by means of an observation system using a white reference standard together with correction for errors due to the observation system. These albedos were compared with the theoretically calculated ones, and the effects of snow physical parameters on the spectral albedo were investigated.

BRDF observation of a snow surface is very important for satellite remote sensing of a snow surface or of the atmosphere above a snow surface because of the anisotropic feature of snow reflectance. The early BRDF observations of snow surfaces were made for broad spectral regions on the snowfield [*Salomonson and Marlatt*, 1968; *Kuhn*, 1974; *Dirmhirn and Eaton*, 1975] and in the cold laboratory [*O'Brien and Munis*, 1975; *O'Brien*, 1977]. These studies showed the anisotropic reflection properties of snow. *Kuhn and Siogas* [1978] observed the monochromatic BRDF at $\lambda = 0.45\mu m$ at the South Pole in Antarctica, and reported the effect of sastrugi. *Taylor and Stowe* [1984a, b] demonstrated the basic features of BRDF at the top of the atmosphere for snow, cloud, land, and ocean with NIMBUS-7 ERB data. *Kuhn* [1985] examined the BRDF at $\lambda = 0.45$, 0.514, 0.75, and $1.0\mu m$ under specific geometric conditions at several Antarctic sites and an alpine snow surface. *Steffen* [1987] demonstrated the effects of snow grain size and snow type on BRDF properties from measurements using an instrument with a bandpass filter of $\lambda = 0.4 - 0.5\mu m$ in the Tienshan Mountains of China. *Brandt et al.* [1991] advanced Kuhn's work and showed the effects of the direction of sastrugi on the BRDF at $\lambda = 0.9\mu m$ as obtained from measurements at the South Pole in Antarctica taking advantage of the constant solar zenith angle over the course of a day. *Carlson and Arakelian* [1993] reported that the most anisotropic reflection in the principal plane was observed at $\lambda = 2.0\mu m$ as determined from reflection data from 0.5 to $2.3\mu m$ at Vostok in Antarctica. *Grenfell et al.* [1994] showed the BRDF pattern averaged over all Sun-sastrugi azimuth angles at $\lambda = 0.9\mu m$ at the South Pole in Antarctica. *Steffen* [1997] made the same observation as *Steffen* [1987] in Greenland and showed the BRDF patterns for several

geometric conditions. *Warren et al.* [1998] studied the effect of surface roughness on the BRDF at $\lambda = 0.6$, 0.66, and $0.9\,\mu m$ observed at the South Pole in Antarctica from the point of view of satellite remote sensing. Thus, BRDF observations have been made for some extent of snow conditions, wavelengths, and geometry. However, since natural snow surface conditions show wide variations, BRDF observations are required under various snow conditions with narrow spectral resolution in a wider spectral range and under various geometric conditions. On the other hand, it may be said that more theoretical studies on BRDF of snow are still required. For example, the BRDF is very sensitive to snow grain shape in the near infrared region. Thus, we have to investigate what kind of phase function is suitable for BRDF calculation. It is not clear if the hexagonal ice plate shown by *Leroux et al.* [1999] is applicable to all snow type. For such subjects, it is necessary to compare the measured BRDFs of snow under various conditions with the theoretically calculated ones.

The first objective of this study is to investigate the effects of snow physical parameters (snow grain size, impurities, and layer structure) on spectral albedo under clear conditions using the spectral data, snow pit work data, and a radiative transfer model. The second objective is to investigate the BRDF properties of snow and obtain the basic knowledge required to develop an accurate BRDF model. This work is linked with the satellite remote sensing program which is to retrieve snow grain size and snow impurities using data obtained by means of an optical sensor GLI (Global Imager) mounted on the Japanese satellite ADEOS-II (Advanced Earth Observing Satellite-II) that will be launched in 2000 [*Nakajima et al.*, 1998]. Therefore, the BRDF analysis was done for 6 selected wavelengths in the visible and the near infrared regions from among the GLI's 36 channels.

2. Observation conditions

Spectral albedo observations with snow pit work were made on February 22 - 25, 1998 at three sites on a snowfield around Kitami in eastern Hokkaido, Japan (Figure 1, Table 1). These observation sites were seasonally snow covered flat farms, where there were no shadows caused by surface roughness, although slight undulation was seen. The spectral

albedo data were selected under the conditions where the solar zenith angle was close to 53° which was the value at local solar noon, and the snow surface was illuminated by a direct solar beam. The sky conditions were clear except on February 22 as shown in Table 1. A new snowfall was observed on February 20 with a depth of about $10cm$ and on February 21 with a depth of less than $1cm$. Snow conditions at the snow surface changed from new snow to faceted crystals or granular snow during the observation period as shown in Figure 2, and those in the lower part were depth hoar throughout this period. Snow grain size (radius) was estimated using a handheld lens together with micrographs to provide the size distribution. In situ measurement with a handheld lens gave two kinds of dimensions of grain size; one was a half the length of the major axis of crystals or dendrites (r_1) and the other was a half the branch width of dendrites or a half the dimension of narrower portion of broken crystals (r_2). Figure 3 shows micrographs for the surface snow (Figures 3a - 3d) from February 22 to 25 and those for $5cm$ - and $20cm$ -depths on February 23 (Figures 3e - 3f). These micrographs together with other pictures were used to estimate the size distribution of circle-equivalent radius for the projected grains by means of the image processing software "Image Hyper II" made by Inter Quest Inc. (Japan). The procedure of this image processing was as follows: The digitized image of each micrograph of snow grains was converted to binary tone with an adequate threshold level. Highly aggregated grains were masked automatically. For the remaining grains, the projected area was directly measured for independent grains. In case of a few grains attached to each other, they were separated into independent grains by estimating the area of overlapping between individual grains by means of a sphere-separating algorithm. The circle-equivalent radius was calculated from the projected area, and the mean radius ($\bar{r}_{image}$) and the effective radius (r_{image}^{eff}: area-weighted mean radius, after *Hansen and Travis*, 1974) were obtained. *Grenfell et al.* [1994] and *Grenfell and Warren* [1999] argued that spheres of equal volume-to-area-ratio (V/A) are more appropriate as the optically equivalent snow grain size. Unfortunately, we could not estimate the radius of the equal-V/A sphere accurately for irregular snow grains on our micrographs. The optically equivalent snow grain size will be discussed using the roughly estimated radius of the equal-V/A sphere in subsection 6.3. The resultant

size distribution is shown in Figure 4. The size distribution of the snow grain radius was wider on later days than early days, and the mean radius $\bar{r}_{image}$ was also larger on later days. The values of $\bar{r}_{image}$ were closer to r_2 than r_1 at the snow surface in Figure 2 and were close to the highest values in the range of r_2. From Figures 2 - 4 we see that the surface grain size increased with the lapse of time, and it was generally smaller at the surface than in the deeper layers. These facts are due mainly to the formation of faceted crystals or depth hoar. The snow density around the surface was lowest on February 22 and became higher on later days. The snow impurities (water-dissolved solid particles in the snowpack) were filtered within a day using Nuclepore filters with a diameter of $25mm$ and the pore size of $0.2\mu m$, after melting the snow samples of the surface layer $(0-5cm)$ and of the sub-surface layer $(5-10cm)$. The concentrations of impurities were estimated by direct measurements of the weight of the Nuclepore filters, before and after filtering, using a balance.

3. Instrumentation

The spectral albedo was observed using a grating spectrometer, "FieldSpec FR", made by ASD Inc. (USA). The scanning spectral range of this instrument was $0.35-2.5\mu m$ with the spectral resolution of 3 nm for $\lambda = 0.35-1.0\mu m$ and 10 nm for $\lambda = 1.0-2.5\mu m$. The scanning time was one second with a sampling interval of 1 nm for the full spectral range. The detectors were one dimensional Si photodiode CCDs for $\lambda = 0.35-1.0\mu m$ and two different types of InGaAs photodiodes for $\lambda = 1.0-1.8\mu m$ and $\lambda = 1.8-2.5\mu m$. To obtain the albedo, measurements of downward and upward fluxes were necessary. However, it was very difficult to measure the downward flux accurately under clear conditions as stated by *Warren et al.* [1986]. Thus, we made an albedo observation system (Figure 5) using a white reference standard (WRS) of $BaSO_4$ "SRT-99" made by Labsphere Inc. (USA). The WRS was attached horizontally to the tip of a pipe (black part in Figure 5 bottom) stretching from the mount set on the top of a tripod. The length of the pipe was $0.9m$. The downward flux was observed by directing the optical fiber tip of the spectrometer downward to the upper surface of WRS. In the case of the upward flux observation, an arm holding the optical fiber tip (hatched parts in

Figure 5 bottom; we will call it the "optical fiber arm" hereafter) was turned by 180° around the pipe. The optical fiber had a conical field of view (FOV) subtending a full angle of approximately 25°. The distance of WRS from the snow surface was about $0.3m$.

This method has some advantages as follows: (1) the level of WRS can be set accurately by means of a spirit level and does not change throughout the measurements; (2) it is not necessary to know the absolute reflectance of WRS for albedo measurements; and (3) the cosine property of reflection is generally better than that of a cosine collector. The deviation from the perfect cosine behavior of the cosine collector used by *Grenfell et al.* [1994] was, at maximum, 10 % at the incident angle of 60° and 40 % for 80°, and its wavelength dependence was also very large. In our case, it was about 8 % at the incident angle of 60° and about 20 % for 80° with slight spectral dependence (Figure 6a). Our system, however, underestimated the fluxes due to the shading by the optical fiber arm. These effects were corrected as will be shown in the next section. The spectral albedo for one snow surface was calculated by averaging five spectral albedos obtained from five pairs of measurements for downward and upward (snow reflected) solar fluxes. In general, it takes less than a few minutes to measure these quantities under clear conditions. However, on February 22 it took 16 minutes due to the presence of broken clouds. The standard deviation for these five observed albedos was also calculated to check the data quality.

4. Corrections for radiant flux and albedo

Two kinds of effects should have been taken into account to obtain the radiant flux with our instrument: one was the deviation from the cosine property of WRS and the other was the influence of shading by the optical fiber arm. The former was calibrated in a laboratory (Figure 6a), where WRS was illuminated from different incident angles by a direct solar (parallel) beam led by the mirror of a heliostat. In this calibration there were no data for the incident angles less than 20° due to the shadow of the optical fiber tip on WRS. Since the deviation from the cosine property would be very small at small incident angles, we assumed that the reflectance of WRS for the incident angles less than 20° followed the cosine property.

Figure 6a shows that the spectral dependence of the reflection property of WRS was very small. In the atmospheric absorption bands, the SNRs of measured spectra in this calibration were not very good due to the use of direct solar radiation. Thus, we used the calibration curve at $\lambda = 0.52\mu m$ with high SNR for all wavelengths. The influence of shading by the optical fiber arm is also shown in Figure 6a, where the azimuthally integrated shading fraction is plotted for each incident angle viewed from the center of the field of view of the optical fiber on WRS.

Figure 6a shows that our observation system would have underestimated the radiant flux due to the two factors mentioned above. We now define a factor $f(\theta,\phi)$ as the ratio of the observed value to the true one for the radiant flux coming only from the incident angle θ and the azimuth angle ϕ. For the incidence of isotropic diffuse radiation, the ratio of observed radiant flux to the true one f_{diff} is given by

$$f_{diff} = 2\int_0^{\pi/2} \bar{f}(\theta)\sin\theta\cos\theta d\theta, \tag{1}$$

where $\bar{f}(\theta)$ is the azimuthally integrated value of $f(\theta,\phi)$ and is given by

$$\bar{f}(\theta) = \frac{1}{2\pi}\int_0^{2\pi} f(\theta,\phi)d\phi. \tag{2}$$

For the direct solar beam, the ratio of observed radiant flux to the true one is expressed by $f_{dir}(\theta,\phi) = f(\theta = \theta_0, \phi = \phi_0)$, where θ_0 and ϕ_0 are the solar zenith and solar azimuth angles, respectively. Although the upward flux and the diffuse component in the downward flux are anisotropic in the strict sense, we assumed these fluxes are isotropic here. In our system, the ordinate in Figure 6a corresponds to $\bar{f}(\theta)$ for WRS and $1 - \bar{f}(\theta)$ for shading by the optical fiber arm. In the case of WRS, the ϕ dependence of $f(\theta,\phi)$ is so small that we assumed $\bar{f}(\theta) = f(\theta)$. For the direct solar beam, we also assumed $f_{dir}^{WRS}(\theta_0,\phi_0) = f(\theta_0)$. Putting the data of Figure 6a into equation (1), $f_{diff}^{WRS} = 0.946$ and $f_{diff}^{arm} = 0.934$ are obtained respectively for WRS and the shading by the optical fiber arm. The correction of WRS should be made for

both the direct and diffuse components in downward solar flux, and the correction coefficient $C_{Fdn}^{WRS}(\theta_0,\lambda)$ for downward flux is given by

$$C_{Fdn}^{WRS}(\theta_0,\lambda)=\frac{r_{dir}(\theta_0,\lambda)}{f_{dir}^{WRS}(\theta_0)}+\frac{r_{diff}(\theta_0,\lambda)}{f_{diff}^{WRS}}, \tag{3}$$

where $f_{dir}^{WRS}(\theta_0)$ is obtained from the data for WRS in Figure 6a, and $r_{dir}(\theta_0,\lambda)$ and $r_{diff}(\theta_0,\lambda)$ are the fractions of direct and diffuse components in downward total flux (*i.e.*, $r_{diff}=1-r_{dir}$), respectively. We calculated these fractions using the radiative transfer model for the atmosphere-snow system which will be described in the next section. The calculated values of r_{dir} and r_{diff} for February 23, 1998 ($\theta_0=56.8°$) are shown on the right ordinate in Figure 6b. Since the optical fiber arm held the fiber tip on the opposite side from the Sun and did not affect the measurement of direct solar radiation for $\theta_0>20°$, only the diffuse component should be corrected in the downward solar flux and the correction coefficient $C_{Fdn}^{arm}(\theta_0,\lambda)$ is given by

$$C_{Fdn}^{arm}(\theta_0,\lambda)=\frac{r_{diff}(\theta_0,\lambda)}{f_{diff}^{arm}}. \tag{4}$$

For upward solar flux the correction coefficient C_{Fup}^{WRS} for WRS and C_{Fup}^{arm} for the optical fiber arm are simply given by

$$C_{Fup}^{WRS}=\frac{1}{f_{diff}^{WRS}} \tag{5}$$

and

$$C_{Fup}^{arm}=\frac{1}{f_{diff}^{arm}}. \tag{6}$$

The total correction coefficients for downward and upward solar fluxes are given by $C_{Fdn}^{WRS}(\theta_0,\lambda)C_{Fdn}^{arm}(\theta_0,\lambda)$ and $C_{Fup}^{WRS}C_{Fup}^{arm}$, respectively, and thus the resultant net correction for albedo is expressed by

$$C_{albedo}(\theta_0,\lambda) = \frac{C_{Fup}^{WRS} C_{Fup}^{arm}}{C_{Fdn}^{WRS}(\theta_0,\lambda) C_{Fdn}^{arm}(\theta_0,\lambda)}. \quad (7)$$

The correction coefficients for February 23 are shown on the left ordinate in Figure 6b. In our system, the correction coefficient for upward flux was larger than that for downward flux. However, for the calculation of albedo they canceled out each other in part and the resultant net correction was less than 1.06.

5. Radiative transfer model

5.1. Basic features of the radiative transfer model

A multiple scattering radiative transfer model for the atmosphere-snow system was used for calculating the fractions of direct and diffuse components in downward solar flux mentioned in the previous section and was used to compare the observed spectral albedo of snow with the theoretical one. In the model, snow grains were assumed to be mutually independent ice particles and radiative transfer was treated in the same manner as in the usual multiple scattering model in an atmosphere containing aerosols or cloud particles. Radiative transfer calculations were based on Mie theory for single scattering and the "doubling and adding" method for multiple scattering omitting polarization. The details of this model have been described by *Aoki et al.* [1999]. However, in the present study the imaginary part of the complex index of refraction of ice revised by *Kou et al.* [1993] was used only for $\lambda \geq 1.45\mu m$. In the calculation for the fractions of direct and diffuse components in downward solar flux, we assumed the model atmosphere of Midlatitude Winter [*Anderson et al.*, 1986] together with the Rural model for aerosols [*AFGL*, 1985]. The aerosol optical depth was assumed to be 0.1 at $\lambda = 0.5\mu m$ from the sunphotometer measurements in winter from 1993 to 1998 [*JMA*, 1999; *JMA*, unpublished, 1999] at Ryori Station (39° 02' N, 141° 50' E, 230 m), which was a background monitoring station nearest to our observation sites. For the calculation of spectral albedo for the comparison with the observed one, a simplified model atmosphere was employed

in the radiative transfer model for the atmosphere-snow system. This was because the effects of gaseous absorption and aerosols with an optical depth of 0.1 on the spectral snow albedo were both small enough for $\theta_0 \leq 63.1°$ [*Aoki et al.*, 1999], at which our observation was made, so we assumed the aerosol-free Rayleigh atmosphere without gaseous absorption.

The BRDFs of the snow surface were calculated at 6 wavelengths (0.52, 0.71, 1.05, 1.24, 1.64, and 2.21μm) selected from among the GLI's 36 channels using the radiance model for the atmosphere-snow system extended from the flux model mentioned above. Since there is no strong gaseous absorption at the wavelengths concerned, we assumed the Rayleigh atmosphere including aerosols mentioned above without the gaseous absorption for BRDF calculation. The adopted definition of BRDF is the commonly used one given by

$$BRDF_\lambda(\theta_v, \theta_0, \Delta\phi) = \frac{I_\lambda(\theta_v, \theta_0, \Delta\phi)}{F_\lambda(\theta_0)}, \tag{8}$$

where θ_v and θ_0 are the viewing angle and the incident zenith angle of direct solar beam, respectively, $\Delta\phi$ is the relative azimuth angle of the viewing direction from the solar direction, $I_\lambda(\theta_v, \theta_0, \Delta\phi)$ is the reflected radiance from the snow surface, and $F_\lambda(\theta_0)$ is the downward solar flux.

5.2. Optical characteristics of snow impurities

Warren and Wiscombe [1980] demonstrated that snow impurities reduce the spectral snow albedo in the visible region and have no effect on spectral albedo for $\lambda > 0.9\mu m$ where ice itself becomes a strong absorber. The reduction of visible albedo is different depending on the mixing type, such as external and internal mixtures [*Chylek et al.*, 1983]. To examine the mixing type, we took scanning electron microscope (SEM) photographs of snow impurities collected on the Nuclepore filters (Figure 7). Since these particles comprise a large variety in terms of size and shape, it is considered that a large proportion of them were materials of soil origin. A small amount of spherical particles (maybe minerals) or particles which looked like to be coagulated (maybe soot) were also recognized. These morphological characteristics suggest

that they were anthropogenic aerosols produced by fuel burning. The concentration of these impurities at the snow surface increased with time as shown in Figure 2. In view of these observations, most of the snow impurities were considered to be contained in snow as an external mixture.

When the effect of snow impurities on spectral albedo is simulated as an external mixture, it is necessary to calculate the single scattering parameters for the particles of impurities. For such calculation Mie theory is used, where the particle size distribution and the complex refractive index of impurities are required. To obtain the size distribution of the impurities from the SEM pictures, a sample with a low concentration of impurities on the Nuclepore filter was required. However, since some particles in our collected samples were overlapped each other on the Nuclepore filter, it was difficult to estimate the size distribution accurately. We determined only the mean particle radius as $1.0\mu m$ from the SEM pictures including Figure 7 and assumed a standard size distribution of the gamma-type [*Hansen*, 1971] with an effective variance of 0.125. The imaginary part of the refractive index of the impurities is the most important factor which affects albedo reduction and it is obtained from the absorption coefficient by the following relation:

$$m_{im}(\lambda) = \frac{\lambda \beta_a(\lambda)}{4\pi}, \tag{9}$$

where $m_{im}(\lambda)$ is the imaginary part of the refractive index and $\beta_a(\lambda)$ is the volume absorption coefficient. For measurements of the absorption coefficient, many techniques have been developed [*Clarke*, 1982]. *Lindberg and Laude* [1974] measured $\beta_a(\lambda)$ from the diffuse reflectance of impurities mixed with $BaSO_4$ diluting agent based on the Kubelka and Munk theory. Since this technique requires a sample of several milligrams and it makes the sample unsuitable for the use in SEM analysis after the measurement, this method was not applied to our samples. *Clarke* [1982] developed the integrating sandwich (IS) method in which a Nuclepore filter loaded with the impurities sandwiched between two high-reflectance diffusing wafers, and the total transmittance is measured. This method can be applied only to well

scattered samples and was not applicable to our samples due to the overlapping of particles on the filter. We employed the integrating plate (IP) method [*Lin et al.*, 1973; *Clarke*, 1982] to measure $\beta_a(\lambda)$ from our samples collected on the Nuclepore filters. In this method the diffuse transmittance of the Nuclepore filter loaded with the sample is measured. Since our samples was somewhat thick for this method, multiple scattering by particles in the sample might have caused overestimation of $\beta_a(\lambda)$. Furthermore, according to *Clarke* [1982], the value of $\beta_a(\lambda)$ obtained by the IP method could be overestimated due to the internal reflection of the Nuclepore filter and multiple reflection between the Nuclepore filter and the substrate's surface (opal glass diffuser). To eliminate the third influence we used an integrating sphere as a light source and made the illumination diffuse without using an opal glass diffuser. The value of $\beta_a(\lambda)$ is obtained from the spectral measurement for net transmittance of impurities $T(\lambda)$ as

$$\beta_a(\lambda) = -\frac{1}{d}\ln(T(\lambda)), \tag{10}$$

where d is the depth of the layer of impurities on the Nuclepore filter. The value of d is estimated from the weight w of the impurities, their density ρ_i and the filtration area S_f ($= 2.27cm^2$) of the Nuclepore filter by the relation

$$d = \frac{w}{\rho_i S_f}. \tag{11}$$

We used the values measured with balance for w as mentioned in section 2 and took the typical value of soil $2.0g/cm^3$ for ρ_i [*Japanese National Astronomical Observatory*, 1999]. We thereby obtained the imaginary part of the refractive index of snow impurities, $m_{im}(\lambda)$, as shown on the left scale in Figure 8 for sample 980223A1. The values of $m_{im}(\lambda)$ for all samples from February 22 to 25 lie in the range $1.4\times10^{-2} \sim 2.7\times10^{-2}$ at $\lambda = 0.5\mu m$ and $4.1\times10^{-2} \sim 7.2\times10^{-2}$ at $\lambda = 2.0\mu m$. *Warren and Wiscombe* [1980] reviewed the measurements of snow impurities and showed that the values of the imaginary part of the

refractive index in the visible region are of the order of 10^{-2}. But those for pure substances generally vary widely over a large range of wavelength and are different from each other [*Bohren and Huffman* 1983]. Figure 8 also shows the values of $m_{im}(\lambda)$ for soot [*AFGL*, 1985], Dust-Like aerosol [*AFGL*, 1985], and ice [*Warren*, 1984; *Kou et al.*, 1993] on the same scale just for comparison. Our estimated values of $m_{im}(\lambda)$ were somewhat higher than the values for snow impurities reviewed by *Warren and Wiscombe* [1980], and for Dust-Like aerosol compiled by *AFGL* [1985]. This may owe to three possible reasons: (1) the overestimation of $\beta_a(\lambda)$ due to the multiple scattering by the overlapped particles of impurities; (2) the overestimation of $\beta_a(\lambda)$ due to the internal reflection in the Nuclepore filter as described by *Clarke* [1982]; and (3) the containing of soot in our samples as mentioned in the first paragraph of this subsection. Since the effect of the second reason is evaluated to be as much as 30% [*Clarke*, 1982], the first or the third one could be the main reason. Since the measured values of $m_{im}(\lambda)$ were scattered in the regions of $\lambda < 0.4\mu m$ and $\lambda > 1.8\mu m$ due to low SNR (see Figure 8), the fitted curve of $m_{im}(\lambda)$ obtained by means of a cubic equation of wavelength was used in calculation of the spectral albedo of the snow surface. We obtained the curves of $m_{im}(\lambda)$ for all of our samples. On the other hand, the real part of the refractive index, $m_{re}(\lambda)$, is generally measured by the immersion oil technique [*Patterson et al.*, 1977], in which the sample is immersed in an oil whose indices of refraction and dispersion are known. This technique also makes the sample unsuitable for the use in SEM analysis after the measurement. We therefore assumed the value of $m_{re}(\lambda)$ for Dust-Like aerosol compiled by *AFGL* [1985] as shown on the right scale in Figure 8.

6. Effects of snow physical parameters on spectral albedo

6.1. Snow layer structure

The spectral albedo observed on February 23 was compared with the theoretical values as shown in Figure 9 where the observed and theoretical spectral albedos are shown on the left scale, and the standard deviation of observed albedo is on the right scale. At the wavelengths where a large standard deviation was observed, the energy of the downward solar flux was

relatively weak compared with the sensitivity of the detector of our spectrometer. This is due mainly to the low sensitivity of the detector itself ($\lambda \sim 0.95\mu m$ and $\lambda > 1.8\mu m$) and the energy of the downward solar flux was low because of the atmospheric absorption bands ($\lambda \sim 0.4$, 1.4, 1.9, and $2.5\mu m$). Except for these wavelengths, low values of standard deviation less than 0.005 were obtained. The theoretical spectral albedos were calculated for four kinds of snow models (Figure 10), in which layer thickness, effective snow grain radius (r_{eff}), and the concentration of impurities (s) were varied.

Model-1 consists of a pure snow layer with $r_{eff} = 55\mu m$ and a semi-infinite snow depth. The grain size was determined from a comparison between observed spectral albedo and the theoretical one in the region of $\lambda > 1.4\mu m$. This was based on the theoretical calculation by *Warren and Wiscombe* [1980], in which there are no significant effects of impurities on spectral albedo in this wavelength region because of the high value of $m_{im}(\lambda)$ for the ice and its much larger volume fraction compared with the impurities. The theoretical albedo agrees with the observed one very well in this wavelength region. The value of $r_{eff} = 55\mu m$ agrees with r_2 better than r_1, where r_1 is a half the length of the major axis of crystals or dendrites, and r_2 is a half the branch width of dendrites or a half the dimension of narrower portion of broken crystals as shown in Figure 2. The relation between the near infrared albedo and snow grain size will be further discussed in subsection 6.3. In the region of $\lambda < 1.4\mu m$, the observed albedo is lower than the theoretical one. Some situations in parameters such as total snow depth and vertical profiles of snow grain size and impurities could be considered as the reasons for this discrepancy between the albedos. To examine this, the observed albedo was compared with the theoretical one calculated for Model-2 without impurities, in which the snow grain size, depth, and density were determined from the results of snow pit work. The observed snow grain size (particularly r_2) varies drastically near the surface (see Figure 2b). To simulate this condition, in Model-2 we assumed three pure layers with $r_{eff} = 55\mu m$ $(0-1cm)$, $110\mu m$ $(1-5cm)$, and $1000\mu m$ $(5-30cm)$. In the second layer, the value of $r_{eff} = 110\mu m$ was assumed to be twice that of $r_{eff} = 55\mu m$ in the top layer according to the measurements of r_2. For snow density the observed value $\rho = 0.16g/cm^3$ was assumed for the top layer and a

constant value $\rho = 0.2 g / cm^3$ was assumed for the two lower layers. The visible albedo is reduced in Model-2, but is not sufficiently low. This is due to the snow impurities as we have mentioned above. The measured concentration of impurities was $4.0 ppmw$ in the layer of $0 - 5cm$ and $1.2 ppmw$ in the layer of $5 - 10cm$. We made Model-3 which was the same as Model-2, except for the impurities whose concentration was assumed to be $s = 4 ppmw$ for the top two layers and $s = 1 ppmw$ for the bottom layer. The theoretical albedo for Model-3 is further reduced in the region of $\lambda < 1.0 \mu m$, but does not yet correspond to the observed one. Now we considered that the snow impurities might have been concentrated at the surface, and Model-4 was made in which the concentration of impurities was assumed to be $s = 18 ppmw$ for the top $0 - 1cm$ layer and $s = 1 ppmw$ for the two lower layers. The concentration in the top layer was set so as to keep the total column amount of impurities in the layers of $0 - 5cm$ as determined from the observed value of $3.6 \mu g / cm^2$, where it was $3.7 \mu g / cm^2$ for Model-4. We can see the best agreement between the observed albedo and the theoretical one with Model-4. These results suggest that only a thin top layer rather than the whole depth of $0 - 5cm$ of snow was highly contaminated and this occurred due to dry fallout of atmospheric aerosols. This conclusion holds even if the values of the absorption coefficients of impurities were overestimated due to multiple scattering by the particles of impurities as mentioned in subsection 5.2. A small discrepancy in the albedo between observed and calculated values is noted only in the region of $1.2 < \lambda < 1.4 \mu m$. Similar results were also found from the data of the other days as will be shown in the next subsection, although the reason is not clear at this stage.

6.2. Estimation of snow impurities

Theoretical calculations of spectral albedo using snow models similar to Model-4 were performed for February 22, 24, and 25, and compared with the observations as shown in Figures 11a - 11c. The snow models assumed for these three days are shown in Figures 12a - 12c, respectively. The effective grain radius (r_{eff}) and snow density (ρ) were determined by the same method as in the previous subsection. In the case of February 22, the best agreement

is obtained using the value of s close to the measurement. However, on February 24 the value of s by which the theoretical albedo agrees with the observed one is $50ppmw$ in the layer of $0-0.5cm$. In this case the total column amount of impurities in the layer of $0-5cm$ is $5.7\mu g/cm^2$ which is somewhat larger than the measured value ($4.1\mu g/cm^2$). This result may be due to an error in the thickness of snow sampling because it is not easy to take a snow sample of the layer of $0-5cm$ precisely. In the case of February 25, a good agreement is obtained for $s = 20ppmw$ with a total column amount of impurities $5.8\mu g/cm^2$, in the layer of $0-5cm$ (the measured value was $6.0\mu g/cm^2$). From these analyses, we can delineate the daily change in snow contamination as follows. On February 22 just after the snowfalls (February 20 and February 21), the snow surface was comparatively clean and had a high visible albedo. Thereafter, snow impurities gradually became concentrated at the surface due to dry fallout of atmospheric aerosols. The measured concentration of snow impurities in the layers below $5cm$ -depth on February 22 were higher than those on the other days. Possible reasons are the difference in observation sites or an error in the thickness of snow sampling. However, even if the value of $s = 1ppmw$ is assumed for the $5-30cm$ on February 22, the spectral albedo increases, at maximum, only by 0.001 at $\lambda = 0.5\mu m$.

In the above analyses small discrepancies in albedos between observed and calculated values are still found at around $1.3\mu m$ for all cases in Figures 11a - 11c, as was found on February 23. These results suggest that a systematic error in the calculation and/or observation had been present in this work, but it has not been clarified at this stage. *Sergent et al.* [1998] discussed the optical radius (= our optically equivalent radius) determined from the measured hemispherical-directional reflectance at $\lambda = 0.99\mu m$ makes the theoretical value of the spectral hemispherical-directional reflectance agree with the measured one in a wide region of $\lambda = 0.9-1.45\mu m$. If such measurement is extended to longer wavelengths, the uncertainty in the present study would be clarified.

6.3. Snow grain size

In this subsection we will compare the optically equivalent snow grain size, that gives

the best fit to theoretical spectral albedo, with the in situ measured snow grain size and that determined from micrographs by image processing. *Grenfell et al.* [1981] noted that the observed albedo was lower than that theoretically predicted from the measured snow grain size on the basis of snow pit work, where they defined the snow grain size as 0.5 times the smallest dimension of typical particle. *O'Brien and Koh* [1981] reported that the grain size of new snow theoretically predicted from the near infrared reflectance was much smaller than that determined on the basis of image processing for replicated ice crystals. *Sergent et al.* [1998] showed that the mean convex radius (defined as the inverse of the mean curvature of the grain contour obtained by the image-analysis system) of snow grains was larger than the optical radius except for large grains, as determined from measurements of hemispherical-directional reflectance at $\lambda = 0.9 - 1.45 \mu m$ in a cold laboratory. *Aoki et al.* [1998] demonstrated that the optically equivalent grain size is of the order of the branch width of dendrites for new snow. The different relations of observed grain size to model grain size found by these different authors are most likely explained by different choices of equivalent sphere.

We examined in detail the relation between the optically equivalent snow grain size of sphere and the measured geometrical grain size. Table 2 shows the comparison of the grain radii obtained from snow pit work (r_1 and r_2), image processing ($\bar{r}_{image}$ and r_{image}^{eff}) and spectral albedo fitting in the region of $\lambda > 1.4 \mu m$ (r_{fit}). The value of r_1 is the size commonly used in glaciological measurements, with which the values of r_{fit} do not correspond. Most values of r_{fit} are in the range of r_2. That is, the optically equivalent size is of the order of a branch width of dendrites or of a dimension of narrower portion of broken crystals, just as was found by *Aoki et al.* [1998]. The values of $\bar{r}_{image}$ are 1.6-2.6 times larger than r_{fit} , and the values of r_{image}^{eff} are approximately 1.5 times larger than $\bar{r}_{image}$. Thus, both the snow grain radii estimated by image processing are not applicable as the optically equivalent grain size to our irregular snow particles. *Grenfell and Warren* [1999] showed that the scattering and absorption properties of nonspherical ice particle are represented using equal-V/A spheres from the theoretical calculations for randomly oriented infinite long cylinder of ice. Although we cannot estimate the radius of the equal-V/A sphere accurately for irregular snow grains in our

micrographs, we could roughly make an estimate of radius of the equal-V/A sphere by assuming our snow grains to be hexagonal columns and to lie along the c-axis in our micrographs. According to *Grenfell and Warren* [1999], the radius of equal-V/A sphere r_{VA} for hexagonal column is given by

$$r_{VA} = \frac{3\sqrt{3}ac}{4c + 2\sqrt{3}a}, \tag{12}$$

where a is the length of each side of the hexagon and c is the length of the column. The projected area (not a surface area) measured by image processing is $2ac$ and equals to $\pi \bar{r}_{image}^{\,2}$. We, here, need the ratio $2a / c$, that is the width / length ratio of each snow grain. This ratio increases from February 22 to 25 as shown in Figure 3. We roughly estimated the ratios $2a / c$ from our micrographs to be 1/5, 1/4, 1/3, and 1/2, respectively, from February 22 to 25. Thus, the values of r_{VA} are obtained as shown in Table 2. These values agrees with r_{fit} as discussed by *Grenfell and Warren* [1999].

The grain radius can be defined as the radius of (1) the equal-volume sphere, (2) the equal-surface-area sphere, (3) the equal-projected-area sphere (4) the equal-V/A sphere, (5) half the long dimension, or (6) half the short dimension. *Grenfell et al.* [1981] and *Aoki et al.* [1998] used the definition (6), and the analyses by image processing use the definition (3). In general, the snow grain sizes by the definitions except (4) and (6) are larger than the optically equivalent one. In the paper by *O'Brien and Koh* [1981], very small particles less than $50\,\mu m$ were not identified as replicated ice crystals and, thus, their estimated grain size for new snow as determined by image processing might have been larger than the theoretically predicted one. On the other hand, we confirmed that there was no liquid water in the network of snow grains in our observation. If water exists in the snowpack, it would act to increase the optically equivalent grain size by bonding snow grains.

7. Effects of snow physical parameters on BRDF

7.1. Observation of BRDF

The BRDF observation was carried out on the same snow surface for the albedo measurement on February 25 at Site-B of which the results were shown in the previous section. This observation was made using two types of optical heads: one was the bare optical fiber whose field of view (FOV) was 25° for full angle and the other was a foreoptics head with 1°-FOV attached to the optical fiber. The former was set up as in the case of the albedo observation system (see Figure 5) without WRS where the azimuth and zenith angles were controlled by turning the azimuth direction of the mount and the viewing direction of the optical fiber arm, respectively. The latter (foreoptics) was set to a goniostage (angle-setting device) on a tripod on the snow surface. Since the distance from the snow surface to the foreoptics was about $1.0m$, even a slight undulation of the snow surface could affect the BRDF pattern observed with the foreoptics, especially at low θ_v. On the contrary, at high θ_v the FOV of the optical fiber was too broad to measure the target accurately. We thus made a composite BRDF pattern from the measurements obtained with the optical fiber for $\theta_v \leq 70°$ and from those obtained with the foreoptics for $\theta_v \geq 80°$.

In the calculation of BRDF, it is necessary to measure $F_\lambda(\theta_0)$ as shown in equation (8). However, it was difficult to obtain its accurate value in measurement with the foreoptics and WRS because the foreoptics head was large in size ($60mm\phi \times 120mm$) compared to that of WRS ($150mm \times 150mm$) and it obstructed the light coming from the zenith direction. In many studies involving the BRDF observation, the anisotropic reflection factor $R_\lambda(\theta_v,\theta_0,\Delta\phi)$ has been used [*Taylor and Stowe*, 1984a, b; *Brandt et al.*, 1991; *Grenfell et al.*, 1994; *Warren et al.*, 1998] which is defined as

$$R_\lambda(\theta_v,\theta_0,\Delta\phi) = \frac{\pi BRDF_\lambda(\theta_v,\theta_0,\Delta\phi)}{A_\lambda(\theta_0)}, \tag{13}$$

where $A_\lambda(\theta_0)$ is the spectral albedo. The resulting $R_\lambda(\theta_v,\theta_0,\Delta\phi)$ has an average value of 1.0 over the $(\theta_v,\Delta\phi)$ hemisphere. The value of $R_\lambda(\theta_v,\theta_0,\Delta\phi)$ is expressed only by the upward radiance $I_\lambda(\theta_v,\theta_0,\Delta\phi)$ and is given by

$$R_\lambda(\theta_v,\theta_0,\Delta\phi) = \frac{\pi I_\lambda(\theta_v,\theta_0,\Delta\phi)}{\int_0^{2\pi}\int_0^{\pi/2} I_\lambda(\theta_v,\theta_0,\Delta\phi)\sin\theta\cos\theta d\theta d(\Delta\phi)}. \quad (14)$$

The merit of using $R_\lambda(\theta_v,\theta_0,\Delta\phi)$ is that it is not necessary to know the value of $F_\lambda(\theta_0)$ in equation (8). However, the complete angular measurement of $I_\lambda(\theta_v,\theta_0,\Delta\phi)$ is required and it was not obtained in the case of our observations. We therefore calculated the normalized BRDF (NBRDF) by taking into account the radiance at the nadir. The composite NBRDF pattern was also calculated from each NBRDF obtained by means of the optical fiber and the foreoptics.

Figure 13 shows the observed composite NBRDF for 6 wavelengths, where we used the display method employed previously by *Taylor and Stowe* [1984a, b] and *Warren et al.* [1998]. The anisotropic reflection property is very significant at $\lambda = 1.64$ and $2.21\mu m$, while in the visible region the NBRDF patterns are relatively flat. The reason for this was explained by *Leroux et al.* [1999] as follows: since in the visible region the single scattering albedo is close to unity due to the weak absorption of ice, the BRDF is not influenced by the single scattering parameter, and vice versa in the near infrared region. A similar result was obtained in the principal plane by *Carlson and Arakelian* [1993] in the measurement of anisotropic reflection in Antarctica. Our result was expected in view of the findings of *Warren et al.* [1998] where the BRDF pattern was found to become more anisotropic with a relatively strong forward peak for $\lambda > 0.9\mu m$, where snow is more absorptive. The maximum NBRDF is observed at $\theta_v = 85°$ in the forward scattered direction (the bottom of each map) being 2.2 at $\lambda = 0.52\mu m$ and 16.2 at $\lambda = 1.64\mu m$. In the side scattered directions (the left and right directions on each map), the NBRDF decreases to some degree with the viewing angle in the visible region and increases in the near infrared region. Observation by ADEOS II / GLI will be made only in the range $\theta_v \leq 45°$, where the NBRDF varies from 0.94 to 1.14 at $\lambda = 0.52\mu m$ and from 0.88 to 2.19 at $\lambda = 1.64\mu m$. If the appropriate correction on BRDF is not made in the satellite remote sensing, a large amount of error would be present in the retrieved snow parameter values, especially in the near infrared channels. Furthermore, even

the uncertainty of 10% in the snow reflectance at $\lambda = 0.52\mu m$ could bring the serious error for the remote sensing of snow impurities.

7.2. Theoretical calculation of BRDF and comparison with measurement

Figure 14 shows the theoretically calculated patterns of NBRDFs using two different phase functions under the same snow conditions as used in Figure 11c. The first one (left side) was calculated using the single scattering parameters calculated for spherical ice particles by Mie theory and the second (right side) using the same parameters except for the phase function of Henyey-Greenstein (HG), which was calculated from the same asymmetry factor as in Mie theory. The most conspicuous difference between these two NBRDFs is the presence of a rainbow in the case of using Mie phase function, where it can be significantly seen at $\lambda = 1.64\mu m$ and it appears at any wavelength although it cannot be seen clearly. On the other hand, no rainbow is seen at any wavelength in the measurements shown in Figure 13. The second point to be noticed is the maximum value of NBRDF that is seen at just below the horizon in the forward scattering direction. It is higher in NBRDF using Mie phase function than in using HG phase function: the values of NBRDF at θ_v = 85° are 3.0 (Mie), 2.2 (HG), and 2.2 (observation) for $\lambda = 0.52\mu m$, and are 23.4 (Mie), 14.2 (HG), and 16.2 (observation) for $\lambda = 1.64\mu m$. From these comparisons of the theoretical NBRDFs with the measured ones, we see that HG phase function simulates our measurement of NBRDF better than Mie theory.

Figure 15 shows Mie and HG phase functions of snow grains in the top layer of the snow model used in these NBRDF calculations. The peak at the scattering angle of around 135° in Mie phase function causes the rainbow of BRDF and the forward scattering peaks in both phase functions are responsible for the maximum value of BRDF. These phenomena can easily be explained where single scattering by snow grains is dominated. Since multiple scattering by snow grains is dominant in the visible region due to the weak absorption of ice, the pattern due to the single scattering is hidden by the multiple scattering. On the contrary, in the near infrared region low order scattering is dominant due to the strong absorption of ice, and this makes the rainbow or maximum value in the forward scattering region in BRDF. As a

result, the shape of the phase function affects the BRDF of snow, and thus the snow grain shape also affects the BRDF. From these points of view it seems that the general hexagonal shapes are not suitable for BRDF calculation, and the spherical shape is not suitable either, because the halo is not usually seen on the snow surface itself although it occasionally appears in the Antarctic Plateau [*Warren et al.*, 1998]. The shapes of snow grains are different from each other and change in the course of the aging of snow. Even in cirrus clouds, the halo does not necessarily appear. In measurements with a polar nephelometer by *Gayet et al.* [1998], examining cirrus of irregular shape, a smooth phase function was observed at forward scattering angles.

Studies on single scattering properties of nonspherical ice particles in clouds can provide us with useful information for our BRDF studies of the snow surface. One suggestive work was done by *Macke et al.* [1996a] who had calculated the phase function for randomized triadic Koch-fractals and found that it becomes smooth with increasing distortion. In this case the complicated shape of the ice particles eliminates particular peaks such as the halo or rainbow in the phase function. Smooth phase functions have been obtained in theoretical calculations for ice particles with inclusions of such as air bubbles or soot [*Macke et al.*, 1996b; *Mishchenko and Macke*, 1997], imperfect hexagonal ice crystals [*Hess et al.*, 1998], a randomly oriented oblate spheroid [*Mishchenko and Travis*, 1998], and a plate of hexagonal ice particles [*Leroux et al.*, 1999]. Comparison of the observations with these models is the next coming item of the present study. In addition, it will be necessary to conduct studies on: (1) direct measurement of the phase function of snow particles at each stage of snow age; and (2) calculation of single scattering for irregular ice particles.

We have seen in this subsection that the shape of the phase function is important for BRDF calculation. It is now worth checking the effect of the phase function on albedo. Figure 16 shows a comparison of theoretical spectral albedos obtained using Mie and HG phase functions for the snow model of February 25. We see that there is almost no difference in spectral albedo between Mie and HG phase functions. This result holds except for the large θ_0. This means that the asymmetry factor is important for albedo, but the detailed shape of the

phase function does not affect the albedo. It leads us to safely say that the use of Mie phase function is appropriate for snow albedo calculations. However, the results presented in this subsection indicate that the observation of only the snow albedo is insufficient for the ground truth in satellite remote sensing of snow.

8. Conclusions

Spectral albedo and BRDF observations in the wavelength range from 0.35 to $2.5\mu m$ were made on a flat snowfield in the mid-latitude region. From comparisons of the observed spectral albedos and theoretical ones obtained in calculations using a multiple scattering model for the atmosphere-snow system, the reduction detected in visible albedo could be explained by the high concentration of snow impurities at the surface ($\leq 1cm$), where the total column amount of impurities in the layer of $0 - 5cm$ was as much as that measured in snow pit work. This suggests that the high concentration of impurities at the surface was caused by dry fallout of atmospheric aerosols. The optically equivalent size of snow grains was estimated on the basis of the albedo in the near infrared region of $\lambda > 1.4\mu m$, and was found to be of the order of a branch width of dendrites or of a dimension of narrower portion of broken crystals. This size was smaller than both the mean grain size and the effective grain size obtained from micrographs by image processing. However, if the snow grains on the micrographs were assumed to be hexagonal columns, the radius of equal volume-to-surface-area ratio sphere became close to the optically equivalent snow grain size. These results suggest that careful interpretation of retrieved data will be necessary in satellite remote sensing of snow grain size and impurities in the future.

In the measurement of BRDF, the anisotropic reflection patterns were significant in the near infrared region of $\lambda > 1.4\mu m$, while the visible BRDF patterns were relatively flat. Comparisons with the theoretically calculated BRDFs showed that HG phase function was more suitable than Mie phase function, while the spectral albedos calculated with both phase functions agreed with each other with negligible error. This indicates that the phase function (thus, the grain shape) affects the BRDF of snow and an asymmetry factor is generally

important for the spectral albedo. The shapes of individual snow grains are generally so different that a particular shape such as a sphere is not employable for BRDF calculation. It is thus desirable to pursue studies such as the direct measurements of the phase function of snow grains at each stage of the aging of snow together with theoretical calculations for the irregular ice particles. These are important steps required for making a successful satellite remote sensing of snow surface.

Acknowledgments. This work was conducted as part of the ADEOS II/GLI Cal/Val experiment supported by NASDA (National Space Development Agency of Japan). We would like to thank Mr. Isao Itoh (Meteorological Research Institute) for developing the albedo observation system. We also thank Messrs. Yukinori Nakajima, Hiroki Kai, and Yasuhiro Nakajima (Remote Sensing Technology Center) for their logistic support. Thanks are due to Mr. Hijiri Himono (Hokkaido University of Education) and Miss Kimiko Shimohara (Kitami Institute of Technology) for their help in this field experiment, and Miss Mineko Yamaguchi (The University of Tokyo) and Mrs. Qingyi Xu (University of Tsukuba) for analyzing the spectral data and collected samples. We are indebted to Drs. Kikuo Okada and Masataka Murakami (Meteorological Research Institute), respectively, for the use of the SEM system and the image processing system. Discussions with Profs. Takenori Noumi (Meteorological Collage), Teruyuki Nakajima (The University of Tokyo), Takashi Yamanouchi (National Institute of Polar Research), and Harumi Isaka (Université Blaise Pascal) were fruitful for this study.

References

AFGL, *Handbook of geophysics and the space environment,* Air Force Geophysics Laboratory, 1985.

Anderson, G. P., S. A. Clough, F. X. Kneizys, J. H. Chetwynd, and E. P. Shettle, *AFGL atmospheric constituent profiles (0-120km)*, AFGL-TR-86-0110, 43 pp., Air Force Geophysics Laboratory, Hanscom, MA, 1986.

Aoki, Te., Ta. Aoki, M. Fukabori, Y. Tachibana, Y. Zaizen, F. Nishio, and T. Oishi, Spectral albedo observation on the snow field at Barrow, Alaska, *Polar Meteor. Glaciol., 12*, 1-9, 1998.

Aoki, Te., Ta. Aoki, M. Fukabori, and A. Uchiyama, Numerical simulation of the atmospheric effects on snow albedo with a multiple scattering radiative transfer model for the atmosphere-snow system, *J. Meteor. Soc. Japan*, 77, 595-614, 1999.

Bohren, C. F., and D. R. Huffman, *Absorption and Scattering of Light by Small Particles*, 530 pp, Wiley, New York, 1983.

Brandt, R. E., T. C. Grenfell, and S. G. Warren, Optical properties of snow, *Antarct. J. U.S.*, *26*, 272-275, 1991.

Carlson, R. W, and T. Arakelian, Spectral bidirectional reflectance and energy absorption rates of antarctic snow, *Antarct. J. U.S., 28*, 256-258, 1993.

Chylek, P., V. Ramaswamy, and V. Srivastava, Albedo of soot-contaminated snow, *J. Geophys. Res.*, *88*, 10837-10843, 1983.

Clarke, A. D., Effects of filter internal reflection coefficient on light absorption measurements made using the integrating plate method, *Appl. Opt.*, *21*, 3021-3031, 1982.

Dirmhirn, I., and F. D. Eaton, Some characteristics of the albedo of snow, *J. Appl. Meteorol.*, *14*, 375-379, 1975.

Gayet, J.-F., F. Auriol, S. Oshchepkov, F. Schröder, C. Duroure, G. Febvre, J.-F. Fournol, O. Crépel, P. Personne, and D. Daugereon, In situ measurements of the scattering phase function of stratocumulus, contrails, and cirrus, *Geophys. Res. Lett.*, *25*, 971-974, 1998.

Grenfell, T. C., A visible and near-infrared scanning photometer for field measurements of spectral albedo and irradiance under polar conditions, *J. Glaciol.*, *27*,476-481, 1981.

Grenfell, T. C., and G. A. Maykut, The optical properties of ice and snow in the Arctic Basin, *J. Glaciol.*, *18*, 445-463, 1977.

Grenfell, T. C., D. K. Perovich, and J. A. Ogren, Spectral albedos of an alpine snowpack, *Cold Regions Sci. Technol.*, *4*, 121-127, 1981.

Grenfell, T. C., and D. K. Perovich, Spectral albedos of sea ice and incident solar irradiance in the southern Beaufort Sea, *J. Geophys. Res.*, *89*, 3573-3580, 1984.

Grenfell, T. C., S. G. Warren, and P. C. Mullen, Reflection of solar radiation by the Antarctic snow surface at ultraviolet, visible, and near-infrared wavelengths, *J. Geophys. Res.*, *99*, 18,669-18,684, 1994.

Grenfell, T. C., and S. G. Warren, Representation of a nonspherical ice particle by a collection of independent sphere for scattering and absorption of radiation, *J. Geophys. Res.*, in press, 1999.

Han, W., *Remote sensing of surface albedo and cloud properties in the Arctic from AVHRR measurements*, D. S. thesis, 129 pp, Univ. of Alaska, Fairbanks, 1996.

Hansen, J. E., Multiple scattering of polarized light in planetary atmospheres. Part I. The doubling method, *J. Atmos. Sci.*, *28*, 120-125, 1971.

Hansen, J. E., and L. D. Travis, Light scattering in planetary atmospheres. *Space Sci. Rev.*, *16*, 527-610, 1974.

Hess, M., R. B. A. Koelemeijer, and P. Stammes, Scattering matrices of imperfect hexagonal ice crystals, *J. Quant. Spectrosc. Radiant Transfer*, *60*, 301-308, 1998.

Japanese National Astronomical Observatory, *Rika Nenpyo* (in Japanese), 1058 pp, Maruzen Co., Ltd., 1999.

JMA, *Annual report of background air pollution observation 1997*, Japan Meteorological Agency, 83 pp, 1999.

Kou, L., D. Labrie, and P. Chylek, Refractive indices of water and ice in the 0.65- to 2.5-μm spectral range, *Appl. Opt.*, *32*, 3531-3540, 1993.

Kuhn, M., Anisotropic reflection from sastrugi fields, *Antarct. J. U.S.*, *9*, 123-125, 1974.

Kuhn, M., Bidirectional reflectance of polar and alpine snow surfaces, *Ann. Glaciol., 6*, 164-167, 1985.

Kuhn, M., and L. Siogas, Spectroscopic studies at McMurdo, South Pole, and Siple Stations during the austral summer 1977-78, *Antarct. J. U.S., 13*, 178-179, 1978.

Leroux, C., J. Lenoble, J. L. Deuzé, P. Goloub, C. Sergent, and M. Fily, Modeling and measurements of snow reflectance from visible to near infrared, in *IRS'96: Current Problems in Atmospheric Radiation*, ed. by W. L. Smith and K. Stamnes, 37-40, 1997.

Leroux, C., and M. Fily, Modeling the effect of sastrugi on snow reflectance, *J. Geophys. Res., 103,* 25,779-25,788, 1998.

Leroux, C., J. Lenoble, G. Brogniez, J. W. Hovenier, and J. F. De Haan, A model for the bidirectional polarized reflectance of snow, *J. Quant. Spectrosc. Radiat. Transfer, 61*, 273-285, 1999.

Li, S., *A model for the anisotropic reflectance of pure snow*, M.S. thesis, 60 pp, Univ. of Calif., Santa Barbara, 1982.

Liljequist, G. H., Energy exchange of an Antarctic snow-field: A. Short-wave radiation; B. Long-wave radiation and radiation balance, in *Norwegian-British-Swedish Antarctic Expedition, 1949-52, Scientific Results*, Vol. 2, Part 1, Norsk Polarinstitutt, Oslo, 1-184, 1956.

Lin, C.-I., M. Baker, and R. J. Charlson, Absorption coefficient of atmospheric aerosol: a method for measurement, *Appl. Opt., 12*, 1356-1363, 1973.

Lindberg, J. D., and L. S. Laude, Measurement of the absorption coefficient of atmospheric dust, *Appl. Opt., 13*, 1923-1927, 1974.

Macke, A., J. Mueller, and E. Raschke, Single scattering properties of atmospheric ice crystals, *J. Atmos. Sci., 53*, 2813-2825, 1996a.

Macke, A., M. I. Mishchenko, and B. Cairns, The influence of inclusions on light scattering by large ice particles, *J. Geophys. Res., 101,* 23,311-23,316, 1996b.

Mishchenko, M. I., and A. Macke, Asymmetry parameters of the phase function for isolated

and densely packed spherical particles with multiple internal inclusions in the geometric optics limit, *J. Quant. Spectrosc. Radiat. Transfer*, *57*, 767-794, 1997.

Mishchenko, M. I., and L. D. Travis, Capabilities and limitations of a current FORTRAN implementation of the T-matrix method for randomly oriented, rotationally symmetric scatterers, *J. Quant. Spectrosc. Radiat. Transfer*, *60*, 309-324, 1998.

Nakajima, T. Y., T. Nakajima, M. Nakajima, H. Fukushima, M. Kuji, A. Uchiyama, and M. Kishino, Optimization of the Advanced Earth Observing Satellite II Global Imager channels by use of radiative transfer calculations, *Appl. Opt.*, *37*, 3149-3163, 1998.

O'Brien, H. W., Observations of the ultraviolet spectral reflectance of snow, *CRREL Rep. 77-27*, U. S. Army Cold Reg. Res. and Eng. Lab., Hanover, N. H., 1977. (Available as NTIS AD-A046 349 / 7GI).

O'Brien, H. W., and R. H. Munis, Red and near-infrared spectral reflectance of snow, *CRREL Res. Rep., 332*, U. S. Army Cold Reg. Res. and Eng. Lab., Hanover, N. H., 1975. (Available as NTIS AD-A007 732 / 1GI, from the Natl. Tech. Inf. Service, Springfield, Va.)

O'Brien, H. W., and G. Koh, Near-infrared reflectance of snow-covered substrates, *CRREL Rep. 81-21*, U. S. Army Cold Reg. Res. and Eng. Lab., Hanover, N. H., 1981.

Patterson, E. M., D. A. Gillette, and B. H. Stockton, Complex index of refraction between 300 and 700 nm for Saharan Aerosols, *J. Geophys. Res.*, *82*, 3153-3160, 1977.

Salomonson, V. V., and W. E. Marlatt, Anisotropic solar reflectance over white sand, snow and stratus clouds, *J. Appl. Meteorol.*, *7*, 475-483, 1968.

Sergent, C., C. Leroux, E. Pougatch, and F. Guirado, Hemispherical-directional reflectance measurements of natural snow in the 0.9-1.45 μm spectral range: comparison with adding-doubling modeling, *Ann. Glaciol., 26*, 59-63, 1998.

Steffen, K., Bidirectional reflectance of snow at 500-600 nm, in *Large Scale Effects of Seasonal Snow Cover*, edited by B. Goodison *et. al.*, IAHS Publ. 166 pp. 415-425, Int. Assoc. of Hydrol. Sci., Wallingford, England, 1987.

Steffen, K., Effect of solar zenith angle on snow anisotropic reflectance, in *IRS'96: Current*

Problems in Atmospheric Radiation, ed. by W. L. Smith and K. Stamnes, 41-44, 1997.

Taylor, V. R., and L. L. Stowe, Reflectance characteristics of uniform Earth and cloud surfaces derived from NIMBUS 7 ERB, *J. Geophys. Res.*, *89*, 4987-4996, 1984a.

Taylor, V. R., and L. L. Stowe, Atlas of reflectance patterns for uniform earth and cloud surfaces (NIMBUS-7 ERB--61 days), *NOAA Tech. Rep. NESDIS 10*, Natl. Oceanic and Atmos. Admin., Washington D.C., 1984b.

Warren, S. G., Optical properties of snow, *Rev. Geophys. Space Phys.*, *20*, 67-89, 1982.

Warren, S. G., Optical constants of ice from the ultraviolet to the microwave, *Appl. Opt.*, *23*, 1206-1225, 1984.

Warren, S. G., T. C. Grenfell, and P. C. Mullen, Optical properties of Antarctic snow, *Antarct. J. U.S.*, *21*, 247-248, 1986.

Warren, S. G., and W. J. Wiscombe, A model for the spectral albedo of snow, II: Snow containing atmospheric aerosols, *J. Atmos. Sci.*, *37*, 2734-2745, 1980.

Warren, S. G., R. E. Brandt, and P. O'Rawe Hinton, Effect of surface roughness on bidirectional reflectance of Antarctic snow, *J. Geophys. Res.*, *103,* 25,789-25,807, 1998.

Wiscombe, W. J., and S. G. Warren, A model for the spectral albedo of snow, I: Pure snow, *J. Atmos. Sci.*, *37*, 2712-2733, 1980.

Figure captions

Figure 1. Map showing the locations of observation sites in eastern Hokkaido, Japan. The sea of Okhotsk was mostly covered by sea ice during the observation period. The prevailing wind at the time of snowfall was northwestern.

Figure 2. Vertical profiles of snow parameters obtained from snow pit work from February 22 to 25, 1998. Snow types are indicated as NS for new snow, H1 for faceted crystals, H2 for depth hoar, S1 for fine-grained old snow, C for crust, and G for granular snow. Snow grain sizes were measured with approximately $10\mu m$-resolution using a handheld lens for two kinds of dimensions, where one is a half the length of major axis of crystals or dendrites (r_1), and the other is a half the branch width of dendrites or a half the dimension of narrower portion of broken crystals (r_2). Snow impurities were collected on the Nuclepore filters and the concentration was estimated by means of a balance. The snow sample name is indicated in parentheses below the concentration of impurities.

Figure 3. Micrographs of snow grains (a) - (d) for the surface from February 22 to February 25, 1998 and (e) - (f) for $5cm$ - and $20cm$-depths on February 23, 1998.

Figure 4. Size distributions of sphere-equivalent radius of snow grains at the surface obtained by image processing from February 22 to 25, 1998. The values $\bar{r}_{image}$ and r_{image}^{eff} are, respectively, the mean radius and the effective radius, and N is the total number of processed snow grains. The highly aggregated grains on the micrographs were excluded in image processing.

Figure 5. Albedo observation system: (top) photograph of the observational setup; and (bottom) a schematic diagram of the setup for downward and upward flux observations. The downward flux was observed by directing the optical fiber tip of the spectrometer downward to the upper surface of WRS which was attached horizontally to the edge of a

pipe (black part) with a length of $0.9m$ stretching from the mount on a tripod. In the case of the upward flux observation, an arm holding the optical fiber tip (hatched parts) turned by 180° around the pipe. The distance of WRS from the snow surface was about $0.3m$.

Figure 6. (a) Deviation from the perfect cosine property in the incident angle dependence of the reflectance of WRS (shown by characters) and the azimuthally integrated shading fraction by the optical fiber arm for each angle of incidence viewed from the center of the field of view of the optical fiber on WRS (solid line). The underestimate of radiant flux due to the imperfect cosine property of WRS was 5.36 % for complete diffuse illumination, and 6.19 % for direct solar beam at $\theta_0 = 56.8°$. The total shading fraction by the optical fiber arm was 6.56 % for complete diffuse illumination. (b) Fractions of the diffuse component ($r_{diff}(\theta_0, \lambda)$: thin dashed line) and the direct component ($r_{dir}(\theta_0, \lambda)$: thick dashed line) in downward solar flux theoretically calculated for $\theta_0 = 56.8°$, and correction coefficients for upward solar flux ($C_{Fup}^{WRS} C_{Fup}^{arm}$: middle solid line), downward solar flux ($C_{Fdn}^{WRS}(\theta_0, \lambda) C_{Fdn}^{arm}(\theta_0, \lambda)$: thin solid line), and albedo ($C_{albedo}(\theta_0, \lambda)$: thick solid line) on February 23, 1998.

Figure 7. Scanning electron microscope (SEM) photographs of snow impurities collected on Nuclepore filters for the snow samples (top) 980223A1 ($0 - 5cm$) and (bottom) 980223A2 ($5 - 10cm$) on February 23, 1998.

Figure 8. Spectral variations of refractive indices of snow impurities estimated from measurement of the transmittance of a Nuclepore filter on which the impurities in the snow sample 980223A1 had been collected. Imaginary parts ($m_{im}(\lambda)$) are shown by solid lines with the left ordinate, and real parts ($m_{re}(\lambda)$) are shown by dashed lines with the right ordinate. Values for soot [*AFGL*, 1985], Dust-Like aerosol [*AFGL*, 1985], and ice [*Warren*, 1984; *Kou et al.*, 1993] are also plotted for comparison. The fitted

curve of $m_{im}(\lambda)$ obtained by means of a cubic equation of wavelength for the snow sample is given by $m_{im}(\lambda) = -0.0141\lambda^3 + 0.0611\lambda^2 - 0.0478\lambda + 0.0317$.

Figure 9. Observed spectral albedo (left ordinate), its standard deviation (right ordinate) on February 23, 1998 and theoretically calculated spectral albedos for four kinds of snow models shown in Figure 10. Observed data are thinned down to one twentieth and only those for which the standard deviation was less than 0.1 are shown. Other observation conditions are shown in Table 1.

Figure 10. Snow models for which the theoretical spectral albedos were compared with the measurement on February 23, 1998, where r_{eff} is the effective snow grain radius, ρ is the snow density, and s is the concentration of impurities. In the column of m_{im} the name of the snow sample is indicated from which the imaginary refractive index of impurities was derived.

Figure 11. Same as Figure 9 for Model-4, but for (a) February 22, (b) February 24, and (c) February 25 in 1998. Observation conditions are shown in Table 1.

Figure 12. Snow models on (a) February 22, (b) February 24, and (c) February 25 in 1998, for which the theoretical spectral albedos were calculated and compared with the measurements as shown in Figure 11.

Figure 13. Composite NBRDFs of snow for 6 wavelengths as obtained from measurements of anisotropic reflectance with an optical fiber of 25°-FOV for $\theta_v \leq 70°$ and those obtained with foreoptics of 1°-FOV for $\theta_v \geq 80°$. The measurements using the optical fiber were made in 12:22 - 12:58 LT ($\theta_0 = 54.0 - 56.0°$) and using the foreoptics in 13:20 - 13:34 LT ($\theta_0 = 57.9 - 59.3°$) on February 25, 1998 at Site-B. All reflectances are normalized by the value at the nadir. The plus signs on the each NBRDF map

indicate the observed points. The radial coordinate is proportional to the viewing angle θ_v, which is zero at the center of the circle (nadir) and is 90° on the circle. The illumination from the Sun comes from the lower direction of each map, so the bottom of the each map is the forward scattering direction.

Figure 14. Theoretical NBRDFs of snow for 6 wavelengths. The semicircular maps on the left side were calculated using Mie phase function and those on the right side using HG phase function. The mesh points on each of the NBRDF maps indicate the grid points where calculations were made.

Figure 15. Mie and HG phase functions of snow grains for $\lambda = 0.52$ and $1.64\,\mu m$ in the top layer of the snow model (see Figure 12c) of February 25, 1998. The curves for $\lambda = 1.64\,\mu m$ are displaced upward by a factor of 10^2.

Figure 16. Comparison of theoretical albedos using Mie and HG phase functions (left ordinate) for the snow model of February 25, 1998. The difference between the two albedos is shown on the right ordinate.

Table 1. Locations and Conditions of Observation of Snow Albedo

Date	Site	Latitude	Longitude	Height	Local time	θ_0	Sky condition
Feb. 22, 1998	Site A	43° 56' 20" N	143° 39' 25" E	105 m	11:26 - 11:41	54.2 - 54.3°	5/10 Cu and 1/10 Ac
Feb. 23, 1998	Site B	43° 45' 33" N	144° 10' 26" E	57 m	10:14 - 10:15	56.8 - 56.9°	1/10 Cu
Feb. 24, 1998	Site C	43° 45' 55" N	144° 11' 18" E	75 m	12:23 - 12:25	54.4 - 54.5°	Clear
Feb. 25, 1998	Site B	43° 45' 33" N	144° 10' 26" E	57 m	10:34 - 10:36	54.7 - 54.8°	Clear

The value of θ_0 means the solar zenith angle.

Table 2. Comparison of Grain Radii (μm) of Snow Surface Obtained from Snow Pit Work (r_1 and r_2), Image Processing ($\bar{r}_{image}$, r_{image}^{eff} and r_{VA}), and Spectral Albedo Fitting in the Region $\lambda > 1.4\mu m$ (r_{fit})

Date	r_1	r_2	$\bar{r}_{image}$	r_{image}^{eff}	r_{VA}	r_{fit}
Feb. 22, 1998	100 - 750	50 - 100	89	140	42	35
Feb. 23, 1998	300 - 500	50 - 150	109	163	57	55
Feb. 24, 1998	100 - 500	50 - 150	132	195	77	65
Feb. 25, 1998	250 - 750	50 - 150	143	220	96	85

The value of r_1 is a half the length of the major axis of crystals or dendrites, and r_2 is a half the branch width of dendrites or a half the dimension of narrower portion of broken crystals. The values $\bar{r}_{image}$ and r_{image}^{eff} are the mean radius and the effective radius, respectively. The radius of the equal-V/A sphere r_{VA} is given by the equation (12). The value of r_{fit} is a theoretical effective radius of the top layer of snow that gives the best fit to observed spectral albedo in the region of $\lambda > 1.4\mu m$.

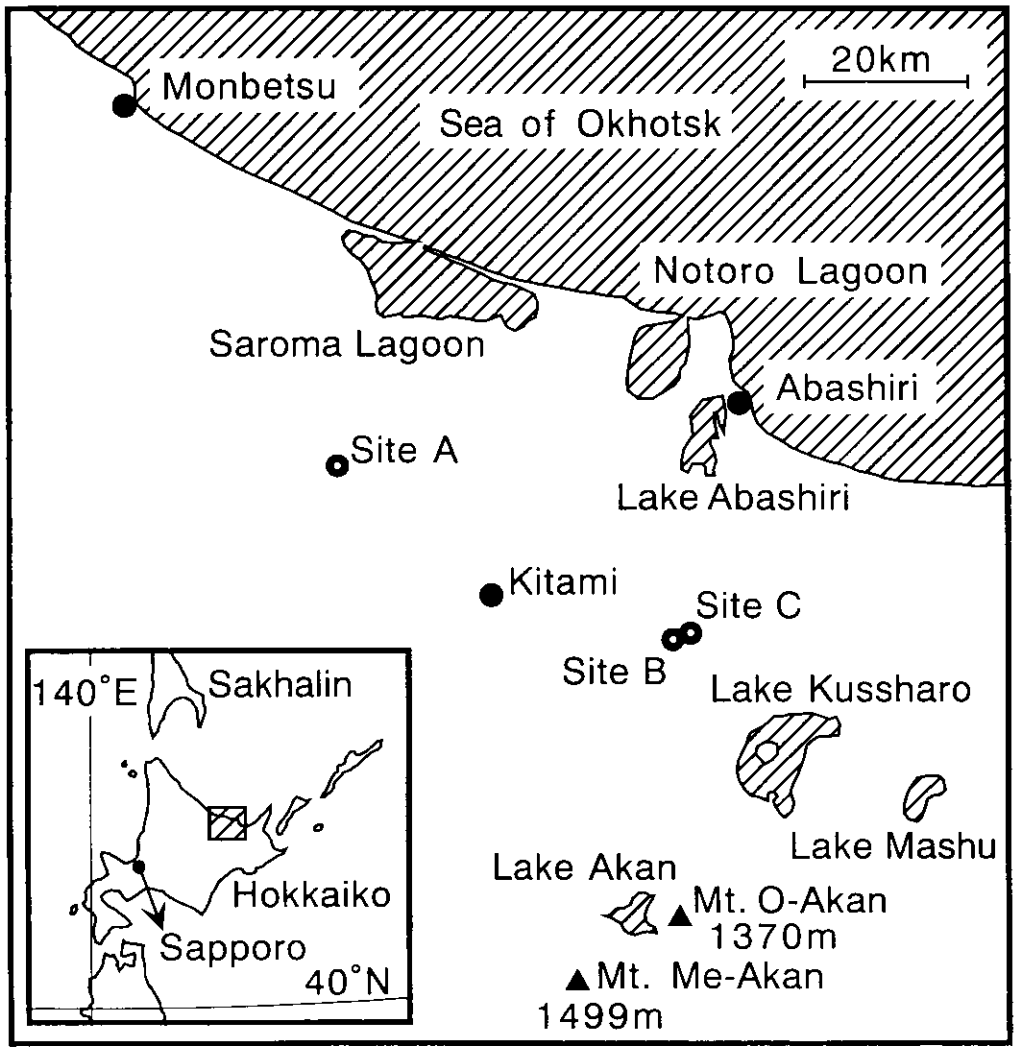

Figure 1. Map showing the locations of observation sites in eastern Hokkaido, Japan. The sea of Okhotsk was mostly covered by sea ice during the observation period. The prevailing wind at the time of snowfall was northwestern.

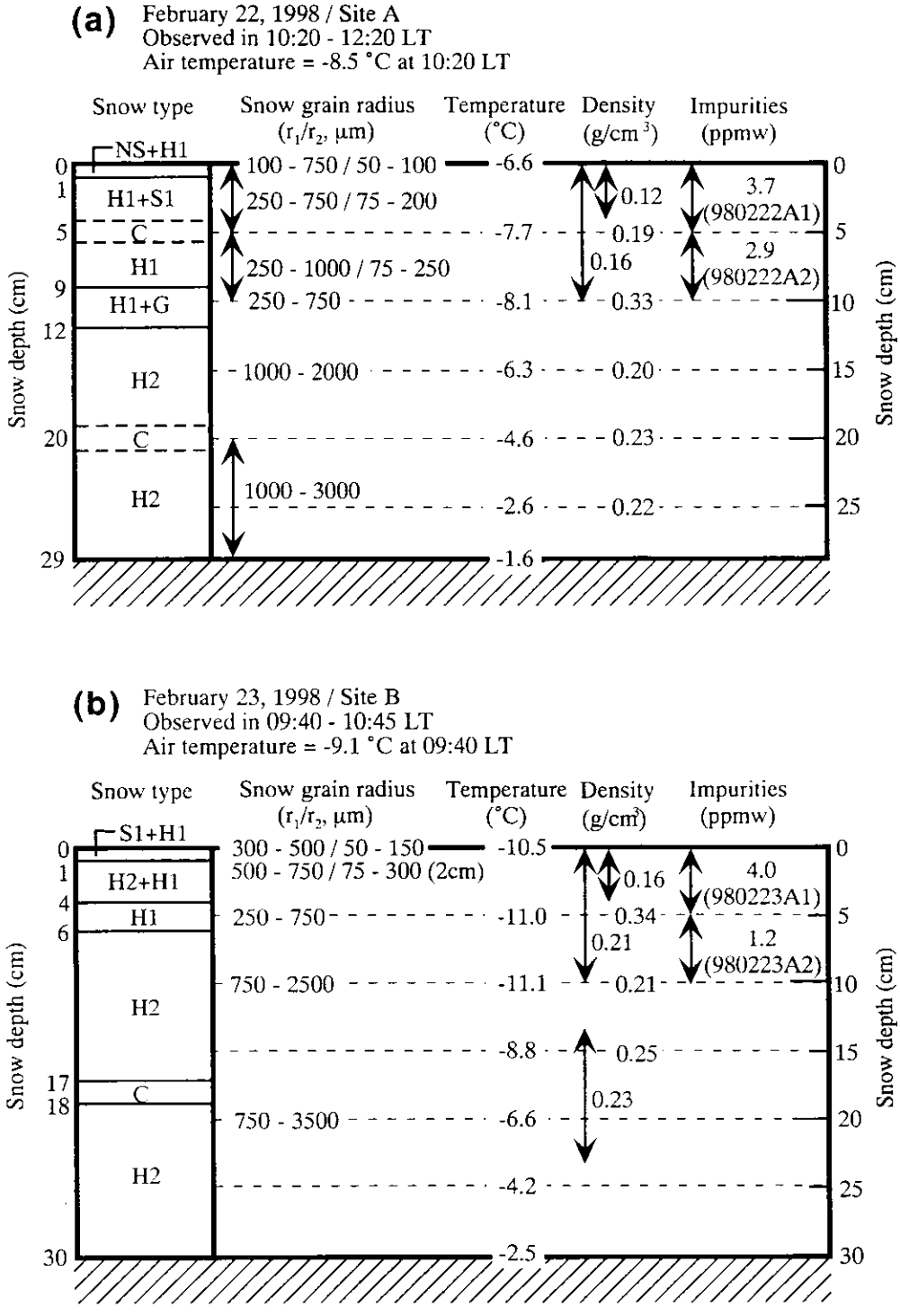

Figure 2. Vertical profiles of snow parameters obtained from snow pit work from February 22 to 25, 1998. Snow types are indicated as NS for new snow, H1 for faceted crystals, H2 for depth hoar, S1 for fine-grained old snow, C for crust, and G for granular snow. Snow grain sizes were measured with approximately $10 \mu m$-resolution using a handheld lens for two kinds of dimensions, where one is a half the length of major axis of crystals or dendrites (r_1), and the other is a half the branch width of dendrites or a half the dimension of narrower portion of broken crystals (r_2). Snow impurities were collected on the Nuclepore filters and the concentration was estimated by means of a balance. The snow sample name is indicated in parentheses below the concentration of impurities.

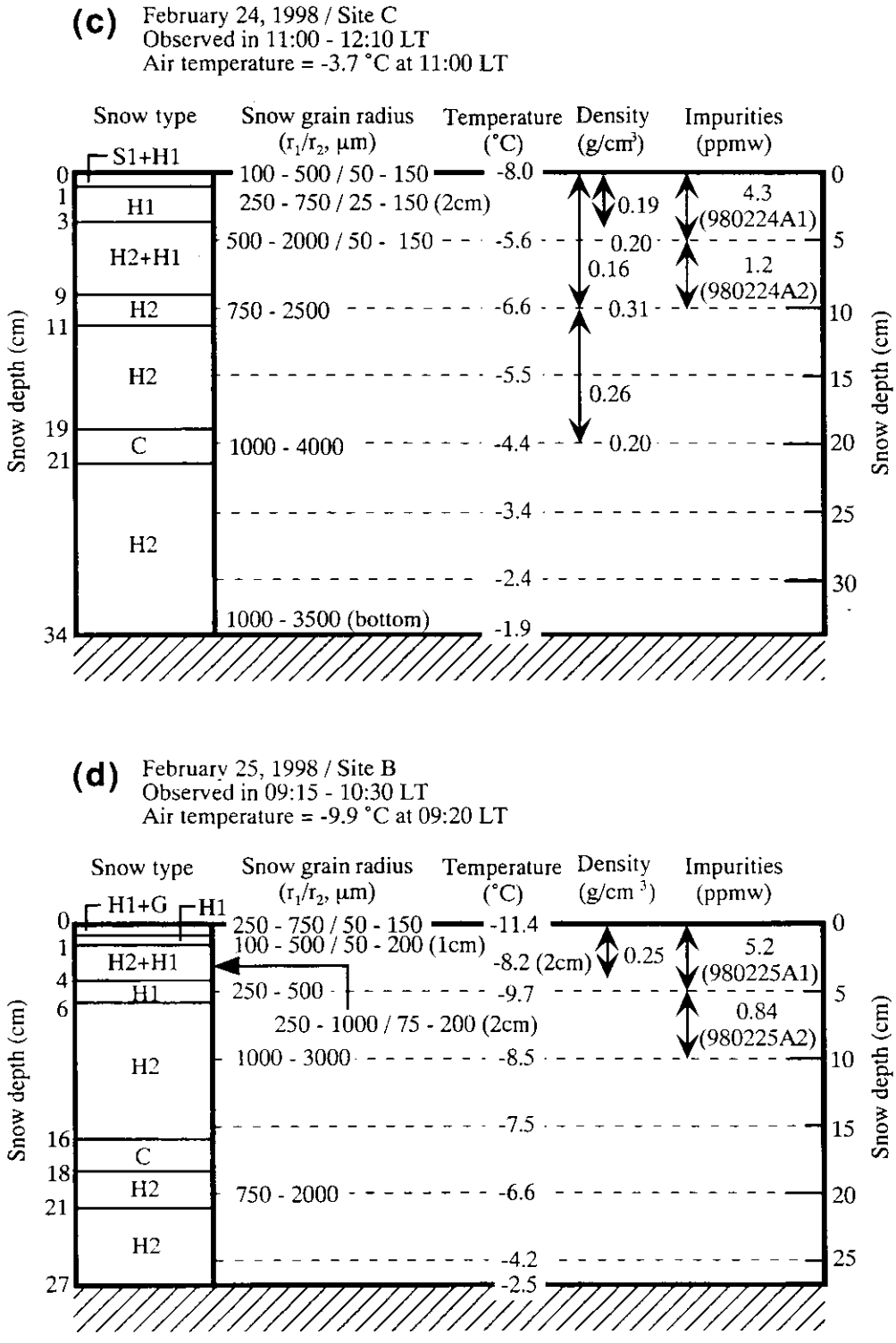

Figure 2. Vertical profiles of snow parameters obtained from snow pit work from February 22 to 25, 1998. Snow types are indicated as NS for new snow, H1 for faceted crystals, H2 for depth hoar, S1 for fine-grained old snow, C for crust, and G for granular snow. Snow grain sizes were measured with approximately $10\,\mu m$-resolution using a handheld lens for two kinds of dimensions, where one is a half the length of major axis of crystals or dendrites (r_1), and the other is a half the branch width of dendrites or a half the dimension of narrower portion of broken crystals (r_2). Snow impurities were collected on the Nuclepore filters and the concentration was estimated by means of a balance. The snow sample name is indicated in parentheses below the concentration of impurities.

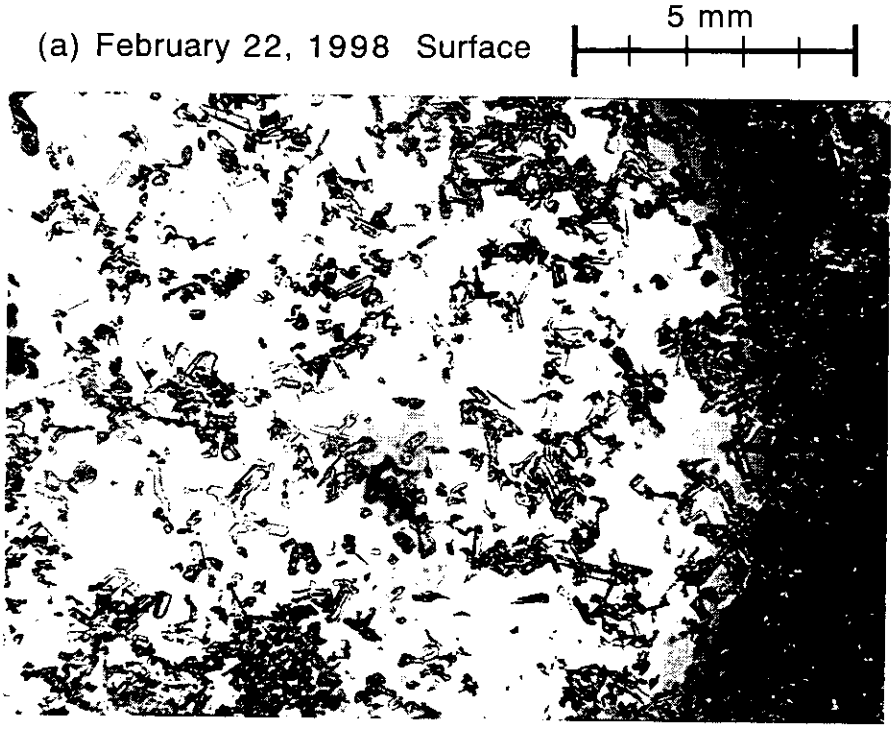

Figure 3. Micrographs of snow grains (a) - (d) for the surface from February 22 to February 25, 1998 and (e) - (f) for 5*cm* - and 20*cm* -depths on February 23, 1998.

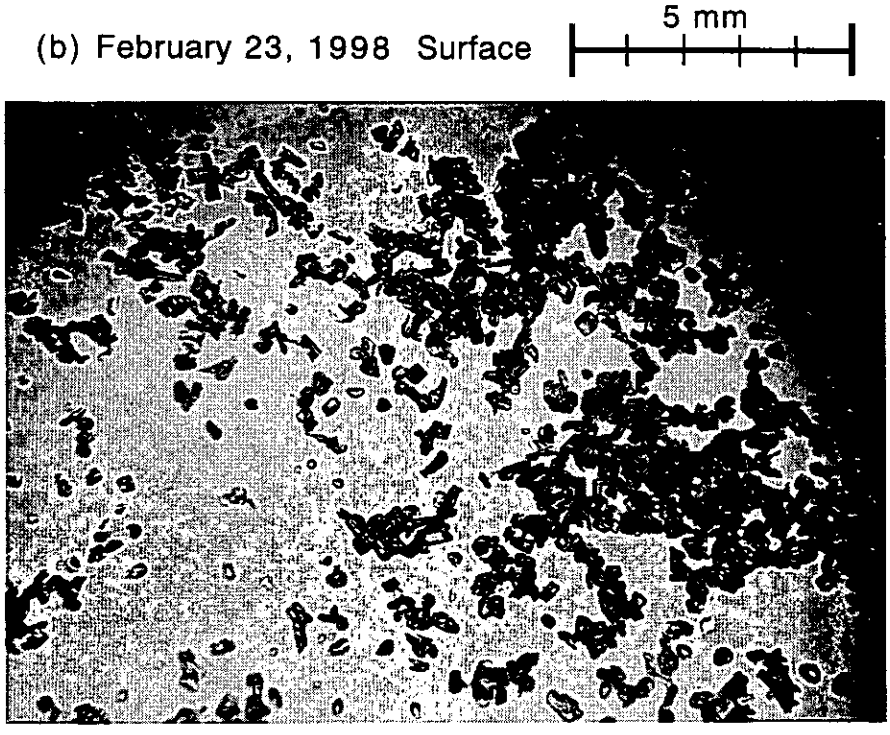

Figure 3. Micrographs of snow grains (a) - (d) for the surface from February 22 to February 25, 1998 and (e) - (f) for 5*cm* - and 20*cm* -depths on February 23, 1998.

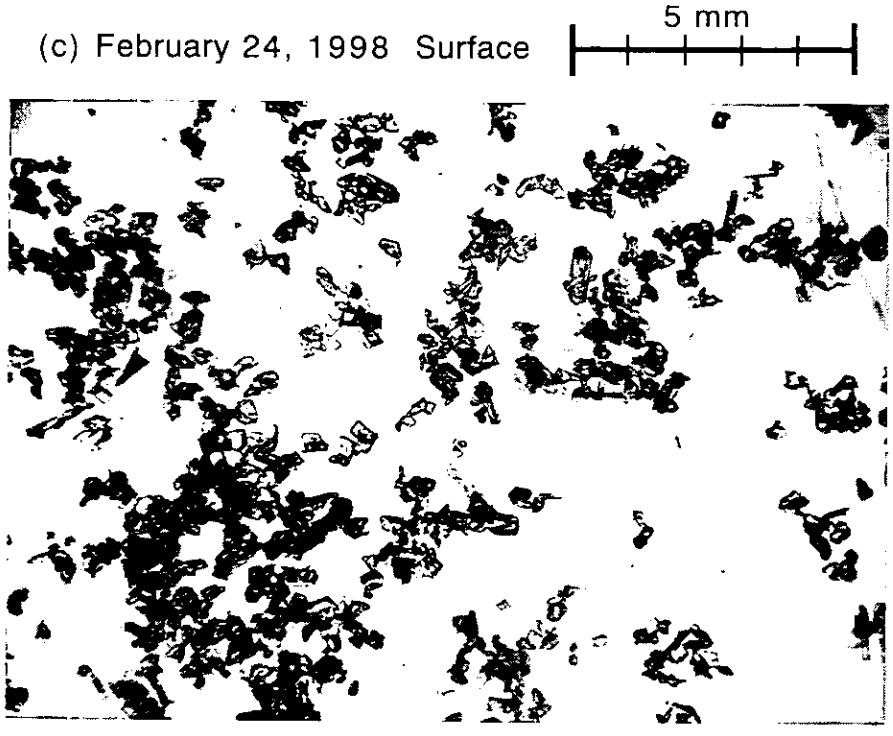

Figure 3. Micrographs of snow grains (a) - (d) for the surface from February 22 to February 25, 1998 and (e) - (f) for 5*cm* - and 20*cm* -depths on February 23, 1998.

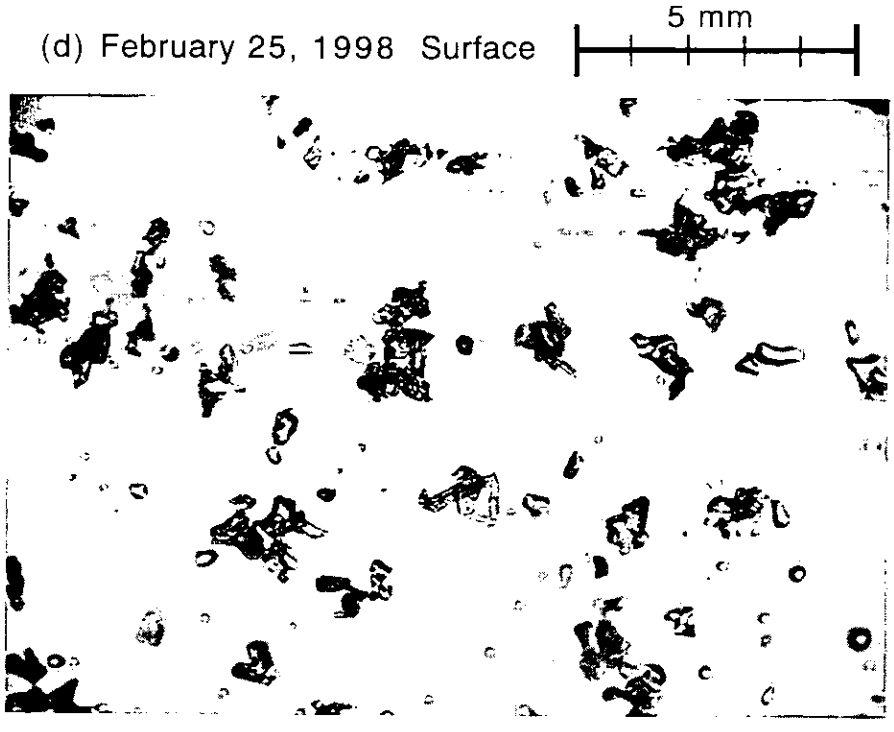

Figure 3. Micrographs of snow grains (a) - (d) for the surface from February 22 to February 25, 1998 and (e) - (f) for $5cm$ - and $20cm$ -depths on February 23, 1998.

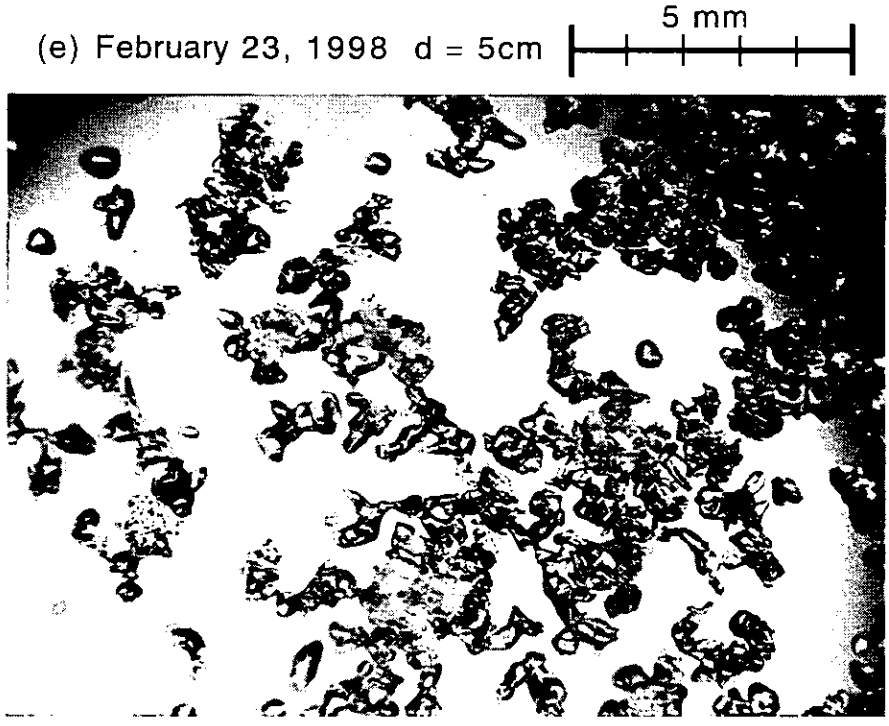

Figure 3. Micrographs of snow grains (a) - (d) for the surface from February 22 to February 25, 1998 and (e) - (f) for 5*cm* - and 20*cm* -depths on February 23, 1998.

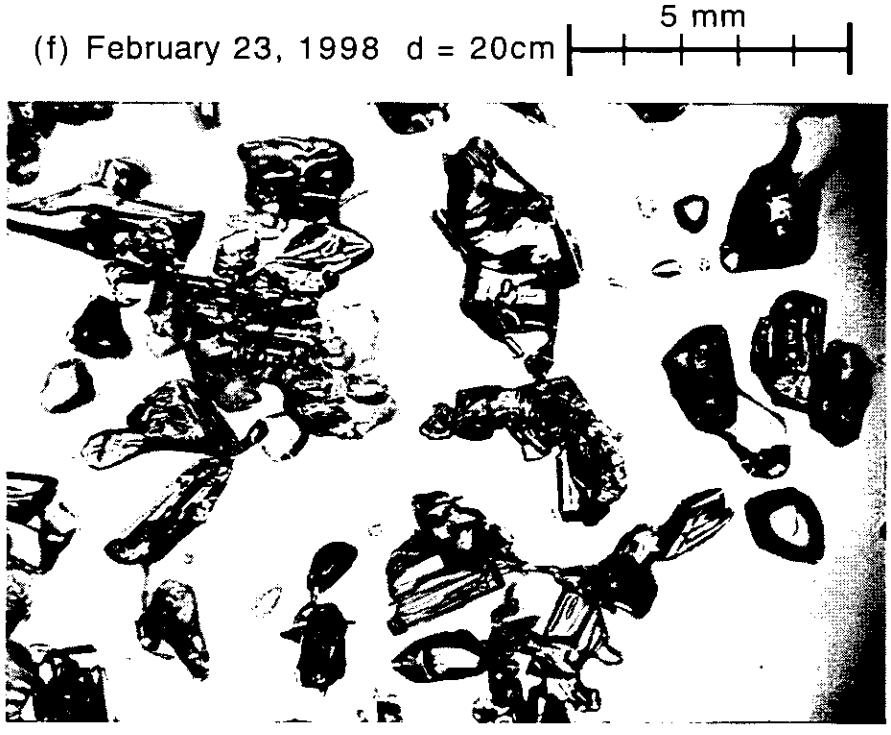

Figure 3. Micrographs of snow grains (a) - (d) for the surface from February 22 to February 25, 1998 and (e) - (f) for 5*cm* - and 20*cm* -depths on February 23, 1998.

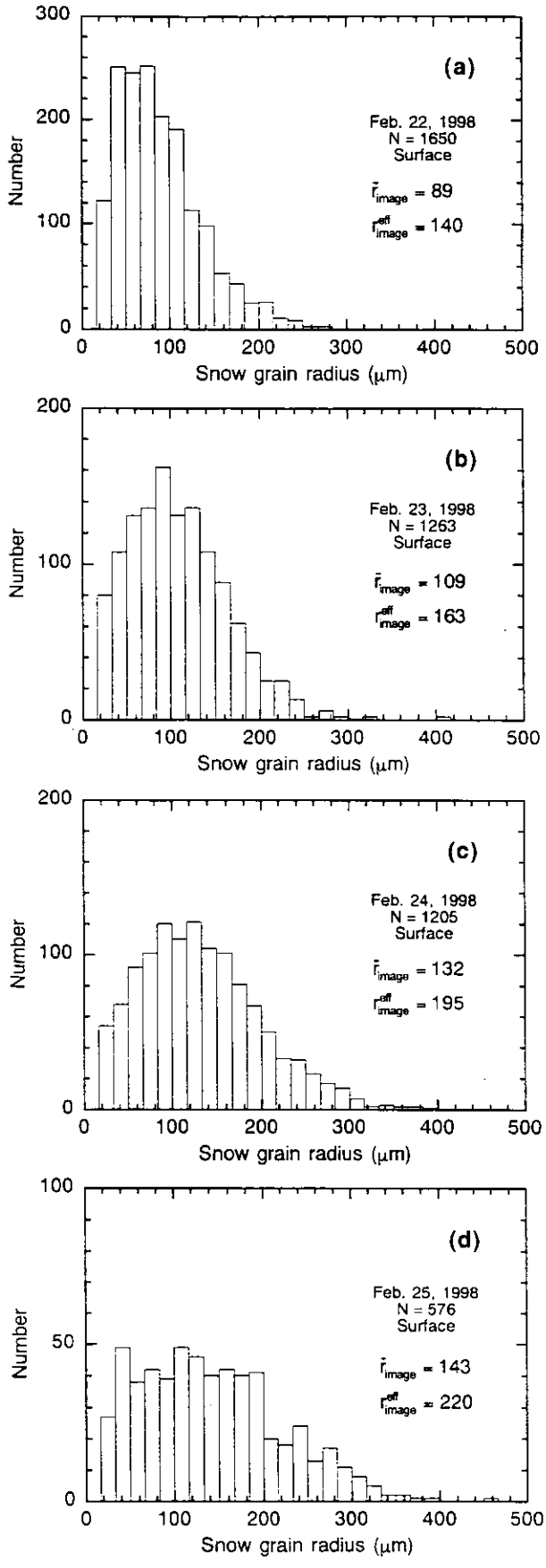

Figure 4. Size distributions of sphere-equivalent radius of snow grains at the surface obtained by image processing from February 22 to 25, 1998. The values $\bar{r}_{image}$ and r^{eff}_{image} are, respectively, the mean radius and the effective radius, and N is the total number of processed snow grains. The highly aggregated grains on the micrographs were excluded in image processing.

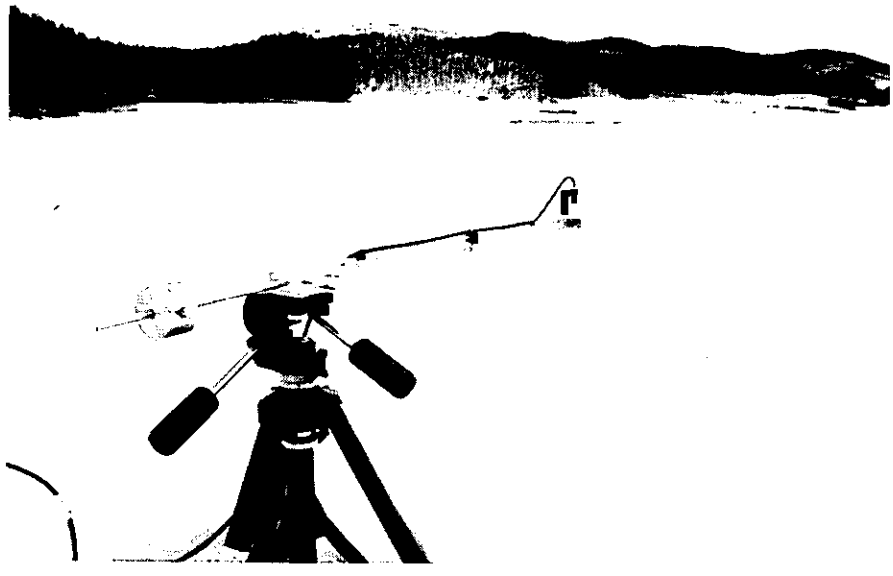

Figure 5. Albedo observation system: (top) photograph of the observational setup; and (bottom) a schematic diagram of the setup for downward and upward flux observations. The downward flux was observed by directing the optical fiber tip of the spectrometer downward to the upper surface of WRS which was attached horizontally to the edge of a pipe (black part) with a length of $0.9m$ stretching from the mount on a tripod. In the case of the upward flux observation, an arm holding the optical fiber tip (hatched parts) turned by 180° around the pipe. The distance of WRS from the snow surface was about $0.3m$.

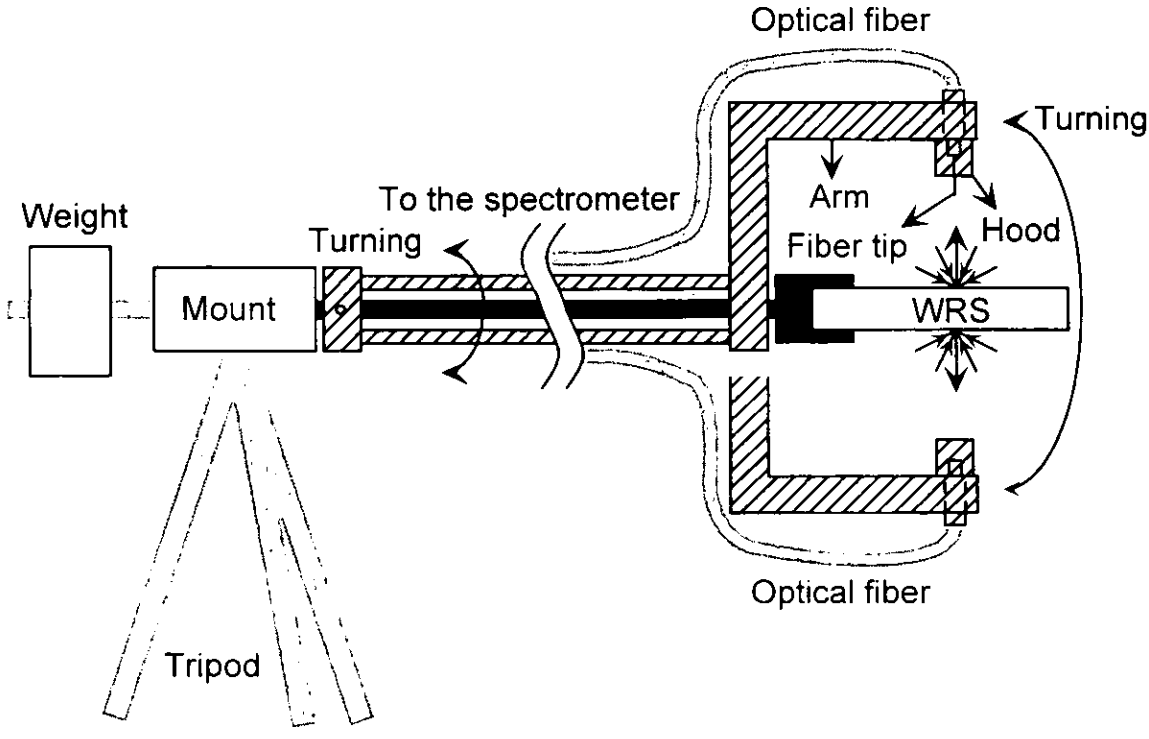

Figure 5. Albedo observation system: (top) photograph of the observational setup; and (bottom) a schematic diagram of the setup for downward and upward flux observations. The downward flux was observed by directing the optical fiber tip of the spectrometer downward to the upper surface of WRS which was attached horizontally to the edge of a pipe (black part) with a length of $0.9m$ stretching from the mount on a tripod. In the case of the upward flux observation, an arm holding the optical fiber tip (hatched parts) turned by 180° around the pipe. The distance of WRS from the snow surface was about $0.3m$.

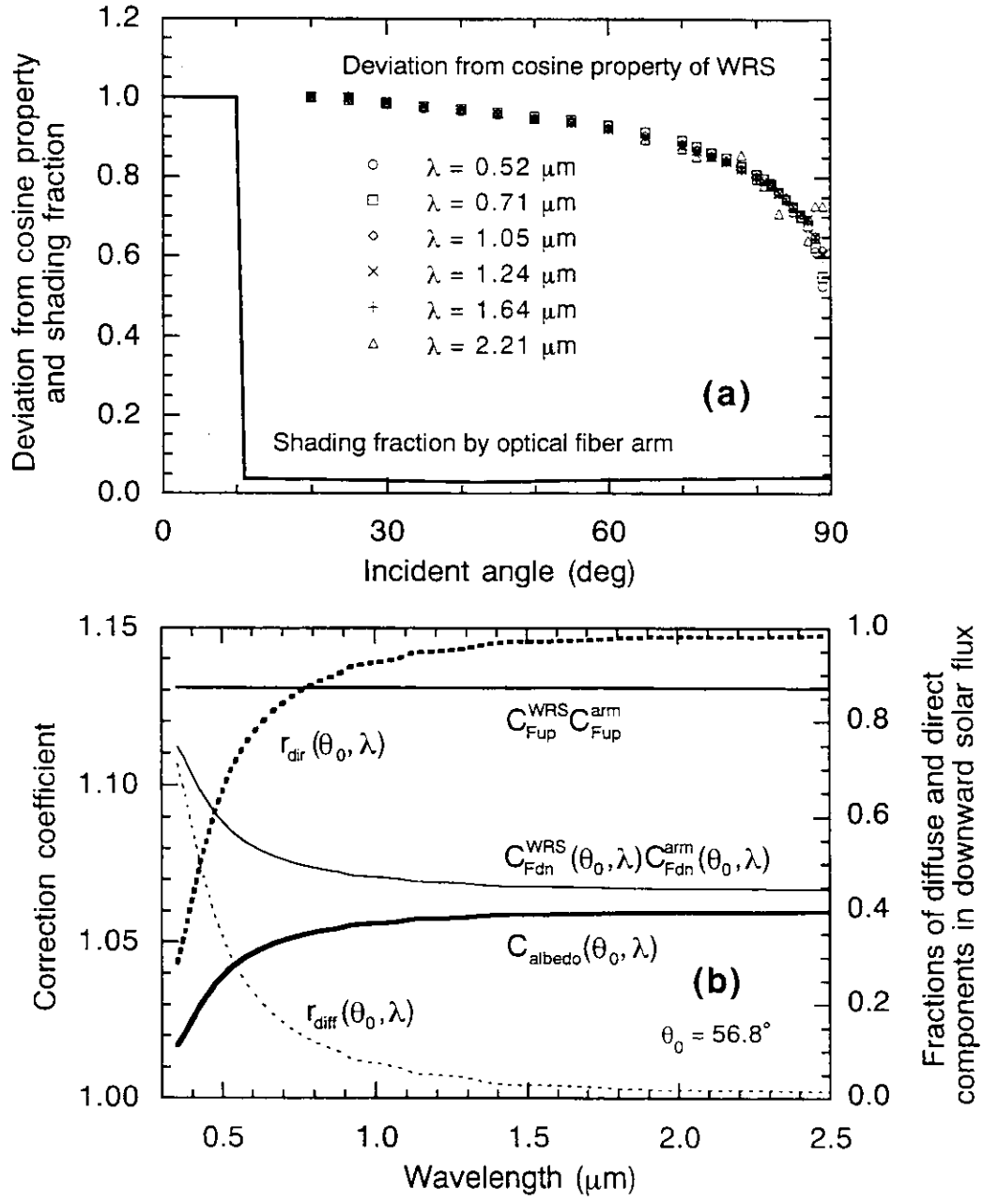

Figure 6. (a) Deviation from the perfect cosine property in the incident angle dependence of the reflectance of WRS (shown by characters) and the azimuthally integrated shading fraction by the optical fiber arm for each angle of incidence viewed from the center of the field of view of the optical fiber on WRS (solid line). The underestimate of radiant flux due to the imperfect cosine property of WRS was 5.36 % for complete diffuse illumination, and 6.19 % for direct solar beam at $\theta_0 = 56.8°$. The total shading fraction by the optical fiber arm was 6.56 % for complete diffuse illumination. (b) Fractions of the diffuse component ($r_{diff}(\theta_0,\lambda)$: thin dashed line) and the direct component ($r_{dir}(\theta_0,\lambda)$: thick dashed line) in downward solar flux theoretically calculated for $\theta_0 = 56.8°$, and correction coefficients for upward solar flux ($C_{Fup}^{WRS}C_{Fup}^{arm}$: middle solid line), downward solar flux ($C_{Fdn}^{WRS}(\theta_0,\lambda)C_{Fdn}^{arm}(\theta_0,\lambda)$: thin solid line), and albedo ($C_{albedo}(\theta_0,\lambda)$: thick solid line) on February 23, 1998.

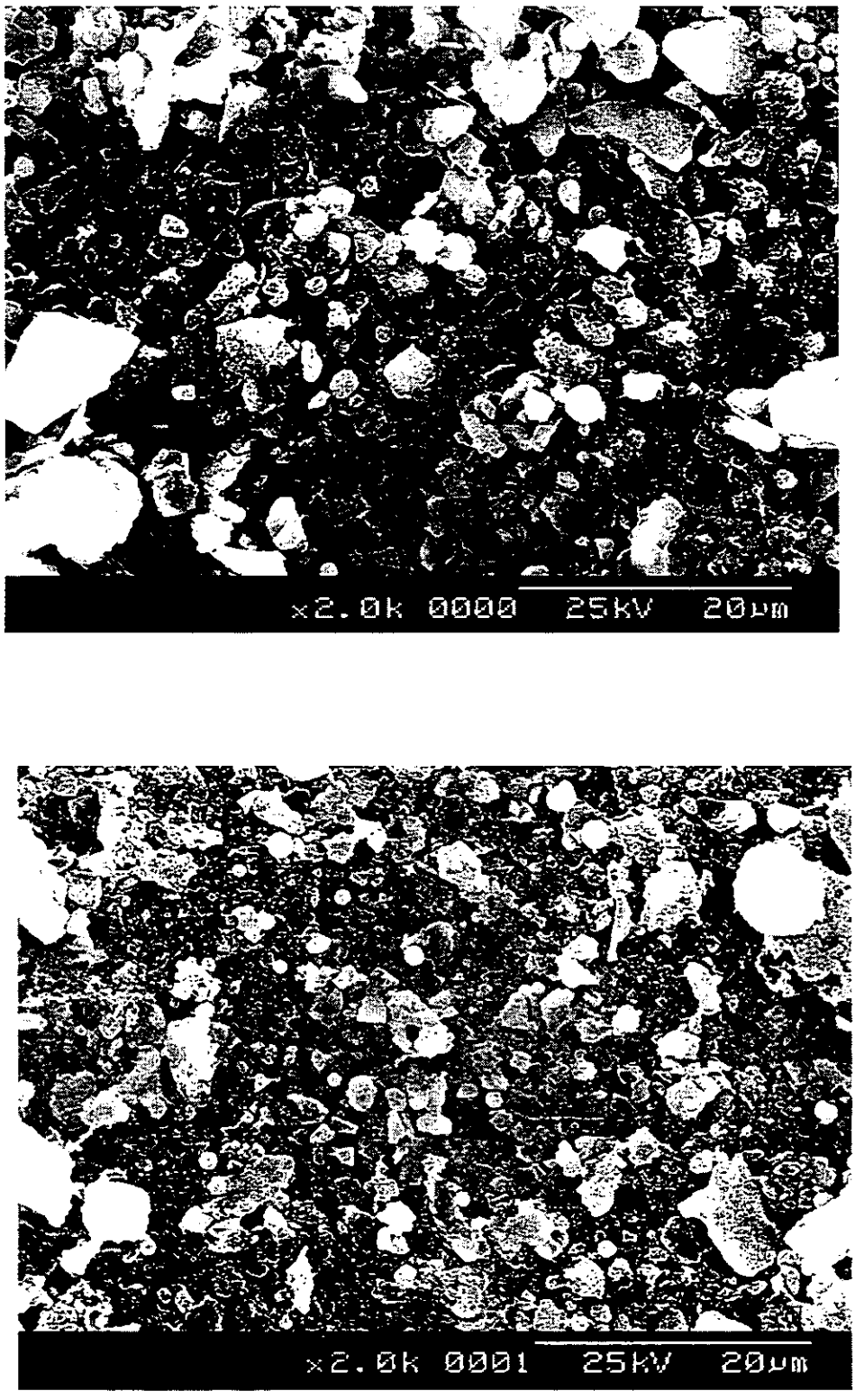

Figure 7. Scanning electron microscope (SEM) photographs of snow impurities collected on Nuclepore filters for the snow samples (top) 980223A1 (0-5 *cm*) and (bottom) 980223A2 (5-10 *cm*) on February 23, 1998.

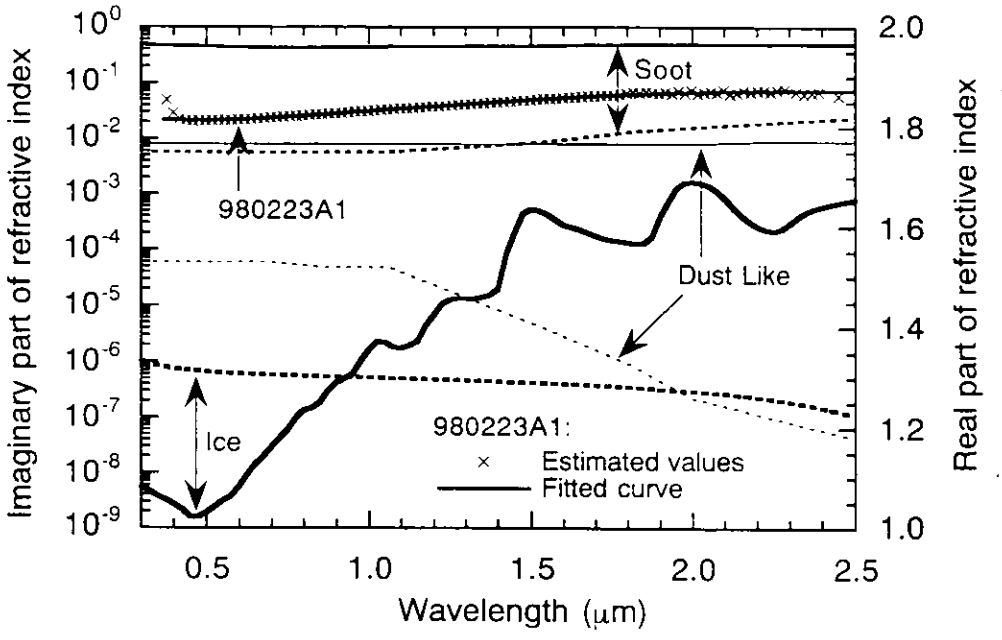

Figure 8. Spectral variations of refractive indices of snow impurities estimated from measurement of the transmittance of a Nuclepore filter on which the impurities in the snow sample 980223A1 had been collected. Imaginary parts ($m_{im}(\lambda)$) are shown by solid lines with the left ordinate, and real parts ($m_{re}(\lambda)$) are shown by dashed lines with the right ordinate. Values for soot [*AFGL*, 1985], Dust-Like aerosol [*AFGL*, 1985], and ice [*Warren*, 1984; *Kou et al.*, 1993] are also plotted for comparison. The fitted curve of $m_{im}(\lambda)$ obtained by means of a cubic equation of wavelength for the snow sample is given by $m_{im}(\lambda) = -0.0141\lambda^3 + 0.0611\lambda^2 - 0.0478\lambda + 0.0317$.

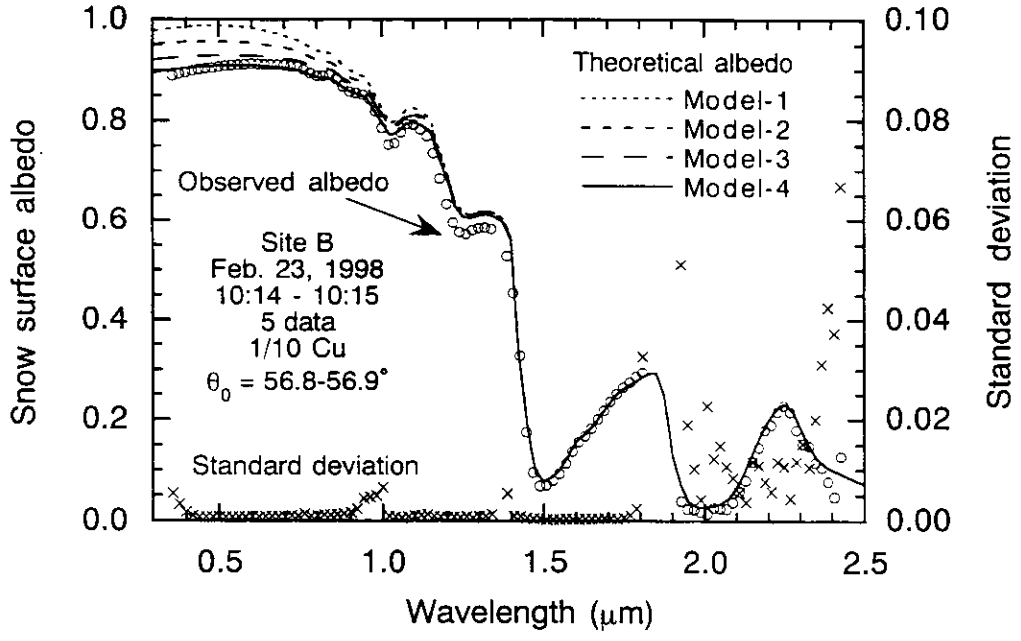

Figure 9. Observed spectral albedo (left ordinate), its standard deviation (right ordinate) on February 23, 1998 and theoretically calculated spectral albedos for four kinds of snow models shown in Figure 10. Observed data are thinned down to one twentieth and only those for which the standard deviation was less than 0.1 are shown. Other observation conditions are shown in Table 1.

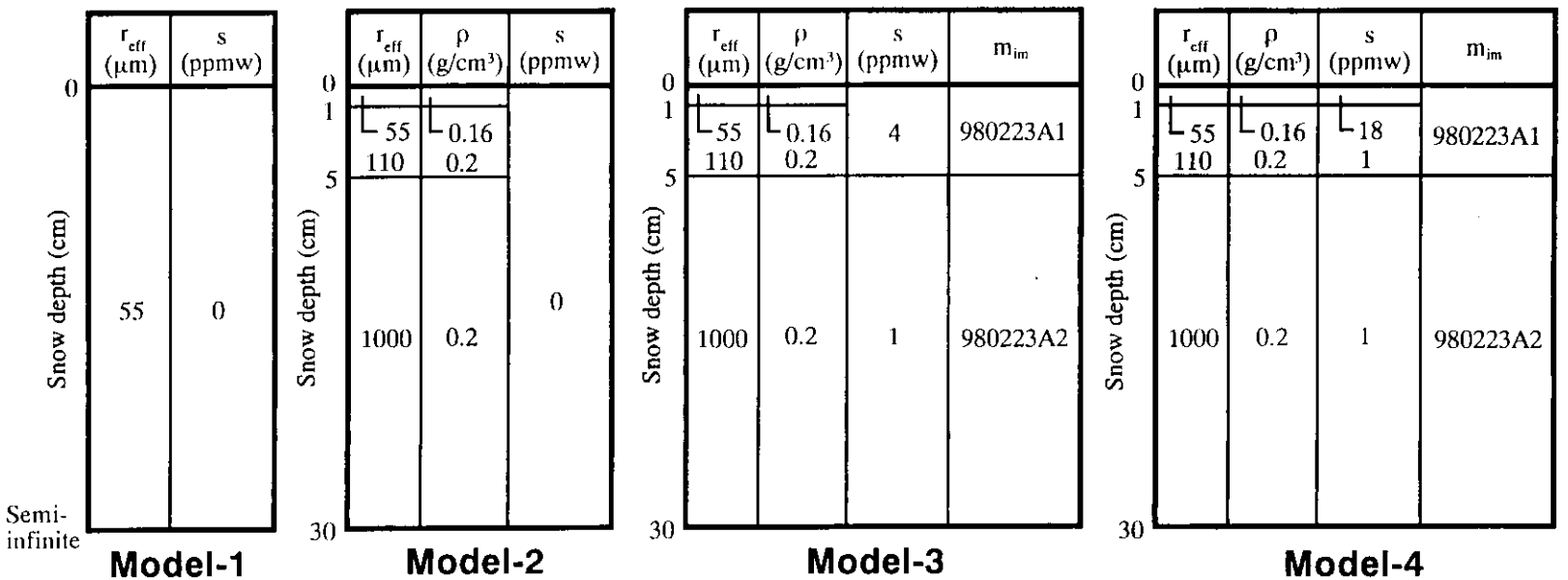

Figure 10. Snow models for which the theoretical spectral albedos were compared with the measurement on February 23, 1998, where r_{eff} is the effective snow grain radius, ρ is the snow density, and s is the concentration of impurities. In the column of m_{im} the name of the snow sample is indicated from which the imaginary refractive index of impurities was derived.

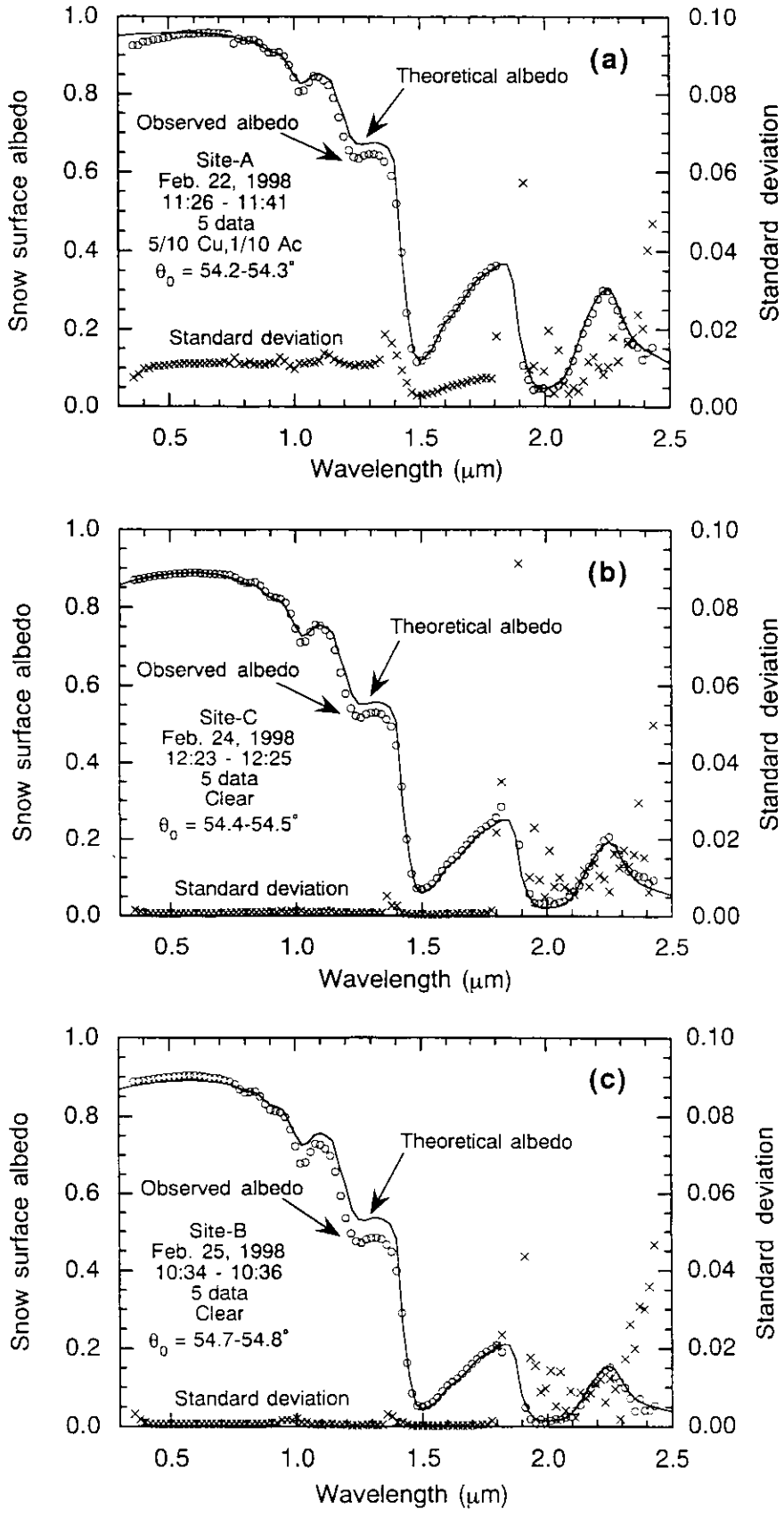

Figure 11. Same as Figure 9 for Model-4, but for (a) February 22, (b) February 24, and (c) February 25 in 1998. Observation conditions are shown in Table 1.

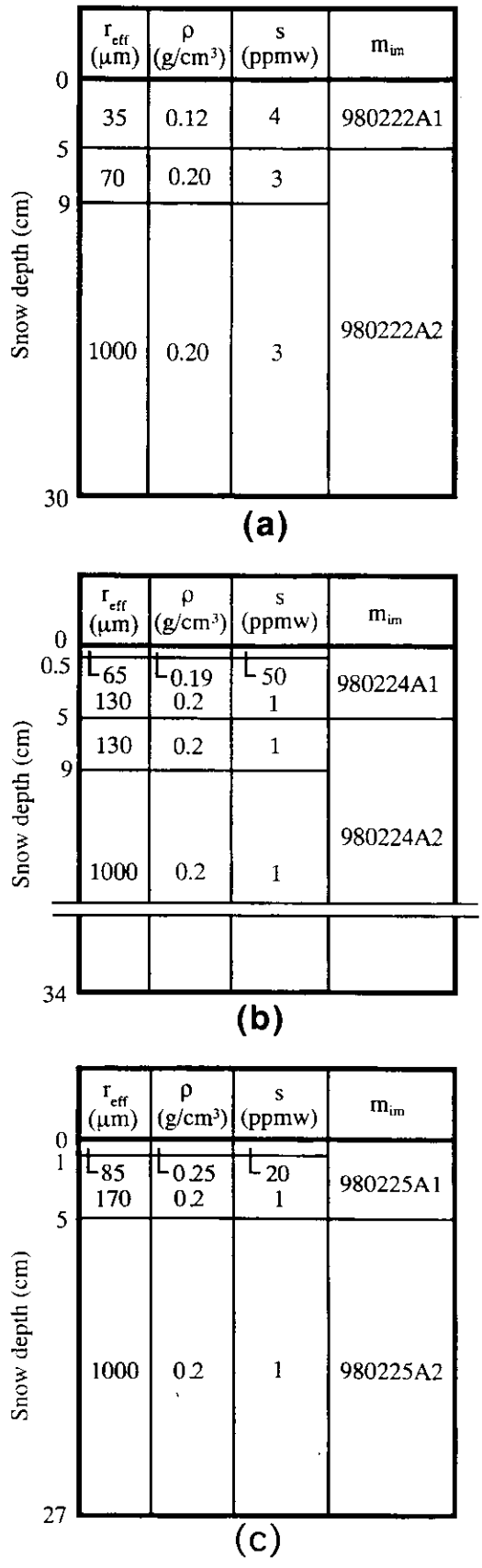

Figure 12. Snow models on (a) February 22, (b) February 24, and (c) February 25 in 1998, for which the theoretical spectral albedos were calculated and compared with the measurements as shown in Figure 11.

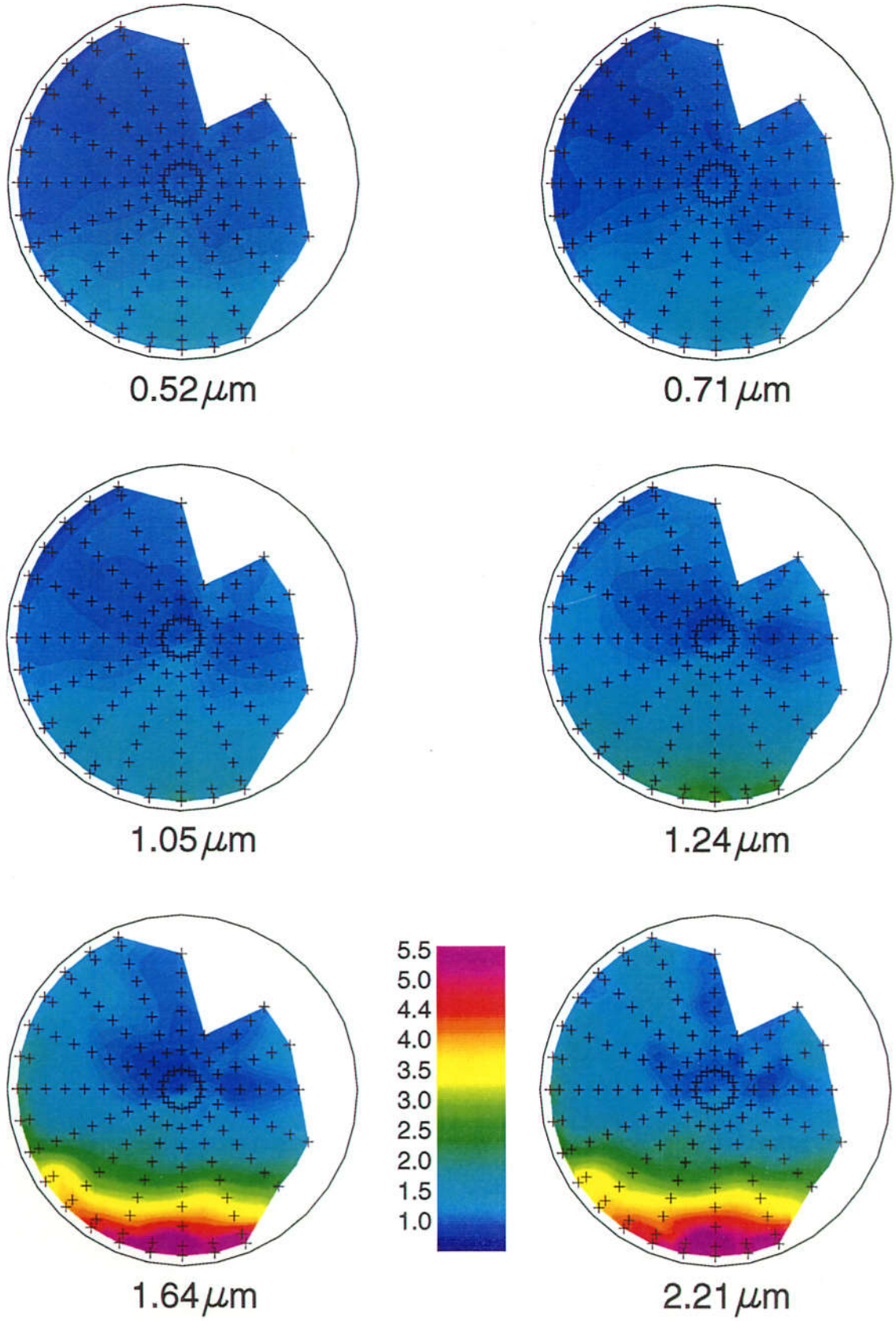

Figure 13. Composite NBRDFs of snow for 6 wavelengths as obtained from measurements of anisotropic reflectance with an optical fiber of 25°-FOV for $\theta_v \leq 70°$ and those obtained with foreoptics of 1°-FOV for $\theta_v \geq 80°$. The measurements using the optical fiber were made in 12:22 - 12:58 LT ($\theta_0 = 54.0 - 56.0°$) and using the foreoptics in 13:20 - 13:34 LT ($\theta_0 = 57.9 - 59.3°$) on February 25, 1998 at Site-B. All reflectances are normalized by the value at the nadir. The plus signs on the each NBRDF map indicate the observed points. The radial coordinate is proportional to the viewing angle θ_v, which is zero at the center of the circle (nadir) and is 90° on the circle. The illumination from the Sun comes from the lower direction of each map, so the bottom of the each map is the forward scattering direction.

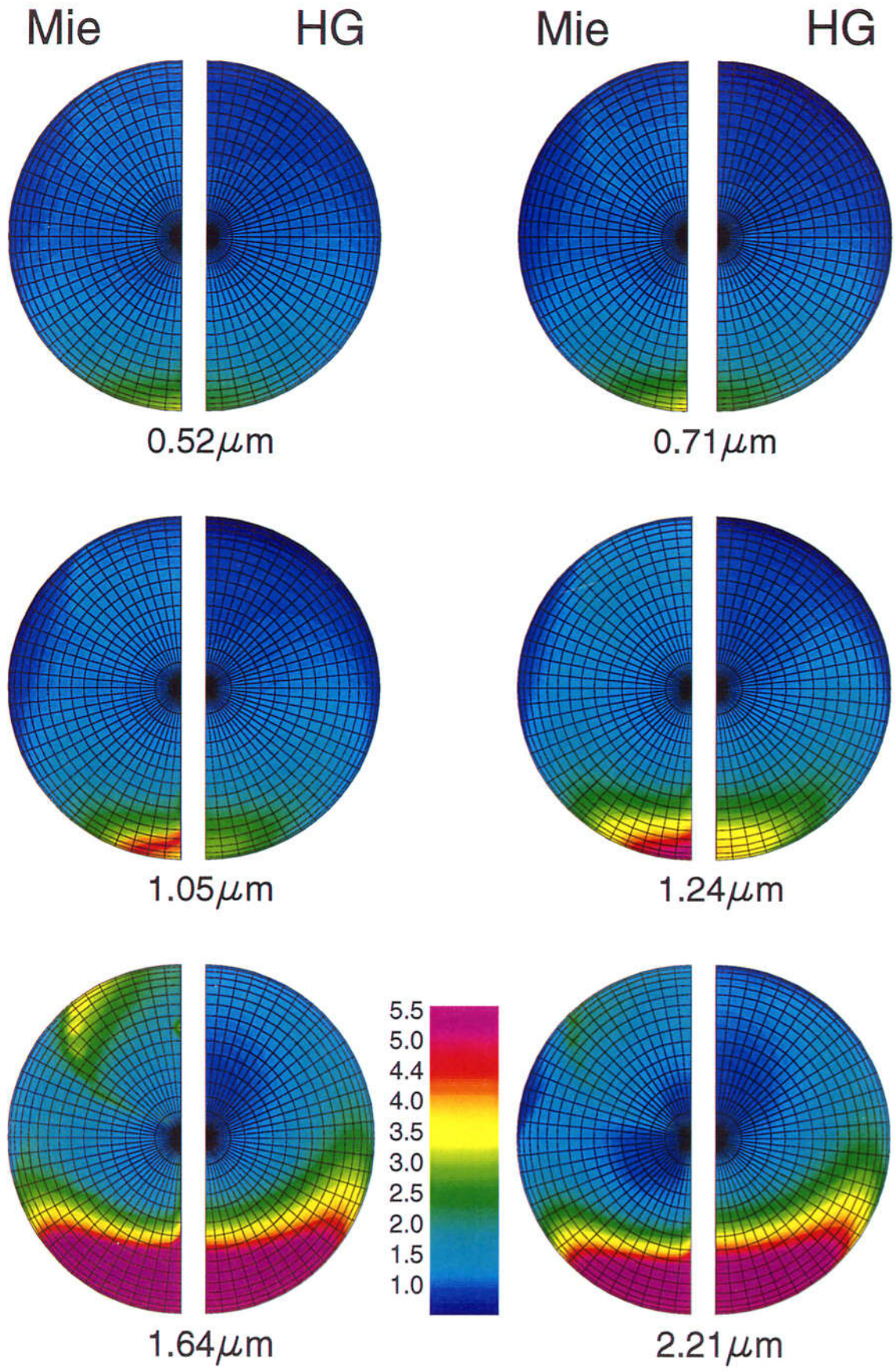

Figure 14. Theoretical NBRDFs of snow for 6 wavelengths. The semicircular maps on the left side were calculated using Mie phase function and those on the right side using HG phase function. The mesh points on each of the NBRDF maps indicate the grid points where calculations were made.

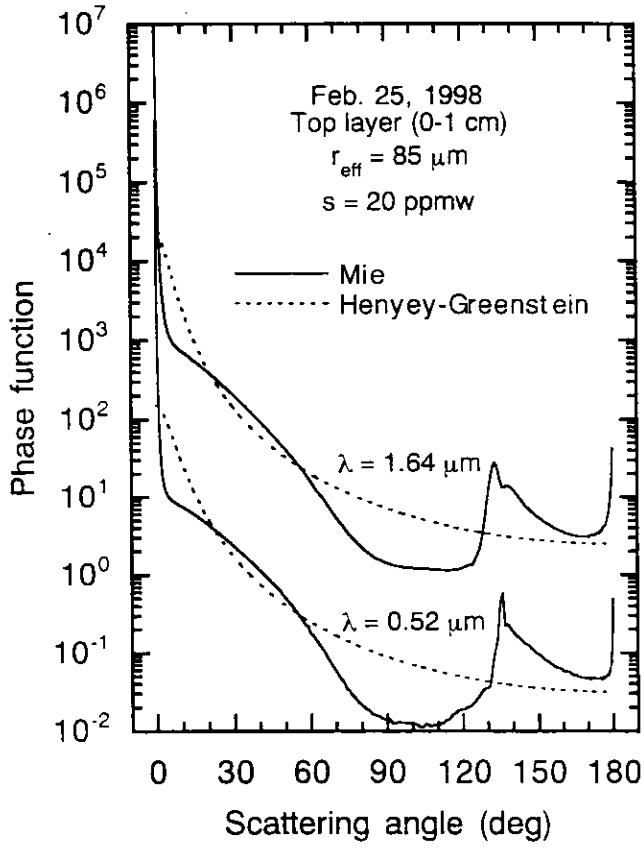

Figure 15. Mie and HG phase functions of snow grains for $\lambda = 0.52$ and $1.64\,\mu m$ in the top layer of the snow model (see Figure 12c) of February 25, 1998. The curves for $\lambda = 1.64\,\mu m$ are displaced upward by a factor of 10^2.

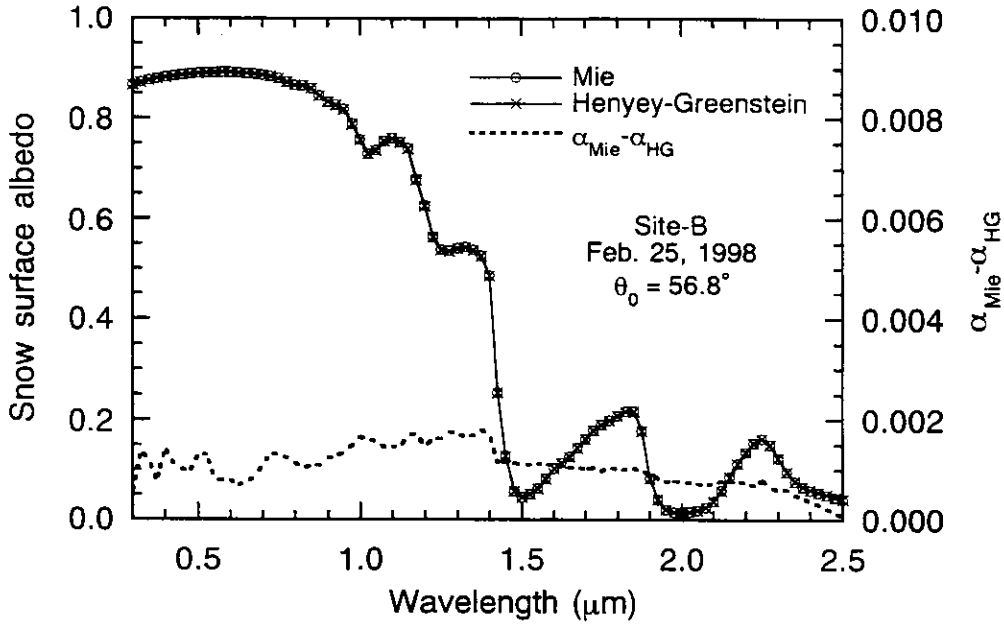

Figure 16. Comparison of theoretical albedos using Mie and HG phase functions (left ordinate) for the snow model of February 25, 1998. The difference between the two albedos is shown on the right ordinate.

General Summary

A multiple scattering radiative transfer model in the shortwave wavelength region has been developed for the atmosphere-snow system in which the absorption and scattering by the realistic gases, aerosols and clouds were included and a radiative interaction between the atmosphere and the snow was simulated. Using this model the atmospheric effects on spectral albedo and radiation budget at the snow surface and the top of the atmosphere were investigated. Furthermore, observations of spectral albedo and bidirectional reflection distribution function (BRDF) with the spectrometer have been made together with the snow pit works on some snowfields. The results of spectral observations were compared with the theoretically calculated ones with a multiple scattering model for the atmosphere-snow system and the effects of snow physical parameters on spectral albedo and BRDF were investigated.

In Chapter 1, the approximation methods for Mie phase function were discussed in calculating the spectral albedo of snow surface by taking account of the multiple scattering by snow particles. The particles such as snow grains which are large compared to the wavelength have a strong forward peak in the phase function of single scattering. It has been known that a large error is led by the calculation of multiple scattering directly using such phase function. Therefore, four types of approximations of Mie phase function were investigated in calculating the multiple scattering by snow particles using the "doubling" method. These involve Hansen's renormalization, Grant's renormalization, the delta-M method and the truncation method. Using these approximations, the spectral albedos of snow surface were calculated under the conditions of effective grain radii of 50, 200 and $1000\mu m$ in a wavelength region from 0.3 to $3.0\mu m$, and were compared to that calculated using the delta-Eddington approximation. The reason to compare with the delta-Eddington approximation is that this method does not need a phase function and a behavior of the systematic error is understood. In the Hansen's renormalization, the maximum albedo error exceeded 0.1 for the snow with an effective radius of $1000\mu m$ at small solar zenith angles. The delta-M method overestimated the snow albedos at all solar zenith angles at the wavelengths less than $1.4\mu m$ for the snow with an effective radius of $1000\mu m$. This was due to the insufficient angle resolution (0.1° in a scattering angle region less than 2°) in the forward peak region of the look-up table of Mie phase function. It was

shown that even with ten times higher resolution in the scattering angle region less than 10° a sufficient accuracy could not be obtained for an effective radius of $1000\mu m$ at the wavelengths less than $0.6\mu m$. Reasonable results were obtained by the Grant's renormalization and the truncation method for all three cases of effective grain radii studied. It was also found that these methods save computation time and memory because the sufficient accuracy was obtained even with an angle resolution of 0.1° in the forward peak region of phase function. In case of truncation method, the result was not sensitive to the choice of a truncation angle between 5° and 20°.

In Chapter 2, the atmospheric effects on spectral and spectrally integrated snow albedos at the snow surface and the top of the atmosphere were investigated. A multiple scattering radiative transfer model based on the "doubling and adding" method combined with the Mie theory was applied to estimate the effects of absorption and scattering by the atmospheric molecules, absorptive gases, aerosols and clouds. Based on the result of Chapter 1, the truncation method with the truncation angle of 10° was employed to correct the anisotropic Mie phase function. It was shown that the spectral surface albedo was reduced by the atmospheric absorptive gases at large solar zenith angles. The solar zenith angle dependence was weakened at the wavelengths less than $0.5\mu m$ by the Rayleigh scattering and at almost all wavelengths by the atmospheric aerosols and cloud cover. H_2O rich atmosphere decreased the spectral surface albedo at large solar zenith angle in the H_2O bands, while the additional reduction of downward solar flux in the near infrared region by H_2O absorption caused the spectrally integrated surface albedo to increase by several percent. Aerosols increased the spectrally integrated surface albedo at small solar zenith angles and reduced it at large solar zenith angles, however they reduced the spectrally integrated planetary albedo except at large solar zenith angles. Optically-thick cloud cover increased both the spectrally integrated surface and planetary albedos at any solar zenith angle. In the visible region at small solar zenith angles the downward solar flux on the snow surface under cloudy sky could exceed that for clear case, and both further could exceed the extraterrestrial solar flux, resulting from the multiple reflection between snow surface and the atmosphere (cloud cover). The global solar radiation on snow surface under cloudy sky, however, never exceeded that for clear case and that at the top of the atmosphere.

It is concluded, from what has been said above, that the snow surface albedo is affected by the appearances of cloud or aerosols of high concentration. It is also found that the snow surface albedo is affected by the Rayleigh scattering at shorter wavelengths and by the atmospheric absorption at large solar zenith angles. Thus, it is necessary to take the atmospheric effects into account for comparison of the theoretical albedo of snow surface with the measured one, according to the conditions of clouds, aerosols, water vapor and solar zenith angle.

In Chapter 3, the spectral albedo in the wavelength region of 0.35-2.5 μm observed on the snowfield under the cloudy sky at Barrow, Alaska in April, 1997 was discussed. The observed spectral albedo was compared with the theoretical ones calculated by a multiple scattering model for the atmosphere-snow system developed in Chapter 2, in which the snow physical parameters obtained from the snow pit work were used. It was found that for new snow consisting of dendrites the optically effective snow grain size was not a crystal size, but of the order of a branch width. The observed spectral albedo was lower than theoretically calculated one for "pure snow" in the visible region and a part of the near infrared region; such reduction was explained by the internal mixture of soot and the external mixture of dust for snow particles. The theoretical spectral albedo calculated for a two-layer snow model that contains impurities agreed well with the measured one at all wavelengths. These results mean that the weakly absorptive dust contributed to the gross concentration (weight mixing ratio) of snow impurities estimated from snow sample and the highly absorptive soot contributed to the albedo reduction in the visible region.

In Chapter 4, the effects of snow physical parameters on spectral albedo and bidirectional reflectance of snow surface were discussed by comparing the observed spectral data with the theoretical ones. The observations of spectral albedo and bidirectional reflectance in the wavelength region of $0.35 - 2.5\,\mu m$ were made together with snow pit work on a flat snowfield under the clear sky in eastern Hokkaido, Japan in February, 1998. The effects of snow impurities, density, layer structure, and grain size attained by in situ and laboratory measurements were taken into account in snow models for which spectral albedos were calculated using a multiple scattering model for the atmosphere-snow system. Comparisons of these theoretical albedos with measured ones suggest that the snow impurities were concentrated at the snow surface by dry fallout of atmospheric aerosols. The optically equivalent snow grain size was found to

be of the order of a branch width of dendrites or of a dimension of narrower portion of broken crystals as was same in Chapter 3. This size was smaller than both the mean grain size and the effective grain size obtained from micrographs by image processing. This means that the optical equivalent snow grain size is smaller than the so-called snow grain size measured glaciologically. The observational results for the BRDF normalized by the radiance at the nadir showed that the anisotropic reflection was very significant in the near infrared region especially at the wavelengths longer than $1.4\mu m$, while the visible normalized BRDF (NBRDF) patterns were relatively flat. Comparison of this result with two kinds of theoretical NBRDFs, where one having been calculated using single scattering parameters by the Mie theory and the other using the same parameters except for Henyey-Greenstein (HG) phase function obtained from the same asymmetry factor as in the Mie theory, showed that the observed NBRDF agreed with the theoretical one using HG phase function rather than with that using Mie phase function, while the albedos calculated with both phase functions agreed well with each other. This suggests that the optically effective snow grain shape is neither the sphere nor the ordinary hexagonal column, by which respectively the rainbow or halo appear in the theoretical BRDF pattern, but is the nonspherical particle having the smooth phase function.

As we have been seen above, the multiple scattering model for the realistic atmosphere-snow system in the shortwave region have been developed by the following things: (1) the examination of appropriate approximation method for Mie phase function; (2) the employment of exact multiple scattering scheme and (3) considering the interaction between the atmosphere and snow. Using this model the quantitative atmospheric effects on the snow albedos were estimated. The optically equivalent snow grain size and the effects of snow layer structure of impurities on spectral albedo were also investigated by comparing the observed spectral albedos with the theoretical ones calculated with this model. It was concluded from these results that the snow albedo is affected by the external factors such as the atmospheric conditions or solar zenith angle although the snow albedo properties are basically determined by the physical parameters of snow itself such as grain size, grain shape, impurities and layer structure. Furthermore, it was suggested from the comparison between the measured snow BRDF and the theoretical one that the observational BRDF pattern was explained with the nonspherical snow particles having the smooth phase function.

From the viewpoint of satellite remote sensing of snow surface, the followings are understood: Since the optically equivalent snow grain size is much smaller than the ordinary grain size measured glaciologically, new snow would be measured as the smallest grain, which is rather the advantage for monitoring the snow grain size from the space with a satellite. The new snow would be observed as small grains with a size of several tens micrometers and the old granular snow would be observed as large grains with a size of several millimeters. Since the snow grain size varies depending on the history of meteorological conditions such as the temperature and solar radiation under which the snow has exposed, the retrieved snow grain size is possible to be used for monitoring the climate change on the ice sheet with a small amount of short term variation of snow grain size. The information content of snow grain size included in the spectral albedo of snow is most abundant in the near infrared region of 1.5-2.3 μm. Compared to the snow with a grain radius of 1000 μm, the spectral albedo of the snow with the grain radius of 50 μm is from several to over ten times higher in this wavelength region and the range of this albedo variation is large enough to make the detection of the snow grain size actual. On the other hand, the snow impurities could enhance the global warming because it reduces the visible albedo. It is necessary to monitor the concentration of snow impurities in the globe. However, compared to the pure snow, the visible albedo is reduced only from several to several tens percent even by the dirty snow with relatively high soot concentration of 1ppmw. It is expected that the more accurate observation is necessary for the snow impurities than the snow grain size. The optical sensor of earth observation satellite ADEOS-II/GLI described in "General Introduction" in this study will equip the visible and near infrared channels which are effective to retrieve the snow grain size and snow impurities. GLI will also carry the 1.6 μm channel which is advantageous to the discrimination of cloud cover over the snow surface. Therefore, it is expected that the global distributions of the snow parameters mentioned above will be clarified.

Some problems to be solved have remained in this study. In the comparison of spectral albedo of snow surface between the observation and theoretical calculation, the observed albedos were always lower than the theoretical ones at the wavelengths of 1.2-1.3 μm. This reason is not clear on the present stage and it is necessary to be investigated further including the optical properties of ice. The snow grain shape would change depending on each stage of the metamorphoses or aging of snow. Thus

it is necessary to model the snow grain shape (or phase function) depending on the snow type of each stage of snow age for the theoretical studies of snow BRDF properties. Together with this, it is effective to measure the phase function of snow particles directly by a polar nepherometer. The studies of BRDF for the non-uniform snow surface such as sastrugi have just begun recently. It needs the approaches both from the observation and the theory. Although the multiple scattering model for the atmosphere-snow system developed in this study is applicable at the solar zenith angles less than 80°, it is desirable to keep the high accuracy even at larger solar zenith angles for the use in the polar regions. Particularly for the studies of ultraviolet radiation in the polar regions, the theoretical calculation would also be necessary under such geometric conditions and thus the improvement of the model is the next coming item. The observation by ADEOS-II/GLI will be started after 2000 and the synchronous validation observation on the snow surface is the most important subject.